universität wien

DIPLOMARBEIT

Titel der Diplomarbeit

Microwave microstructures for enhanced coherent control of nitrogen-vacancy center spin qubits in diamond

Verfasser
Adrian Kowar

angestrebter akademischer Grad
Magister der Naturwissenschaften (Mag.rer.nat)

Wien, 2013

Studienkennzahl lt. Studienblatt:	A411
Studienrichtung lt. Studienblatt:	Physik
Betreuer:	Prof. Jörg Schmiedmayer, Dr. Johannes Majer

Abstract

The principles, possible application and basic implementation of coherent manipulation of single electronic spins of nitrogen vacancy defect centres in diamond using optically detected magnetic resonance has been explored for many years, but the road ahead to achieve a mature application is still a long way off.

A key issue in order to rach that goal is to be able to control the spin states with adequate precision. That control is performed by microwave pulses applied to the defect centre and would essentially benefit from faster state transitions, as decoherence in the form of dephasing represents the greatest impediment in fulfilling that demand. This thesis aims to show that it is possible to enhance the accuracy of spin manipulation by introducing a micro-structure upon the diamond surface, which transports the inbound microwave pulse from a co-planar wave-guide to a location on the diamond where a short-circuit of the structure creates a large magnetic field. As the short-circuit is designed to be circular, the field is expected to closely conform to the field of an ideal current loop, which is supported by finite element simulations.

As a central part of this thesis I manufactured such a device using the micro-technological process of photo-lithography. As applying such tiny structures to small diamond samples poses unexpected difficulties, the reliable procedure that was developed in the process will be highlighted in detail. To demonstrate the success of the process, basic spin manipulation experiments were carried out. These show that the micro-structure performs better than the previous setup, which incorporated a wire for transmission of the microwave signal. The advancements developed in this thesis are faster driven spin transitions, an increased signal-to-noise ratio for optically detected magnetic resonance measurements; a locally stronger magnetic field can successfully be confined to an arbitrarily-sized area with a known field geometry and an immutable position regarding the defect centres.

Kurzfassung

Die Prinzipien und möglichen Anwendungen, sowie die grundsätzliche Implementierung kohärenter Manipulationen einzelner Elektronenspins in Stickstoff-Fehlstellen-Zentren in Diamant mittels optisch detektierter Magnetresonanz wurden in den vergangenen Jahren ausführlich erforscht. Nichts desto trotz ist es noch ein weiter Weg zu einer ausgereiften Anwendung.

Eine essentielle Voraussetzung um dieses Ziel zu erreichen ist die Möglichkeit die Spinzustände mit hinreichender Genauigkeit zu manipulieren. Solche Manipulationen werden mittels Mikrowellen-Pulsen durchgeführt und würden in erster Linie von einer Beschleunigung der Zustandsübergänge profitieren, da Dekohärenz in Form von Spin-Dephasierungen das größte Hindernis das genannte Ziel zu erreichen darstellt. Ziel dieser Diplomarbeit ist es zu zeigen, dass es möglich ist die Genauigkeit der Spin-Manipulation zu erhöhen, indem eine Mikrostruktur zur Leitung der Mirowellensignale auf dem Diamanten errichtet wird. Diese soll die Welle von einem koplanaren Wellenleiter zum Diamanten leiten, wo dieser kurzgeschlossen wird, wodurch an diesem Ort ein starkes magnetisches Feld erzeugt wird. Da der Kurzschluss kreisförmig gestaltet wird, liegt die Annahme nahe, dass sich das Magnetfeld wie das einer geschlossenen stromdurchflossenen Leiterschleife verhält, welche durch Finite-Elemente-Simulationen erhärtet wird.

Im Rahmen der Diplomarbeit wurde mit Methoden der Mikroelektronik, insbesondere Photo-Lithographie, von mir eine derartige Struktur angefertigt. Zusätzliche Schwierigkeiten ergaben sich aufgrund des Umstandes, dass die Struktur auf sehr kleinen Diamantproben platziert werden sollte. Die Lösung dieses Problems machte die Entwicklung eines eigenen Verfahrens notwendig. Um den Erfolg des Herstellungsprozesses zu demonstrieren, wurden einfache Magnetresonanzexperimente durchgeführt. Diese zeigen, dass die Mikrostruktur bessere Ergebnisse liefert als die vorangehende Ausführung, welche aus einem die Mikrowelle transmittierenden Drahtstück bestand. Es kann festgestellt werden, dass die Spin-Übergänge mit der Mikrostruktur schneller getrieben werden können, sich das Signal-Rausch-Verhältnis bei optisch detektierten Magnetresonanz Messungen bessert, das lokal stärkere Magnetfeld auf eine beliebige räumliche Ausdehnung skaliert werden kann und die Feldgeometrie und -position bezüglich der Defekte stets bekannt ist.

Acknowledgements

Although this thesis allowed me primarily to explore a wonderful area of physics and I gained a lot scientific experience during this exploration, the deepest impression is surely that I have had the opportunity to confront my personal weaknesses and identify my own strengths more fully. With this in mind I would like to express my gratitude to my advisors, official – Prof. Jörg Schmiedmayer and Dr. Johannes Majer – and unofficial – Dr. Michael Trupke and Dipl. Ing. Tobias Nöbauer – for guiding me through regions of science which would have remained unidimensional without their assistance, allowing me the freedom to explore territory, which went beyond the expertise of our work group. I particularly appreciate having been granted the time to slowly expand my skills, necessary in order to be able to retain what I learned in bringing myself up to the speed to meet the high standard of the work group. Although not an official advisor, my immediate predecessor working on this material Dipl. Ing. Stefan Putz deserves mention, as he often assisted me on issues as concerned the experimental set-up. Dr. Christian Koller, who guided me along the first steps into the group's subject, provided his helpful expertise throughout the fabrication processes. I also had the pleasure of Matthias Stüwe's erudite company, who taught me everything necessary to know in order to create the micro-structure and thought up many ideas for alternative manufacturing processes with me; he also managed to make the long hours during the machine processes pass swiftly. I would also like to thank Univ. Ass. Dr Georg Steinhauser and Michaela Foster BSc for approving the chemical processes I wanted to undertake. Prof. Max Bichler also provided valuable hints, literally, for dissolving problems. As the number of people providing useful hints and helping hands extends beyond the scope of any acknowledgements, I would like to officially thank everyone in the Schmiedmayer group, as well as the members of the ZMNS[1].

To all the others, first and foremost family and flatmates, but other friends as well, I extend my heartfelt thanks for their invaluable support. They shouldered the everyday weight along with me providing encouragement and moral support when complications arose. Due to their special contributions, I would like, additionally, to mention Nicole Wandl for providing a multitude of explanations on chemical processes and Mario Hofbauer for his IT support.

To sum up of my thesis in terms of myself I need to note that I enjoyed being subjected to so many topics connected science and engineering. I not only learned something about quantum-, atom- and solid state physics, but was also exposed to crystallography and group theory, chemistry (etching, cleaning, patinating), micro-fabrication in the clean room (especially lithography), optics and microwave usage, programming, CAD designing and finite element simulating. I am indeed thankful for having received the opportunity to expand my horizons.

[1] Zentrum für Mikro- und Nanostrukturen, Wien

Contents

1 Introduction

This thesis focuses on the quantum physics of the nitrogen vacancy defect center (NV) in diamond and uses optically detected magnetic resonance (ODMR) as the primary means of observation. The NV is of special interest in many respects: It is a quantum system with two discernible states making it suitable for quantum information processing [DFT+99]. It is a source of fluorescence, shows no photo bleaching[1] and is inherently stationary [FLC+07]. It emits single photons [KMZW00] and is sensitive to magnetic [Deg08] and electric fields [DFD+11].

The NV is a comparatively bright source of fluorescence and may be situated in a nano-diamond as small as 5 nm [IBW+00]. Although it is just an atom-sized defect it provides a maximum fluorescence rate of about 77 MHz [MHS06][2]. This is roughly on the same order of magnitude as quantum dots [RBM+10][3] and much larger than that of fluorescent dye molecules [CN98]. While dye molecules are rendered optically inactive due to photo bleaching within a few seconds to several minutes [SDV+04] and quantum dots withstand illumination for hours only [OLS+05], nano-diamonds containing NV hardly show any photo-bleaching at all. Considering the wide range of possible diamond surface functionalization [SB08], especially with carboxyl addends and the low cytotoxicity [YKC+05], nano-diamonds serve as excellent bio-markers [FLC+07].

Single photons are of essential use for quantum cryptography schemes [EFMP11] like the BB84 protocol [BB84]. Such protocols rely on the arbitrariness of the basis of measurement used into which eigenstates the photons are transformed. By detecting multiple photons representing the same bit of information one could determine the actual state from any basis, due to the probabilistic nature of quantum measurement. Quantum repeaters for long range quantum information transfer [BDCZ98] probably need to rely on single photon sources as well. [EFMP11]. Also true random number generators [ROT94] profit from single photon sources, which intrinsically do not suffer from photon detection coincidences in contrast to e.g. attenuated laser sources. Finally it is necessary to work with single photons in optical quantum computation [KLM+01].

The NV can also be applied as sensor for weak magnetic [Deg08] [MSH+08]

[1] This statement is not of unrestricted validity. The center may occasionally change its charge state and thus cease to fluoresce. Nevertheless it happens so rarely – once during months of observation – that this phenomenon can be dispensed with.

[2] Manson et al. cite several sources which find about 13 ns lifetime for the NVs excited state.

[3] This paper presents fluorescence rates of up to 300 MHz but states that with optically excited quantum dots a rate of 80 MHz could not be exceeded.

[BCK+08][TCC+08] and electric fields [DFD+11]. Such measurements rely on magnetic resonance effects, particularly spin echo measurements, that are dependent on the fields applied and cause an alteration in the progression rate of an NV spin. Magnetometers incorporating NVs can not only detect fields as small as several nT, but offer spatial resolutions of parts of microns. Their application ranges from diamond surfaces as sensor arrays to nano diamonds upon needle tips.

Quantum computation is one of the most promising applications of NV centers. It might be capable of solving several problems impossible to solve with a classical computer. But as the speed of single processing steps is much smaller for current implementations than it is for classical computers their use is not immediately obvious. One of the most prominent advantages of the NV regarding other implementations is, that the NV behaves like an atom or molecule but is trapped forever at its lattice site.

I want to start the next section by presenting the principles of quantum computation. This thesis will not directly deal with performing quantum computation but with the means to perform such operations; therefore, I will summarize the most expedient data about quantum information, ODMR, diamonds and the NV in particular.

The following sections explain the experimental setup used to measure the fluorescence of single NVs and ensembles of NVs and manipulate the spin state of NVs using microwave pulses.

The scope of this thesis was to design, manufacture and test a gold micro-structure on top of the diamond sample. The structure is intended to enhance the capability to transport microwaves to the NVs, which are located a few micrometres beneath the respective diamond's surface. Therefore the field driving magnetic resonance of NV spins will become stronger, which will increase the speed of NV spin transitions. ODMR experiments on NVs are carried out with this new device and comparisons to the previous configuration are drawn.

2 Quantum information processing

2.1 The qubit

2.1.1 Qubits and quantum registers

Qubit is a short name for quantum bit. Like its classical counterpart, the bit, which is the smallest amount of classical information, the qubit is the smallest amount of quantum information. A classical bit is capable of assuming one of two possible states. A qubit can be measured to be in one of two possible states, but in contrast to a classical bit it can assume any linear combination of these states and is thus called a superposition. Two-state systems or two-level systems are commonly used terms for such quantum systems. Although there are often two states that are distinguished by being inherently suitable for measurement of physical properties (like the spin orientation of an electron) every pair of basis states $|\psi_0\rangle, |\psi_1\rangle$ can be used to compose the superposition state $|\Psi\rangle$ [CTDL92]:

$$|\Psi\rangle = c_0 |\psi_0\rangle + c_1 |\psi_1\rangle , \tag{2.1}$$

with c_0, c_1 being complex coefficients that carry the information contained in the qubit. For coding larger amounts of information, systems containing multiple qubits need to be used. Such an array of N qubits is called a quantum register of size N. In order to understand the dynamics and measurement of qubits and quantum registers, concepts like quantum measurement, unitary time evolution and entanglement are required. These may be found in numerous textbooks [CTDL92][Fox06][AP01] but I also added a small section (8.2) to the appendix summarizing the basics of quantum mechanics for swift recapitulation. With knowledge about the behaviour of collections of quantum systems it is possible to expand the equation for a single qubit state (2.1) to describe a two-qubit quantum register:

$$|\Psi\rangle = \sum_{ij} c_{ij} |ij\rangle , \tag{2.2}$$

with $i, j = 0, 1$. As four variations of 0 and 1 to i and j can be assigned, there are four summands, which means four complex coefficients are needed to fully define the state. For an N qubit state the number of complex valued degrees of freedom rises to 2^N:

$$|\Psi\rangle = \sum_{i_1 \ldots i_N} c_{i_1 \ldots i_N} |i_1 \ldots i_N\rangle , \tag{2.3}$$

with the indices forming all variations of zero and one. This means that the amount of information which can be stored in the quantum register grows exponentially with the

size of the register. As every quantum state needs to be normalized (see section8.2.2, figure 8.15), the following requirement has to be met for the coefficients:

$$\sum_{i_1 \ldots i_N} |c_{i_1 \ldots i_N}|^2 = 1. \tag{2.4}$$

2.1.2 Quantum computing

The enormous information capacity of larger quantum registers has already giben rise to the assumption of great computation power and consequently has stimulated the creation of algorithms that can solve a variety problems, which would normally be intractable for classical algorithms [Sho94][AL97]. Unfortunately, quantum measurements are of a probabilistic nature (see 8.2.2), which means that only eigenvalues of the observable are actually measured and the probability of their occurrence depends on the projection of the superposition state onto the eigenstates of the observable. This reduces the amount of information extracted from such a system to a single state with 2^N configurations, which is equal to the information retrieved from a classical bit array. In contrast, algorithms that manipulate the information stored in quantum registers are not affected by this impediment, as long as they do not incorporate a measurement of the quantum system. The unitary operations (see 8.2.3) describing the time evolution of the unobserved quantum system do not cause any loss of information. Therefore, algorithms composed of a series of unitary operations can fully exploit quantum parallelism. The key to retrieve the result of a quantum algorithm and therewith to make the computation power of such systems accessible, is to distill a single relevant piece of information from a calculation and transform the representing state into an eigenstate of the system, which makes it measurable, ideally, with a probability of 100 %.

Currently known quantum algorithms are mostly based on quantum Fourier-transformations, such as Shor's algorithm (it achieves prime factorization of a number n in $\mathcal{O}((log(n))^3)$ processing steps [Sho94]), or on amplitude amplification, such as Grover's algorithm (it trawls an n-sized database in $\mathcal{O}(\sqrt{n})$ processing steps [Gro97]). Some algorithms, e.g., for the simulation of quantum systems [AL97], solve problems of the BQP (bounded error quantum polynomial time) class by other means.

All quantum algorithms have in common the fact that they consist of three stages:

- Initialization: This corresponds to a projection operation. The created state is intrinsic to the physics of the creation process. To give some examples: In experiments using photons a BBO crystal can be used to create entangled pairs of horizontally and vertically polarized photons by parametric down conversion. In experiments relying on magnetic resonance effects, spin polarization can be achieved by applying a strong external magnetic field.

- Preparation: This stage is performed by applying unitary operations on the ini-

tialized state[1]. This stage comprises two tasks: First, the state representing the problem to be solved is prepared. Subsequently the algorithm is applied to prepare an eigenstate that is going to be measured.

- Measurement: The detection of an eigenvalue, represented by an observable, is carried out. The superposition is destroyed; therefore, predictions about any state not being an eigenstate cannot be made with regard to a single experiment run. The state has to be prepared repeatedly to gain a statistical determination of the state.

The implementations of such unitary transformations on qubits are called qubit gates and are discussed in section 2.1.4

2.1.3 Qubit representation on the Bloch sphere

A very common visualization of a qubit uses a vector on the so-called Bloch sphere. The vector oriented along the z-axis of the Bloch sphere is associated with $|0\rangle$, the vector in the opposed direction with $|1\rangle$. The polar angle θ corresponds to the ratio of the basis components, the azimuthal angle ϕ denotes the relative phase information (ϕ) between the components [NC11]:

$$\Psi = e^{i\gamma}\left(cos\frac{\theta}{2}|0\rangle + e^{i\phi}sin\frac{\theta}{2}|1\rangle\right). \tag{2.5}$$

The term containing the global phase γ can be dispensed with, as it does not affect physics. As the coefficients c_0, c_1, and respectively θ, ϕ are arbitrary, the fact that the amount of information possible to be encoded within one qubit exceeds that of a classical bit can be made visible.

Any unitary transformations of single qubits which are actively driven processes as well as unperturbed time evolution can be represented by a rotation on the Bloch sphere[2]. Compared to transformations of a classical bit, which are just bit flips, the qubit features two free parameters.

Single qubit states are pure quantum states and thus have always norm one; therefore, their vectors form the surface of the Bloch sphere. When looking at an ensemble of qubits prepared identically, their representation on the Bloch sphere should be equal to that of a single qubit. Due to interaction with the environment the qubits of an ensemble each have slightly different Hamiltonians and thus experience slightly different unitary transformations. This means the qubit vectors will start to diverge and their deviation will increase with time. The mean of the vectors representing the qubits in the ensemble will no longer be a vector on the surface of the Bloch sphere but rather a vector inside the sphere. This result is referred to called a mixed state. A completely mixed state will

[1] This is a simplification as there are algorithms that use projection operators in the state preparation process.

[2] Rotations are unitary transformations themselves.

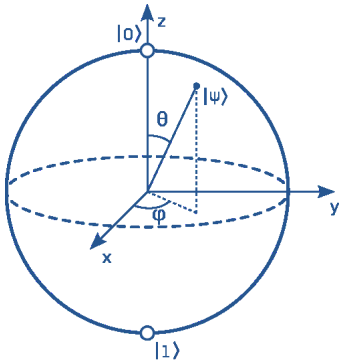

Figure 2.1: The Bloch sphere is used to depict the state a quantum mechanical two state system. The vector can occupy any state between the eigenstates named 0 and 1 in this picture. The polar angle represents the portion of one eigenstate regarding the other and the azimuthal angle represents the phase.

be represented by the point in the middle of the sphere. The transition of a pure state into a mixed state can be described by decay constants and will be treated in section 2.2.6.

2.1.4 Qubit gates

2.1.4.1 Column vector representation of qubit states

A useful way to represent quantum states of discrete levels is to write the coefficients in column vectors. Each position in the vector refers to a basis state of the system. The order of these basis states is defined by convention. Taking the example of a qubit state a possible convention would be

$$|\psi\rangle = c_0 |0\rangle + c_1 |1\rangle = c_0 \begin{pmatrix} 1 \\ 0 \end{pmatrix} + c_1 \begin{pmatrix} 0 \\ 1 \end{pmatrix} = \begin{pmatrix} c_0 \\ c_1 \end{pmatrix}. \tag{2.6}$$

For a two-qubit state the tensor product has to be considered. If the convention for the tensor product between elements of the subspaces $\mathfrak{H}_A$ and $\mathfrak{H}_B$ is set to be

$$\begin{pmatrix} a \\ b \end{pmatrix} \otimes \begin{pmatrix} c \\ d \end{pmatrix} = \begin{pmatrix} ac \\ ad \\ bc \\ bd \end{pmatrix}, \tag{2.7}$$

then the basis vectors stack up in the following way:

$$\begin{pmatrix} |0\rangle_A \otimes |0\rangle_B \\ |0\rangle_A \otimes |1\rangle_B \\ |1\rangle_A \otimes |0\rangle_B \\ |1\rangle_A \otimes |1\rangle_B \end{pmatrix}. \tag{2.8}$$

In consequence, a two-qubit state could be written as

$$|\psi\rangle = c_{00}\,|00\rangle + c_{01}\,|01\rangle + c_{10}\,|10\rangle + c_{11}\,|11\rangle = \begin{pmatrix} c_{00} \\ c_{01} \\ c_{10} \\ c_{11} \end{pmatrix}. \tag{2.9}$$

The state of a quantum register of size N can thus be represented as a complex scalar valued vector of dimension n. Operators acting on such states can be represented by squared matrices of dimension $n \times n$.

2.1.4.2 Single-qubit gates

Quantum gates are the elementary operations that can be performed on a qubit to manipulate information. Mathematically, a gate is represented by a unitary transformation U acting on a quantum state Ψ:

$$\Psi' = U\Psi, \tag{2.10}$$

with the normalization condition $\int |\Psi| d^3x = \int |U\Psi| d^3x = 1$. As a qubit has two properties that can superpose, the transformation will be represented by a 2×2 matrix for a single qubit transformation. Most relevant single qubit gates are rotations around the principal axes [NC11]. Rotations by an angle π can be represented by the Pauli matrices:

$$\sigma_x = \begin{pmatrix} 0 & 1 \\ 1 & 0 \end{pmatrix} \quad , \quad \sigma_y = \begin{pmatrix} 0 & -i \\ i & 0 \end{pmatrix} \quad , \quad \sigma_z = \begin{pmatrix} 1 & 0 \\ 0 & -1 \end{pmatrix}. \tag{2.11}$$

A rotation about $\pi/2$ is necessary to transform a spin from an eigenstate into a superposition of equal portions of both possible eigenstates. This gate is called Hadamard gate, implemented by a $\pi/2$ pulse and represented by

$$U_H = \frac{1}{\sqrt{2}} \begin{pmatrix} 1 & 1 \\ 1 & -1 \end{pmatrix}. \tag{2.12}$$

I will provide an explanation of the physical process behind these gates in section 2.2.

2.1.4.3 Multi-qubit gates

Apart from one qubit gates, two qubit gates and multi qubit gates are possible as well. As one can combine wave-functions using the tensor product the dimension of the combined representation doubles with each qubit involved. By the same token the representation of the transformation increases in size. Although not realized within this thesis the CNOT ([3]) is also noteworthy, as it completes the set of qubit operations for a universal information processing machine [BBC+95]. This gate performs an inversion of the current state depending on the state of another spin in the surroundings:

[3] An equivalent gate called CROT was implemented in 2004 for the NV center[JGP+04b]

$$CNOT = \begin{pmatrix} 1 & 0 & 0 & 0 \\ 0 & 1 & 0 & 0 \\ 0 & 0 & 0 & 1 \\ 0 & 0 & 1 & 0 \end{pmatrix}. \tag{2.13}$$

2.2 Rabi oscillations

2.2.1 Larmor precession

To describe the dynamics of a spin, we can treat it as if it were a rotating, charged object. A magnetic field $\vec{B}$ may apply a torque to that spin: $\vec{\tau} = \vec{r} \times \vec{F} = \vec{r} \times (\vec{j} \times \vec{B})$, with $\vec{F}$ being a Lorentz force caused by the current density $\vec{j}$. Using the classical definition of the magnetic momentum $\vec{\mu} = \frac{1}{2} \int \vec{r} \times \vec{j}(\vec{r})\, d^3r$, the commonly known relation $\vec{\tau} = \vec{\mu} \times \vec{B}$ can be derived (cf. appendix 8.4). Commonly the magnetic moment for electrons is defined as $\vec{\mu} = \gamma \hbar \vec{S}$, with $\vec{S}$ being the spin operator, $\hbar$ the Planck constant and γ the gyromagnetic ratio for an electron. Therefore the temporal change of the magnetic momentum of an electron, which equals to its torque, constitutes the equation of motion for that spin:

$$\frac{d\vec{\mu}}{dt} = \vec{\mu} \times \gamma \vec{B}. \tag{2.14}$$

In order to solve this equation, a coordinate transformation from the laboratory system S to a rotating frame $\tilde{S}$ is practicable. The angular velocity $\vec{\omega}$ of the rotating frame with respect to the laboratory system links the time-derivatives of an arbitrary vector $\vec{X}(t)$ in the following way [Abr61]:

$$\left(\frac{d\vec{X}}{dt}\right)_S = \left(\frac{d\vec{X}}{dt}\right)_{\tilde{S}} + \vec{\omega} \times \vec{X}. \tag{2.15}$$

Thus the equation of motion in the rotating frame can be formulated as [Sli90]:

$$\frac{d\vec{\mu}}{dt} = \vec{\mu} \times \gamma \left(\vec{B} + \frac{\omega}{\gamma}\right) = \vec{\mu} \times \gamma \vec{B}_r, \tag{2.16}$$

where the effective field $\vec{B}_r$, which includes the virtual field generated by the rotation, substitutes the magnetic field of the laboratory system $\vec{B}$. By selection of a frequency $\omega_0 = -\gamma B_0$ for a static magnetic field $\vec{B}_0$, the field sensed by the electron spin within the rotating frame becomes zero; thus, the spin vector appears to be a fixed vector in the rotating frame. In other words, the corresponding Larmor frequency ω_0 of the precession of the spin matches the rotation of the frame.

In the following the effect of an alternating magnetic field shall discussed. Therefore an additional field $\vec{B}_1(t) = \vec{B}_1 \cos(\omega_1 t)$ is assumed to be perpendicular to the static magnetic field $\vec{B}_0$. The rotating field $\vec{B}_1(t)$ is be aligned with the x-axis of the rotating frame $\tilde{S}$, so that it rotates with the angular velocity ω_1. Therefore, the effective field in the rotating frame is again static, with the equation of motion expressed as [Sli90]:

$$\frac{d\vec{\mu}}{dt} = \vec{\mu} \times \gamma \left(\left(B_0 - \frac{\omega_1}{\gamma} \right) \vec{k} + H_1 \vec{i} \right) = \mu \times \vec{B}_{eff}, \tag{2.17}$$

with $\vec{k}$ being the basis vector aligned with the static magnetic field and $\vec{i}$ the basis vector perpendicular to it. This results in an effective field [Sli90]:

$$\vec{B}_{eff} = \left(B_0 - \frac{\omega_1}{\gamma} \right) \vec{k} + B_1 \vec{i}. \tag{2.18}$$

Therefore, if the angular velocity ω_1 (the frequency of B_1) equals the Larmor frequency ω_0 the component along the axis of the rotational frame becomes zero: $(B_0 - \omega_1/\gamma)\vec{k} = 0$. The magnetic moment registers exclusively the component $B_1\vec{i}$, meaning the spin will precess around an axis perpendicular to the axis of the rotating frame. This, a spin transition can be induced. From the laboratory frame a spin transition from a direction along the z-axis to its opposite direction with a precession induced by B_1 much smaller than the Larmor frequency presents itself as the the magnetic moment spiralling downwards (and eventually upwards again).

2.2.2 Semi-classical treatment of dipole transitions

In quantum mechanics dynamics of a state $|\Psi(\vec{r}, t)\rangle$ obey the Schrödinger equation $\hat{\mathcal{H}}\Psi = i\hbar\frac{\partial\Psi}{\partial t}$. The Hamiltonian determines the dynamics and includes all factors affecting the evolution of the state considered in the physical model. In case of the spin state of an NV these factors are the unperturbed time evolution of the wave-function and the interaction with the microwave field. The microwave has a frequency $\omega \approx \omega_0 = (E_1 - E_0)/\hbar$ corresponding to the NV spin resonance frequency [Fox06]. The overall Hamiltonian is simply the sum of the Hamiltonians of the respective effects:

$$\hat{\mathcal{H}} = \hat{\mathcal{H}}_{\text{unp.}}(\vec{r}) + \hat{\mathcal{H}}_{\text{int.}}(t). \tag{2.19}$$

The Schrödinger equation is a linear partial differential equation regarding $|\Psi\rangle$, as long as the Hamiltonian does not include a dependency on the wave-function itself, which may be the case if there were e.g. self-interactions. Thus the equation can be split into a time-independent and a time-dependent part:

$$\hat{\mathcal{H}}_{\text{unp.}}\Psi + \hat{\mathcal{H}}_{\text{int.}}(t)\Psi = i\hbar\frac{\partial\Psi}{\partial t}. \tag{2.20}$$

Starting by solving the equation without the term representing the microwave interaction, one finds the unperturbed solution $\Psi_{0,i}$. The Hamiltonian $\hat{\mathcal{H}}_{\text{unp.}}$ describes the molecular orbits and provides two eigenvalues, the energies E_0 and E_1, which are the energies of the respective levels. Therefore, there are two stationary solutions fulfilling the stationary Schrödinger equation $\hat{\mathcal{H}}_0\psi_i(\vec{r}) = E_i\psi_i(\vec{r})$. Using those, the unperturbed solution reads:

$$\Psi_{unp.,i}(\vec{r}, t) = \psi_i(\vec{r})e^{-iE_it/\hbar}. \tag{2.21}$$

The perturbed solutions of the time-dependent equation can be found using variation of the constants. Adding the unterturbed solutions for the two energy eigenvalues yields:

$$\Psi(r,t) = c_0(t)\psi_0(r)e^{iE_0t/\hbar} + c_1(t)\psi_1(r)e^{-iE_1t/\hbar}. \tag{2.22}$$

Following the description in [Fox06], I provide a treatment of the perturbed case, in which the dipole moment of the two-level system couples to a resonant classical electric field. The energy of an electric dipole in an electric field is expressed as:

$$E_{int.}(t) = q_e\vec{r}\vec{\mathcal{E}} = q_e z\mathcal{E}_0\cos(\omega t) = \frac{q_e z\mathcal{E}_0}{2}\left(e^{i\omega t} + e^{-i\omega t}\right). \tag{2.23}$$

Thereby, the interaction Hamiltonian $\hat{\mathcal{H}}_{\text{int.}}$ is presented as interaction of the dipole with the electric field, which is set to be an alternating field in z-direction only: $\vec{\mathcal{E}} = \vec{e}_z\mathcal{E}_0\cos(\omega t)$. The dipole is defined by the shift of an electric charge q_e by a distance $\vec{r} = z\vec{e}_z$. The components of the perturbed Hamiltonian thus are

$$\hat{\mathcal{H}}_{\text{int.,ij}}(t) = \langle i \,|\, E_{int.}(t) \,|\, j\rangle = \frac{\mathcal{E}_0}{2}\left(e^{i\omega t} + e^{-i\omega t}\right) q_e \langle i \,|\, z \,|\, j\rangle = -\frac{\mathcal{E}_0}{2}\left(e^{i\omega t} + e^{-i\omega t}\right)\mu_{ij}, \tag{2.24}$$

with $\mu_{ij} = -q_e \langle i \,|\, z \,|\, j\rangle = -q_e \int \psi_i^* z \psi_j \; d^3r$ being the dipole matrix elements. Because the position z is an odd parity quantity and atomic states need to be either odd or even, the dipole needs to be of odd parity too [Fox06]; thus, the matrix is completely anti-symmetric, which implies that all the diagonal elements are zero. Further, the dipole matrix element is a measurable quantity and therefore a real number. Combined with the restriction that $\mu_{12} = \mu_{21}^*$ this results in $\mu_{12} = \mu_{21}$. Thus, the two equations derived in [Fox06] give the following time evolutions for c_0 and c_1:

$$\dot{c}_0(t) = i\frac{\mathcal{E}_0\mu_{12}}{2\hbar}\left(e^{i(\omega-\omega_0)t} + e^{-i(\omega+\omega_0)t}\right)c_1(t) \tag{2.25}$$

$$\dot{c}_0(t) = i\frac{\mathcal{E}_0\mu_{12}}{2\hbar}\left(e^{-i(\omega-\omega_0)t} + e^{i(\omega+\omega_0)t}\right)c_0(t). \tag{2.26}$$

The Rabi frequency is introduced:

$$\Omega_R = \frac{|\mu_{el.12}\mathcal{E}_0|}{\hbar}. \tag{2.27}$$

And analogous to that, the transition between two magnetic dipoles (spins) is

$$\Omega_R = \frac{|\mu_{12}B_0|}{\hbar}, \tag{2.28}$$

with B_0 being the magnetic field strength and μ_{12} the magnetic dipole moment matrix element. That can be rewritten using the spin projection quantum number m_s, the gyromagnetic ratio g and the electron Bohr magneton μ_B:

$$\Omega_R = \frac{|\mu_B\, g\, \Delta m_s\, B_0|}{\hbar}. \tag{2.29}$$

Thus we obtain the equations needed to be solved to understand the dynamics of a spin subjected to an alternating electromagnetic field. Two distinct solutions can be found, one for a strong and one for a weak coupling to the field. The strong field solution is more important, as it is our aim to effectively change the spin by coupling it to a strong field.

2.2.3 Rabi-oscillations in the strong field limit

In the strong field limit some assumptions may be made: First of all the rotating wave approximation is applied. It states that any off-resonant frequencies will have a negligible effect. If the frequencies ω and ω_0 are quasi identical, the term containing the sum of the frequencies will contribute high frequency oscillations that will cancel each other out in a time average for typical microwave transition time domains. Considering pure resonance, the above equations simplify to

$$\dot{c}_0(t) = \frac{i\Omega_R}{2} c_1(t) \tag{2.30}$$

$$\dot{c}_1(t) = \frac{i\Omega_R}{2} c_0(t). \tag{2.31}$$

These equations can be condensed into one by differentiating one of them and inserting it into the other. This results in a differential equation of a second order, well known from harmonic oscillations.

$$\ddot{c}_0(t) + \frac{\Omega_R}{2} c_0(t) = 0 \tag{2.32}$$

Recognizing the coefficient $\frac{\Omega_R}{2}$ as a frequency of the oscillation, one may express their equations as

$$c_0(t) = \cos(\frac{\Omega_R t}{2}) \tag{2.33}$$

$$c_1(t) = i\, \sin(\frac{\Omega_R t}{2}). \tag{2.34}$$

The probability for finding the system in state $|0\rangle$ resp. $|1\rangle$ is expressed as

$$\mathcal{P}_{|0\rangle}(t) = \langle 0\rangle\, \Psi = |c_0(t)|^2 = \cos^2(\frac{\Omega_R t}{2}) \tag{2.35}$$

$$\mathcal{P}_{|1\rangle}(t) = \langle 1\rangle\, \Psi = |c_1(t)|^2 = \sin^2(\frac{\Omega_R t}{2}). \tag{2.36}$$

The system varies with a period of $t = 2\pi/\Omega_R$ between states $|0\rangle$ and $|1\rangle$, but the phase is inverted. After $4\pi/\Omega_R$ the state reverts to its original condition. Microwave irradiation of a π/Ω_R duration inverts the state's occupation, and duration of $\pi/2\Omega_R$ creates a 50:50 superposition between the two states. These periodic changes in occupation numbers are known as Rabi oscillations. Using portions of these periods in the form of pulsed

signals can thus be used to manipulate the qubit state; it therefore constitutes one of the possible single qubit quantum gates (see section 2.1.4). These pulses are referred to by their ration to π to intuit their function. They need to be adjusted to correct microwave intensity and duration according to the Rabi frequency. One can create a microwave pulse by interrupting a continuous signal, but one must bare in mind the finite degree of slope as regards the flanks of the pulse. This means the pulse will not have a constant field strength $\mathcal{E}_0$. Thus it is necessary to define a pulse area Θ in exchange for $\Omega_R t$ with

$$\Theta = \left| \frac{\mu_{12}}{\hbar} \int_{-\infty}^{\infty} \mathcal{E}_0(t) dt \right|. \tag{2.37}$$

In the off-resonant case, we introduce an effective Rabi frequency Ω, such that [CTDL92]:

$$\mathcal{P}_{|1\rangle}(t) = \frac{\Omega_R^2}{\Omega^2}, \tag{2.38}$$

which uses the effective oscillation frequency

$$\Omega^2 = \Omega_R^2 + \Delta\omega^2. \tag{2.39}$$

In order to observe Rabi oscillations on an ensemble of spin systems, the medium must first be polarized. Otherwise, the signal of the Rabi oscillation would be largely canceled out in the mixture of states. The polarization caused by the Boltzmann distribution of spins in thermal equilibrium is negligible. In case of NV centers, polarization can be achieved by constant illumination (see section 3).

Damping of Rabi oscillations by dephasing Spontaneous emission causes another limit for arbitrarily long quantum state manipulation processes. Rabi oscillations experience damping due to a loss of coherence. Two processes, which are described in section 2.2.6, the spin relaxation and the dephasing, may be characterized by the decay rates T_1 and T_2.

For the damped case (decay rate γ), the time evolution of the probability c_1 is expressed as [Fox06]:

$$|c_1(t)|^2 = \frac{1}{2(1+2(\gamma/\Omega_R)^2)} \left(1 - \left(\cos\Omega' t + \frac{3(\gamma/\Omega_R)}{(4-(\gamma/\Omega_R)^2)^{1/2}} \sin\Omega' t\right) e^{-2\gamma t/2}\right), \tag{2.40}$$

with $\Omega' = \Omega_R\sqrt{1-(\gamma/\Omega_R)^2/4}$. The asymptotic limit of this is an equal occupation distribution of the basis states $|c_1|^2 = |c_0|^2 = 1/2$. For $\gamma = 0$ one obtains the special case of the undamped Rabi oscillation.

When $\gamma = 2\Omega_R$ then $\Omega' = 0$, resulting in a case of no further oscillation any more. Should even stronger damping occur, the oscillation is reduced to a slope reaching equilibrium faster and faster.

2.2.4 Spin state measurement

The matrices representing the spin projection along an axis are given by 2×2-matrices

$$S_x = \frac{\hbar}{2}\sigma_x \ , \ S_y = \frac{\hbar}{2}\sigma_y \ , \ S_z = \frac{\hbar}{2}\sigma_z, \tag{2.41}$$

with σ_i being the Pauli matrices [WKN01]

$$\sigma_x = \begin{pmatrix} 0 & 1 \\ 1 & 0 \end{pmatrix} \ , \ \sigma_y = \begin{pmatrix} 0 & -i \\ i & 0 \end{pmatrix} \ , \ \sigma_z = \begin{pmatrix} 1 & 0 \\ 0 & -1 \end{pmatrix}, \tag{2.42}$$

which span a complete and closed vector space. The eigenstates of σ_z are the qubit basis states and the NV axis will therefore be set to be the z-axis for low magnetic fields:

$$|0\rangle = \begin{pmatrix} 1 \\ 0 \end{pmatrix} \ , \ |1\rangle = \begin{pmatrix} 0 \\ 1 \end{pmatrix}, \tag{2.43}$$

It is noteworthy that the eigenstates of the observable σ_z can be measured simultaneously with those of the $\vec{S}^2$ observable but not with σ_y or σ_z. This is the case as the Pauli matrices do not commute [CTDL92]:

$$[\sigma_i, \sigma_j] = 2i\epsilon_{ijk}\sigma_k. \tag{2.44}$$

2.2.5 Quantum-mechanical treatment of spin transitions

The Hamiltonian describing the interaction of a spin $\vec{S}$ with an external magnetic field $\vec{B}$ is expressed as:

$$\hat{H} = -\vec{\mu}\vec{B} = -\gamma\hbar\vec{S}\vec{B}. \tag{2.45}$$

Assuming a magnetic field B_0 along the z-axis one can simplify, using the eigenvalues of the spin operator regarding that axis:

$$\hat{H} = -\gamma\hbar m_s B_0. \tag{2.46}$$

In order to flip the spin by $\Delta m_= \pm 1$, a photon of energy $\Delta E = E_{Photon} = h\nu$ [4] has to be absorbed. Due to selection rules for magnetic dipole transitions, only changes of the spin projection quantum number $m_s = 0, \pm 1$ are allowed. Therefore only energy changes of $\Delta E = \gamma\hbar B_0$ are allowed. Therefore, resonance occurs when

$$\omega = \gamma B_0, \tag{2.47}$$

which is in compliance with classical treatment.

[4] $\nu = \omega/2\pi$

2.2.6 Spin relaxation and dephasing

In a closed system without energy dissipation a photon field can change the spin to its state of higher energy, and that energy is returned to the field when the spin reverts to the lower energy state again, providing energy for the next spin state change. Therefore, the time-averaged spin populations will not be affected by the radiation field. Some form of damping is necessary to observe spin population changes. If the magnetic field is low enough, such that the Zeeman energy $\gamma\hbar B_0$ ($h = 6.6 \times 10^{-34}\,\mathrm{Js} = \hbar/2\pi$, the electronic gyromagnetic ratio $\gamma_e/2\pi = -28\,\mathrm{GHz/T}$) comes into the region of thermal interaction energies $k_B T$ ($k_B = 1.38 \cdot 10^{-23}\,\mathrm{J/K}$ being the Boltzmann constant, T being the temperature in Kelvin), the energy stored in the orientation of the magnetic moment can be passed on via dipole interaction to any reservoir. Therefore, the spin population distribution will adjust towards the population distribution of the reservoir within a period of time. That adjustment towards equilibrium is called relaxation. That distribution results in a macroscopic measure, the magnetization of a system $\vec{M} = \sum \vec{\mu}$. The spin populations thermalize towards a Boltzmann distribution,

$$N(m_s) \propto e^{\gamma\hbar B_0 m_s / k_B T}. \tag{2.48}$$

When temperatures increase or Zeeman energies become smaller, the distribution approaches an equal occupation of the states. Therefore, the assumption of

$$\gamma\hbar B_0 \ll k_B T, \tag{2.49}$$

which is called high temperature approximation, leads to a model with small differences in population numbers and therefore minimal net equilibrium magnetization. The magnetization can be derived from the Maxwell-Boltzmann distribution, using the high temperature approximation resulting in Curie's law,

$$M_0 = \chi_0 B_0 = \frac{N\gamma^2 S(S+1)}{3k_B T} B_0. \tag{2.50}$$

This shows a $1/T$ dependence for the magnetic susceptibility χ. It is easily apparent that the high temperature approximation is valid for typical applications at room temperature: e.g. $T = 300\,\mathrm{K}$, $B_0 = 1\,\mathrm{T}$ results in $1.8^{-23} \ll 4.1 \times 10^{-21}\,\mathrm{J}$, which clearly fulfills the requirement for that approximation.

By irradiating such a damped spin population with resonant radiation, one can partially invert[5] population numbers and then observe the relaxation which can be divided in two separate mechanisms:

- Spin-lattice-relaxation: T_1 is the time that represents the decay constant of an off-equilibrium magnetization $\vec{M}$ back towards its equilibrium M_0. It is also called longitudinal relaxation.

[5] The maximum population inversion is achieved when an equilibrium of excitation rate and decay rate of the spin polarization is reached

- Spin-spin relaxation: T_2 is the time that represents the decay constant of the magnetization components perpendicular to the magnetic field direction of an off-equilibrium magnetization towards the equilibrium. It represents the dephasing of the orientation of the spins transverse to the axis pf precession; thus, it is called transversal relaxation.

The Bloch equations express the evolution of magnetization towards thermal equilibrium in the presence of a magnetic field $\vec{B}$ via relaxation. Assume N represents the population number of the respective state, whereas $(+)$ and $(-)$ would denote two possible spin states:

$$\Sigma N = N_+ + N_- \tag{2.51}$$
$$\Delta N = N_+ - N_- \tag{2.52}$$
$$N_+ = \frac{1}{2}(\Sigma N + \Delta N) \tag{2.53}$$
$$N_- = \frac{1}{2}(\Sigma N - \Delta N) \tag{2.54}$$

The time-evolution of the states is the sum of rates into and out of a state, dependent on the current population N from which the transition starts and the probability W for such a transition:

$$\frac{dN_+}{dt} = N_- W_+ - N_+ W_- = -\frac{dN_-}{dt}, \tag{2.55}$$

where W_+ and W_- are the probabilities for a transition into the respective states. The last equivalence rises from the fact that there are just two states available and spins cannot get lost.

When a spin aligns with an external magnetic field, its potential energy regarding that field decreases. This energy is transformed into heat. Heat in reverse prohibits the complete polarization of the spins. The equilibrium with the heat bath is reached when the relative difference of the population corresponds to the temperature of the system. Therefore a Boltzmann distribution can be found in equilibrium [Sli90]. As a consequence, the probabilities can never be equal (as is always the case in quantum mechanics, but that problem will be resolved later):

$$\frac{dN_+}{dt} = 0 \Rightarrow e^{\frac{-\gamma\hbar B_0}{k_B T}} = \frac{N_-^0}{N_+^0} = \frac{W_-^0}{W_+^0} \neq 0. \tag{2.56}$$

As mentioned before, there needs to be a reservoir in exchange with the spin system to allow magnetization and relaxation. For each transition from $N_- \rightarrow N_+$ in the observed spin system, a transition $N_b \rightarrow N_a$ needs to occur in the bath. The probability for that is equal, so we will simply call it exchange probability: $W_{-b\rightarrow+a} = W_{-b\rightarrow+a} = W_{exc}$.

As the rate is $\frac{dN_{-\to+}}{dt} = N_- W_+ = N_- N_b W_{exc}$, one can calculate the probability $W_+ = N_b W_{exc}$. This can be done for the opposite transition accordingly. Considering that the reservoir is in equilibrium $N_-^0/N_+^0 = N_a/N_b$, it becomes clear that the difference between W_- and W_+ does not violate any rules of quantum mechanics but simply arises from different occupation numbers. The dynamics of the population difference can now be calculated:

$$\begin{aligned}
\frac{d\,\Delta N}{dt} &= \frac{dN_+}{dt} - \frac{dN_-}{dt} && (2.57)\\
&= 2\frac{dN_+}{dt} && (2.58)\\
&= 2(N_- W_+ - N_+ W_-) && (2.59)\\
&= (\Sigma N - \Delta N)W_+ - (\Sigma N + \Delta N)W_- && (2.60)\\
&= \Sigma N(W_+ - W_-) - \Delta N(W_+ + W_-) && (2.61)\\
&= \left(\Sigma N \frac{W_+ - W_-}{W_+ + W_-} - \Delta N\right)(W_+ + W_-). && (2.62)
\end{aligned}$$

By introducing the substitution $\Delta N_0 = \Sigma N \frac{W_+ - W_-}{W_+ + W_-}$ and the definition $\frac{1}{T_1} = W_+ + W_-$, one obtains [Sli90]:

$$\frac{d\,\Delta N}{dt} = \frac{\Delta N_0 - \Delta N}{T_1}. \tag{2.63}$$

The population difference ΔN corresponds to the magnetization M_z and the equilibrium difference ΔN_0 equals the magnetization M_0 when equilibrium is reached. Finally, one needs to add the rotation of the frame to obtain the Bloch equation for the z-component:

$$\frac{dM_z}{dt} = (\vec{M} \times \gamma \vec{B})_z + \frac{M_0 - M_z}{T_1}. \tag{2.64}$$

The components in x- and y-direction are decay as well, but there are no equilibrium magnetizations perpendicular to the field applied. As the reason for the decay of the transversal components as regards the magnetization is a different one, the decay constant for these Bloch equations is a different one accordingly:

$$\frac{dM_{x,y}}{dt} = (\vec{M} \times \gamma \vec{B})_{x,y} + \frac{-M_{x,y}}{T_2}. \tag{2.65}$$

In a static magnetic field the T_1-relaxation reduces the energy of the spin system, whereas the T_2-relaxation is energy conserving, which renders the decay processes distinguishable. The theoretical limits are [Lev08]

$$2T_1 \geq T_2 \geq T_2^*, \tag{2.66}$$

where T_2^* is an effective T_2 time-constant, as it includes local effects that enhance the decay of the phase coherence (like inhomogenous line broadening), which can be removed by spin echo techniques (see 6.2.2):

$$\frac{1}{T_2^*} = \frac{1}{T_2} + \gamma \Delta \vec{B}. \tag{2.67}$$

The line shape of a spin transition is a Lorentzian, which can be derived from the Bloch equations for low fields [Lev08]. The mean of this distribution, corresponding to the angular velocity of the rotating net magnetization, is the Larmor frequency ω_0. The width, more precisely the full width at half maximum (FWHM) of that spectral distribution, corresponds to the inverse decay time T_2^*:

$$\Gamma = \frac{1}{\pi T_2^*}. \tag{2.68}$$

3 The nitrogen vacancy defect center (NV) in diamond

3.1 Properties of diamond

A diamond is not just a precious gem, but as a material also possesses a lot of interesting physical properties. Knowing these is useful to understand the properties of the NV as well as the advantages and limitation of the material in the manufacturing process.

3.1.1 Lattice structure

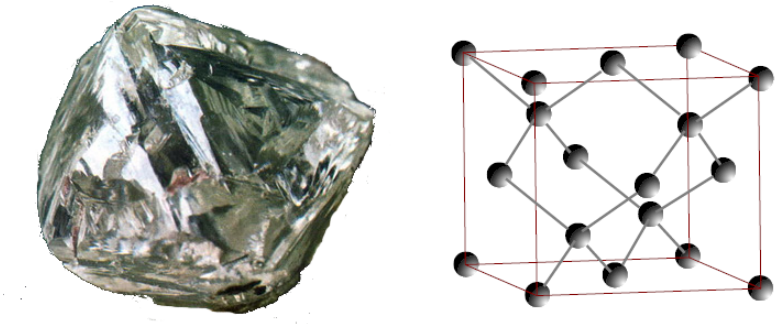

Figure 3.1: A diamond sample with its typical octahedral crystal habit and the elementary cell of the diamond crystal lattice.

Pure diamond is exclusively composed of carbon atoms that are held together by strong covalent electronic bonds. As the carbon is sp^3 hybridized it has four adjacent neighbours in the lattice. To maximize their distances they are arranged on the corners of a tetrahedron, the directions between any neighbors being:

$$\vec{n}_1 = \sqrt{3}\begin{pmatrix}-1\\-1\\-1\end{pmatrix}\ \vec{n}_2 = \sqrt{3}\begin{pmatrix}1\\-1\\1\end{pmatrix}\ \vec{n}_3 = \sqrt{3}\begin{pmatrix}1\\1\\-1\end{pmatrix}\ \vec{n}_4 = \sqrt{3}\begin{pmatrix}-1\\1\\1\end{pmatrix}. \tag{3.1}$$

This results in a face-centerd (fcc) cubic lattice with atoms positioned at (0 0 0) and $(\frac{1}{4}\frac{1}{4}\frac{1}{4})$ in the elementary cell. The elementary lattice cell consists of 8 carbon atoms. The lattice constant is 3.57 Å at 300 K and the distance between two neighboring carbon atoms is 1.546 Å. Diamond has a density of 3.5 kg/m^3 and therefore there are 1.763×10^{11} carbon atoms in one µm^3 [Pie95].

3.1.2 Material properties

3.1.2.1 Physical properties

The strong covalent bonding results in the diamond's great hardness of 10 on the Mohs scale. Nevertheless, it has to be handled with care as it is possible to cleave the crystal along the (1 1 1) plane easily, especially if thin samples are used. The extreme stiffness of the structure results in the highest thermal conductivity of 2200 W/K m, which proves useful when it comes to heat dissipation from the micro structure that is built upon the diamond surface in the course of this thesis.

The spectral transmission window reaches from 225 nm to the far infra-red, allowing measurement of optical activity of various defects and impurities in the form of peaks and bands in the optical absorption and fluorescence spectrum. The large band-gap of 5.46 eV allows to explicitly excite many levels of various defects and impurities within that range, which allows detailed study on those and even manipulation of energy level occupation. The large band-gap is also responsible for the diamond being a good electric insulator with a resistivity of about 10^{11} to $10^{18}\,\Omega$m[Mat11]. The dielectric constant of diamond is 5.5; the small diamagnetic effect (χ_v = -2.1×10^{-5}) can be neglected. Another property relevant for the following considerations is the very small electromagnetic loss tangent $\tan\delta$ (at 140 GHz, roomtemperature) $< 2 \cdot 10^{-5}$ [Mat11].

3.1.2.2 Chemical properties

Diamond is chemically quite inert, which is of great benefit in cleaning and manufacturing processes. Diamond is a metastable phase under normal conditions, which converts to graphite, when the necessary activation energy for the conformation change has been reached (900°C at standard pressure). Diamond oxidises in air at about 700°C, and can be dissolved in metal melts, but it can withstand every acid or solvent up to temperatures of 700°C [RFR99].

3.1.3 Types of diamonds

Diamond can be classified according to it's spectral properties:

- Type I: These diamonds absorb ultraviolet light above 320 nm and have a major absorption band in the infra-red region at 8 µm [RFM34]. They have a high nitrogen content (up to 0.3 %, but usually at least about 100 ppm[1]) [KB59]. Diamonds of type I are subdivided according to the configuration of the impurities.
  - Type Ia: About 98 % of all natural diamonds are of that type and mostly have a yellow tint due to the N2 and N3 center. Most defects are clustered nitrogen conglomerates like the A, B, N2 and N3 center.

[1] 1 ppm is equivalent to about 10^{17} carbon atoms per cubic centimeter

  - Type Ib: This naturally rare type of diamond is usually created artificially by chemical vapour deposition (CVD), as the process disperses the nitrogen to form C-centers. As these diamonds additionally absorb green light they are darker and usually show a yellow or brown tint.

- Type II: These diamonds absorb ultraviolet light at frequencies above 225 nm and show no band at 8 µm , which is explained by the lack of nitrogen impurities (the nitrogen content ranges from 4 to 40 ppm).
  - Type IIa: About 1-2 % of all natural diamonds are of type IIa. They are almost completely free of impurities, therefore they lack most absorption bands.
  - Type IIb: These diamonds are comparatively free of impurities except for boron, which gives these diamonds a blue or grey tint. Boron is especially interesting as it causes these diamonds to be p-type conductors.

3.1.4 Defect centers

The aforementioned defects are just the most common of dozens of naturally and artificial defects found in diamond. As defects play a major role in the solid state physics of diamonds, the most relevant ones are listed here:

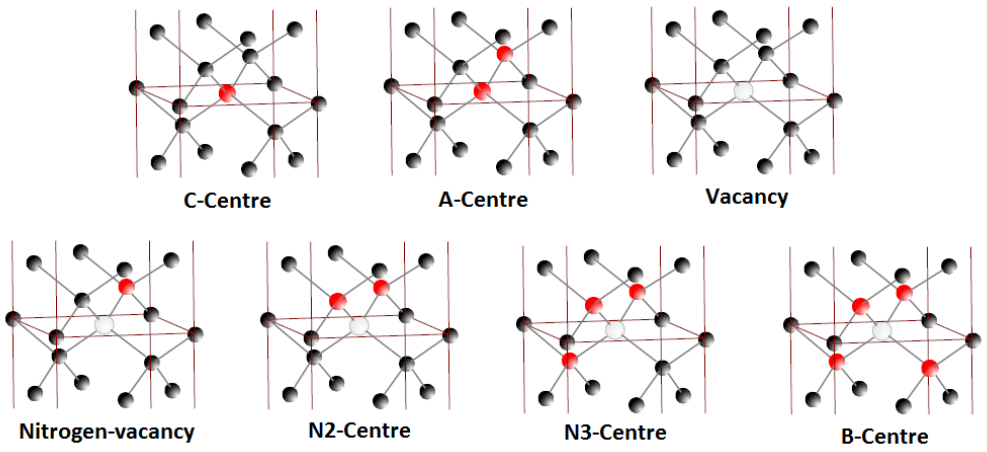

Figure 3.2: A selection of nitrogen and vacancy-related defect centers in diamond

- A-center: It is composed of two neighboring substitutional nitrogen atoms. It can be identified by a characteristic ultraviolet absorption band starting at 4 eV(310 nm)[Dav76] and just one stronger peak in infra-red absorption at 7.8 μm [2], which is often used to determine the Type A defect concentration. If this defect is highly concentrated, one classifies the sample as type IaA diamond [Zai01].

[2] 1282 cm^{-1}

- C-center: These are single substitutional nitrogen atoms. They are rarely found in natural diamonds. It has an infra-red local mode of vibration at 7.440 µm [3], just above the Raman frequency of diamond (7.505 µm [4]). The nitrogen has a substantial relaxation towards the plane of three neighboring carbon atoms, which results in a deep donor, with an electric level of 1.9 eV below the conductive band minimum. The distance increase is about 28% [Mai94]. Another characteristic optical absorption is found at 8.850 µm [5]. As they are easily observed im electron paramagnetic resonance spectra, they are also named P1-center [SSGL59]. This configuration is mainly found in synthetic diamonds [Zai01].

- Vacancy: One of the most common crystal defects is the isolated vacancy. Vacancies are naturally formed in the crystallization process and develop through exposure to heat and radiation as well as plastic deformation. For studies they can be artificially created, for example by irradiating the diamond with accelerated electrons (above 200 keV) or neutrons. Single vacancies have sharp zero phonon lines at 1.673 eV (GR1) and 3.150 eV (ND1). Vacancies tend to move through the crystal most easily when it is heated to above 800°C [ILTT05]. The energy necessary for moving a vacancy through pure diamond is 2.3 eV ±0.2 eV [Mai94]. Thus, vacancies and carbon interstitials can neutralise each other, which is utilized to repair diamonds and increase their transparency. Moving vacancies regularly get trapped beside other impurities forming new defect centers [DP65] [DLC+92].

- B-center: This is a cluster of four substitutional nitrogen atoms around a vacancy, which does not show any optical activity, except for a sharp infra-red line at 8.85 µm [6]. Diamonds that have a high B-center concentration are especially colourless and constitute a separate subcategory called type IaB [Zai01].

- N2- and N3-center: This is a cluster of two respectively three substitutional nitrogen atoms around a vacancy. The N3-center has a characteristic absorption and luminescence line at 415 nm and is not visible by itself, but as it is always accompanied by N2-centers which absorb (but not emit) light at 478 nm and thus create the common yellow color.

- Nitrogen-vacancy: This defect is composed of a single nitrogen impurity situated next to a vacancy. Its remarkable properties are central to this thesis, so the next section will be dedicated to this defect.

[3] 1344 cm^{-1}
[4] 1332.5 cm^{-1}
[5] 1130 cm^{-1}
[6] 1129 cm^{-1}

3.2 Properties of the NV defect center

3.2.1 Structure and creation

As the NV consists of a substitutional nitrogen atom neighbouring a vacancy, there are three lattice sites left next to the vacancy, which are occupied by carbon atoms. Therefore, this system exhibits a three-fold symmetry, technically termed C_{3v}-symmetry, with an axis of threefold rotational symmetry through nitrogen and vacancy, pointing in a [1 1 1] direction [Dav76]. The vacancy is surrounded by five dangling bonds, one electron from each carbon and two from the nitrogen, which form electronic orbitals within the vacancy. Such an object is called NV_0. A sixth electron may bind to the defect, possibly donated by a close nitrogen impurity [MHS06], forming a NV^-. As this is the more frequent type of NV; this abbreviation will refer to the negatively charged configuration from now on.

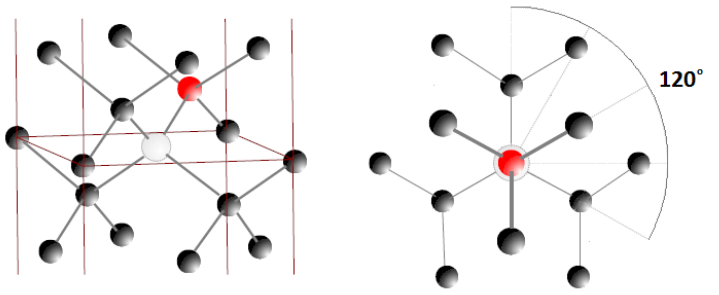

Figure 3.3: Two different views of the nitrogen vacancy defect centre

According to Hund's law, the four electrons will become pairs, occupying the first two orbitals with no angular momentum[7]. The two electrons left will be in orbitals of angular non-zero momentum, meaning there are three orbits with $m_l = 1, 0, -1$. Therefore, the remaining electrons choose different angular momentum orbits, so the Pauli principle will not force the electrons to have unequal spin directions. As a result, the spin of the NV becomes 1 with the setting $m_s = 1, 0, -1$, a triplet state.

Spin measurements for the NV^- show that only 2 % of the spin density is found at the nitrogen, the unpaired electron spin density at the three equivalent nearest-neighbor carbon sites is on the order of 70 %. It has also been reported that the relaxation site of the nitrogen is shifted away from the vacancy at around 8 % increased bond length for the NV^-. The carbons bordering the vacancy move a little closer towards the vacancy. The electrons constituting the NV appear to be located at the nitrogen-far side of the vacancy [JW06].

[7] This would be s-orbitals in case of atoms

3.2.1.1 Creation and stability

As NV do not occur in sufficient densities naturally, techniques to increase these densities are needed in order to create diamond samples suitable for experiments investigating ensemble properties of NVs. Vacancies can be created by irradiating the sample with particles that, when colliding with resident carbon atoms, knock them out of their position into a random site in the lattice. The vacancies can then be stimulated to move through the lattice by applying heat to the sample. On their random walk it is likely for them to be trapped next to an abundantly occurring nitrogen impurity for energetic reasons described below.

In order to create homogeneous vacancy distributions over larger areas, particles with a rather small scattering cross section regarding carbon atoms are chosen. A possible choice are neutrons that are neutral and have a sufficient mass to transfer the necessary energy for kicking a carbon atom off its lattice site and far enough into the surrounding, such that a stable vacancy may be is formed. This needs about 32 eV to be transferred to the carbon atom, which requires neutrons of a kinetic energy higher than 100 eV [8]. Neutrons of energies below that threshold only heat the crystal or cause nuclear transformations. The scattering cross section of carbon for elastic collisions with neutrons is almost constant in the range of 10^{-1}-10^{6} MeV. The spectrum of neutrons largely available in a nuclear reactor performing fission of uranium nuclei ranges from prompt neutrons with energies of 4.8 MeV[9] to thermal neutrons with about 0.1 eV. The spectrum is almost flat in the range of 10^{2} to 10^{6} eV.

A different choice would be an electron beam, thus allowing a fine tuning the electron energy, whereas the reactor neutrons would have all possible velocities including prompt neutron and thermal neutron velocities. For kicking a carbon atom off its lattice site 32 eV are needed. Thus, the first advantage of electrons would be less destruction of the crystal lattice, which normally contributes to e.g. the measured ODMR spectra by broadening it, as there would then be a larger variety of dipole moments. The pushed-off carbon will not have enough energy to displace another carbon and the electron will not lose much energy, but due to its small cross section, it will not likely cause another collision within a reasonable area. This leads to the second advantage, which is that the sample would be enriched with vacancies with just a small gradient in density.

At temperatures of about 800°C vacancies start to diffuse through the crystal [ILTT05], eventually healing out, forming vacancy clusters or combining with nitrogen [DLC+92]. The energy necessary for moving a vacancy through pure diamond is about 2.3 eV ± 0.2 eV for a carbon atom swapping place with a vacancy. Nitrogen, in contrast, is not as easily moved, as the energy for swapping places with a carbon atom is about 6.3 eV (with experimental results of about 5 eV, varying highly, like 2.6 eV in Ref. 21

[8] This information is taken from an as yet unpublished source: Nöbauer et al. – Creation of ensembles of nitrogen-vacancy centres in diamond by neutron irradiation.

[9] This is the average kinetic energy of neutrons released instantly from the nuclear fission of uranium-235.

of [Mai94]). Vacancy assisted movements are expected to require an activation energy of 4.5 eV. It is energetically favorable to move vacancies next to nitrogen impurities so that they get trapped there [Mai94]. The NV is more stable than its constituent defects by 4.7 eV.

3.2.2 Energy levels

Using LCAO (Linear combination of atomic orbitals) theory the possible orbits can be derived from the geometry of the system using a group theoretical approach (for a short summary, see 8.3) [MW70], but the complete structure is not as yet known [AJBB11]. The orbitals derived are labeled with a Mullikan symbol, each referring to an irreducible representation of the respective element of the symmetry group. According to LCAO a system of C_{3v}-symmetry possesses the following four orbitals:

- $^1A_1$: A non-degenerate singlet state, symmetrical regarding the principal axis
- $^3A_2$: A non degenerate anti-symmetric triplet state
- ^1E: A singlet state with twofold degeneracy
- ^3E: A triplet state with twofold degeneracy

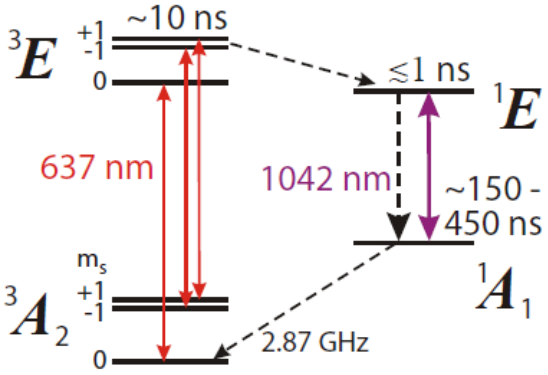

Figure 3.4: This is the currently assumed energy level scheme of the NV defect centre proposed by Acosta et al. [AJBB11].

According to the current assumptions [AJBB11] these four states can be assigned to the following levels:

- $^3A_2$: Ground state, a spin triplet state [RMK87].
- ^3E: Excited state, a triplet with a lifetime of 13 ns [MHS06].
- ^1E: Intermediate state, a singlet with lifetime < 1 ns [MHS06].

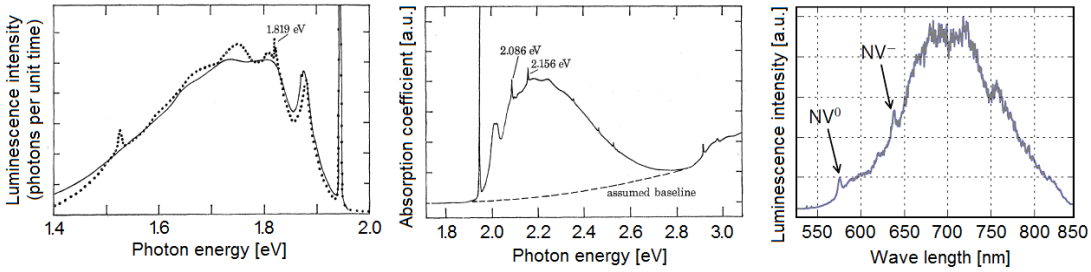

Figure 3.5: The image to the left shows the luminescence spectrum of an irradiated and annealed diamond sample at liquid nitrogen temperatures as a dotted line recorded by Davies et al. in 1976. This is compared to the luminescence calculated from the absorption spectrum (continuous line). The associated absorption spectrum is depicted in the center image. The image to the right shows the luminescence spectrum measured at room temperature, with the experimental set-up used during this thesis project. It was carried out by Stefan Putz in 2010 [Put11].

- $^1A_1$: Metastable state, a singlet with a long lifetime of about 150−450 ns [AJBB11].

The levels are linked by the following transitions:

- $^3A_2 \rightarrow {}^3E$: Optical excitation via 637 nm [10] zero-phonon line (ZPL)[11][DH76] and upper phonon side-band[12].
- $^3E \rightarrow {}^3A_2$: Optical decay at the ZPL and lower phonon side-band.
- $^3E \rightarrow {}^1E$: Inter-system-crossing (ISC)[JPG+02] of small energy change [JPG+02]. It is spin selective: almost exclusively $m_s = \pm 1 \rightarrow m_s = 0$ is allowed.
- $^1E \rightarrow {}^1A_1$: Infra-red decay at 1042 nm.
- $^1A_1 \rightarrow {}^3A_2$: Non-radiative decay.

3.2.2.1 Fluorescence time trace & spin polarization

The observation that fluorescence of NVs under constant illumination does not reach its maximum immediately leads one to assume the presence of a non-radiative decay channel, which depletes its own source, a spin population, by transferring it into another

[10] In literature it is commonly referred to as 1.945 eV line.
[11] It can be discerned from an NV^0 by its ZPL: 575 nm.
[12] The phonon side band contributes a major portion of the absorption/fluorescence intensity at higher/lower frequencies. At room temperature, around 97% of the fluorescence is contributed by emissions into the phonon side-band, and even at liquid helium temperatures only a minimal percentage of the emitted light will contribute to the ZPL [Chi07]. Still, the ZPL peak is visible at room temperature.

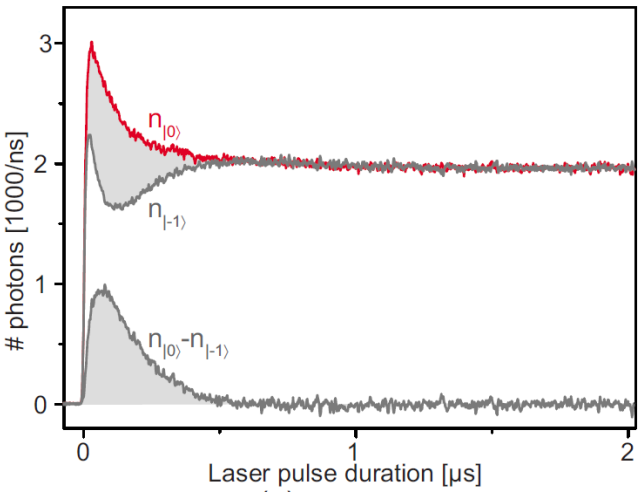

Figure 3.6: The measurement of the fluorescence intensity under constant illumination shows a different time dependence for the bright and dark states. Integrating over the photon counts until equilibrium has been reached allows statistical determination the state of the of the quantum system [SNB+10].

spin state. ${}^1E$ is accessed from ${}^3E$ via ISC[13], thereby transforming $m_s = \pm 1$ to $m_s = 0$. The small energy step [14] and a fast decay to ${}^1A_1$, which prevents a back transition, causes relevant competition with the optical decay. The time constant until a steady state has been attained is mainly determined by the long-lived state ${}^1A_1$. The depleted spin population, $m_s = \pm 1$, is called the "dark state", whereas $m_s = 0$ is referred to as the "bright state". A spin polarization into $m_s = 0$ reaches 80 % after about 3 µs [Put11]. Polarization is rather stable, as arbitrary spin flips only occur every 10^5 cycles [Chi07].

If one starts in a polarized $m_s = 0$ one can observe a fluorescence intensity peak – 30 % above the equilibrium – immediately when illumination starts, decaying to equilibrium within about 1 µs. If one starts in the $m_s = \pm 1$ state, one can observe a sharp drop of about 30 % below the equilibrium after the initial excited state has decayed. The dip occurs, because the NV is caught in the meta-stable state in a greater number of cases. Both time traces return to equilibrium after about 0.5 µs. Lifetime measurements cannot be performed by recording a single decay, because state of the art time-tagger have a resolution of about 300 kHz, whereas several MHz would be necessary [Put11].

[13] An ISC process involves an exchange of the spin with a neighboring moment via spin-spin or spin-orbit coupling.
[14] A large orbital overlap increases the transition probability of an ISC.

3.2.2.2 Fine-structure & Zero-field splitting

The ground[15][RMK87] and the excited state [HHM84] are spin triplet states. As the triplet states are created from two unpaired spins $\vec{S}_1, \vec{S}_2$, which are interacting via dipole-dipole coupling, one can expect interaction energy, even without any external magnetic field being present. Therefore, the energy shift caused by that interaction splits up the energy levels of the spin states and it is called zero-field-splitting. This effect is understood as a part of the fine structure of the electronic term scheme.

The interaction of two spins is dependent on their relative position to each other. In order to derive stationary behaviour [HW02], one time-averages over positions, resulting in spatial distributions of spin densities. If that distribution is distorted out of its spherical geometry, the Hamiltonian $\hat{\mathcal{H}}_{\mathrm{ZFS}}$ has to be calculated using an interaction tensor D:

$$\hat{\mathcal{H}}_{\mathrm{ZFS}} = \vec{S}^{\dagger} D \vec{S} = \sum F_{ij} S_i S_j, \tag{3.2}$$

where S is the spin and $i, j = x, y, z$. The tensor F (derivation see 8.5) can be diagonalized to form

$$F = \begin{pmatrix} -\frac{1}{3}D + E & 0 & 0 \\ 0 & -\frac{1}{3}D - E & 0 \\ 0 & 0 & -\frac{2}{3}D \end{pmatrix} \tag{3.3}$$

with the fine structure constants

$$D \propto \int \Psi^* \left(\frac{r_{12}^2 - 3z_{12}^2}{r_{12}^5} \right) \Psi \, d^3r_1 \, d^3r_2 \quad \text{and} \quad E \propto \int \Psi^* \left(\frac{x_{12}^2 - y_{12}^2}{r_{12}^5} \right) \Psi \, d^3r_1 \, d^3r_2, \tag{3.4}$$

with the orbital coordinates $\vec{r}_{12}$ and their respective components, along with the wave-function Ψ of the crystal orbital.

The Hamiltonian can thus be rewritten as:

$$\hat{\mathcal{H}}_{\mathrm{zfs}} = \frac{1}{\hbar^2} \left[D \left(S_z^3 - \frac{1}{3}\vec{S}^2 \right) + E(S_x^2 - S_y^2) \right]. \tag{3.5}$$

In spectroscopy, energy measurements are limited to the detection of energy differences between electronic levels; therefore, the $m_s = 0$ state is chosen to be the offset. Therefore, spin state $m_s = 1$ is found at an energy $D+E$, and $m_s = -1$ is found at $D-E$.

In the case of the NV, the crystal orbital of the ground and excited state is of threefold symmetry. This means one axis is distinguished, causing a finite D. For an ideal geometry, E would be zero, but due to lattice strain and effects of impurities this, is

[15] The ground state is visible in ESR measurements exclusively under illumination [LW78] and was correctly assigned using spectral hole burning [RMK87].

almost never the case. The splitting D is different for the ground and excited triplet state of the NV.

Experimentally, $D_g = 2.87\,\mathrm{GHz}$ and $D_e = 1.4\,\mathrm{GHz}$ were measured [NKJ+09]. The fine structure constant E_e was measured to be $\ll 50\,\mathrm{MHz}$ for NVs in ultra pure diamond of the type IIa [NKJ+09], but may be on the order of tens of GHz as well [RMK87].

3.2.3 Luminescence of NV centers

3.2.3.1 Intensity

To evaluate the maximum steady-state fluorescence intensity of a single NV one needs to take the transition rates k_{ij} between the contributing levels (here i,j = 1,2,3) into account. Not all level changes are significantly relevant. For an internally un-branched decay channel of multiple levels all the internal decay and excitation transition rates can be accumulated into one. For a rate equation it matters how many transitions into and out of the channel are occurring. Therefore the intermediate state $^1\mathrm{E}$ and the meta-stable state $^1\mathrm{A}_1$ can be condensed to state "3". Further excitations into the decay channel and from there into the optical excited state can be dispensed with, as they are smaller than the corresponding decay rates. The transition rate of the optical excitation is dependent on the optical pumping. The system saturates upon increasing the pumping power, therefore the maximum fluorescence intensity can be derived for the limit of infinite pumping power. Only three transition rates appear in the formula derived by [MSH+08]:

- k_{21}: the optical transition rate from the exited state $^3\mathrm{E}$ to the ground state $^3\mathrm{A}_2$
- k_{23}: the transition rate from $^3\mathrm{E}$ into the dark decay channel
- k_{31}: the transition rate from the dark channel into the ground state.

Finally, the fluorescence quantum yield Φ_F contributes to the result:

$$I_{max} = \frac{k_{31}(k_{21} + k_{32})\Phi_F}{2k_{31} + k_{32}}. \tag{3.6}$$

For a single NV, saturation can be observed with our experimental set-up (see figure 3.7). Observed fluorescence rates are typically on the order of $10^5\,\mathrm{s}^{-1}$[JW06] at room temperature. In contrast, the calculated fluorescence rate is on the order of $10^7\,\mathrm{s}^{-1}$, therefore the detection efficiency is about 1 %. The saturation power of the experimental set-up is about 0.2 mW. For ensemble NV samples, no saturation effect can be observed due to the high number of NVs involved; therefore, only the linear range of the saturation curve can be observed.

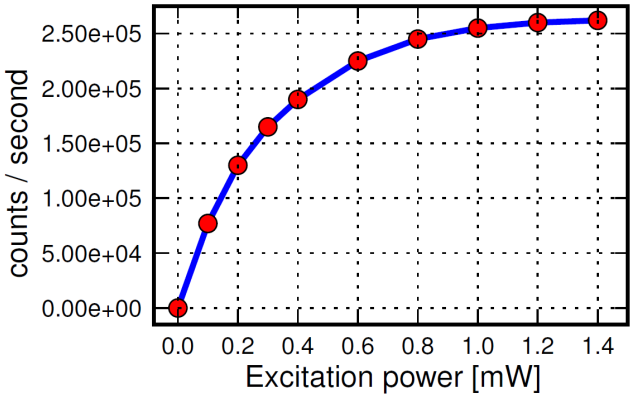

Figure 3.7: This image shows the saturation curve of a single NV measured at room temperature with 532 nm excitation wavelength [Put11].

3.2.3.2 Photon statistics

Several experiments on quantum computation involve single NVs, so we need to ensure that only one NV is present inside the confocal volume.[16]
As our type IIa CVD diamonds feature about one NV per μm^3 with decreasing density towards the surface[17] it is quite likely to observe unresolvable clusters of NVs. To determine whether such photon sources contain a single emitter, one may hold to the fact that a single emitter will never emit two photons at the same time, whereas two emitters may do so by coincidence. Longer delays between photons become more likely in both cases, essentially showing a completely random distribution for long time intervals between emissions. Such behaviour can be described by correlation functions.

Correlation function In statistics a correlation describes the degree to which two statistical variables vary in tandem. The correlation coefficient can vary from one, which means a perfect matching of two sequences of statistical data to zero, which in turn, means there is no relationship between the sequences, to -1, which again means that there is an inverse correlation. If an ordered sequence of statistical variables (e.g. the time-distribution of photon counter clicks) is compared to itself at a different time τ, it is called auto-correlation. The function representing the correlation coefficients for all potential times is called correlation function.

[16] Diamond density: 3,52 kg dm^{-3}, one Dalton: 1,66$*10^{-27}$ kg, carbon atom mass: 1,992$*10^{-26}$ kg, lattice sites: 1,767$*10^{29}$ m^{-3} = 1,767$*10^{11}$ μm^{-3}, one ppb (part per billion) $\hat{=}$176,7 μm^{-3}, nitrogen content (type IIa CVD diamond): <5 ppb $\hat{=}$ <885,5 μm^{-3}, NVs measured: 1 μm^{-3} $\hat{=}$ <1‰NVs/N., confocal volume: 2$*10^{-18}$ m^3 = 2 μm^3, atoms inside confocal volume: 3,534 $*10^{-11}$

[17] for unknown reasons, perhaps related to the production process

Hanbury Brown-Twiss interferometry The Hanbury Brown-Twiss interferometer was developed to measure the correlation of sequences of photon detection of photons from one source on two separate detectors. The photons are randomly distributed between the detectors, but the photon detection sequences exhibit the same statistical distribution.

If there were just one detector, two problems would arise. On the one hand an autocorrelation would show a perfect correlation for $\tau = 0$ for all kinds of behaviour, so no information would be gained through such a measurement. Unfortunately, correlations for photon measurements are only significant close to $\tau = 0$, and uncorrelated for long time shifts. For two detectors, this problem does not occur, because of the random selection of photons. The second disadvantage of s single detector would be its dead time after each photon detection. This disallows measurements of photons in close succession, and would thus distort the statistical behaviour. In case two detectors are used this problem is less severe, as only in 50 % of all cases two consecutive photons arrive at one detector; therefore, less information gets lost.

Correlation function of the photon detection Electromagnetic radiation can be characterized using the second-order coherence function [Ben09]. The coherence of two waves follows from how well correlated the waves are as quantified by the correlation function. For Hanbury Brown-Twiss interferometry the photon counter time traces at the two detectors are used to calculate correlation. Usually, a normalized second-order coherence function is used. For classical fields it can be written using the time-dependent intensity of the radiation [Ben09]:

$$g^{(2)}(\tau) = \frac{\langle I(t)\rangle\langle I(t+\tau)\rangle}{\langle I(t)\rangle^2}. \tag{3.7}$$

The quantum mechanical equivalent is expressed as [Ben09]:

$$g^{(2)}(\tau) = \frac{\langle a^\dagger(t)a(t)a^\dagger(t+\tau)a(t+\tau)\rangle}{\langle a^\dagger(t)a(t+\tau)\rangle^2}, \tag{3.8}$$

with $a^\dagger$ being the photon creation operator and a being the annihilation operator.

Types pf photon fields There are basically three cases of photon sources with different $g^{(2)}(\tau)$ [Ben09]:

- Chaotic light: Most commonly emitted from a thermal light source, the photons occur in bunches.[18]. This means the probability for shorter time intervals between emissions is increased.[Ben09]

[18] Assume a hot gas, whereby collisions change the phase but not the amplitude; the length of a continuous wave pattern is random. The summation of the complex field amplitude looks like a random walk; thus, even for a uniform emission rate the intensity, the squared absolute of the amplitude, varies. The probability for finding the amplitude of the beam in a specific amplitude interval is Gaussian distributed. Consequently the probability distribution for finding the intensity in a specific intensity interval has the shape of an exponential decay like the Boltzmann distribution, which itself is part of a Bose statistic. Multiple occupied states are thus favored [ue11].

$$g^{(2)}(0) \geq g^{(2)}(\tau) \approx 1 \tag{3.9}$$

- Poisson distributed light: Predominately known from laser-light, the states (also known as coherent states or Glauber states) of an electromagnetic field are eigenstates of the annihilation operator a ($a\,|\alpha\rangle = \alpha\,|\alpha\rangle$), and can be represented by Fock-states, states of known occupation number n (which means they are eigenstates of the number operator $N = \sum_k a_k^\dagger a_k$: $n\,|n\rangle = N\,|n\rangle$). For a minimal intensity fluctuation[19], $|\alpha\rangle$ obeys a Poisson-distribution regarding occupation numbers: $P(n) = |\langle n\rangle\,\alpha|^2 = e^{-|\alpha|^2}\frac{|\alpha|^{2n}}{n!}$. Therefore, it shows a completely random distribution of photons over time; delays are all equally probable [Ben09][Ska99]:

$$g^{(2)}(0) \equiv 1. \tag{3.10}$$

- Anti-bunching light: Ideally a single two-level system, which requires a finite duration to be excited again after emission. As emission and re-excitation are naturally broadened; this results in a delay distribution with a dip at zero delay [Ska99]:

$$g^{(2)}(0) = 1 - \frac{1}{N}, \tag{3.11}$$

  where N is the number of single photon emitters in the light source.

Experimentally, a correlation function presented by Jelezko and Wrachtrup [JW06] can be applied for typical single-NV measurements:

$$g^{(2)}(\tau) = 1 - (K+1)e^{k_1\tau} + Ke^{k_2\tau}, \tag{3.12}$$

with

- $k_{1,2} = -\frac{1}{2}P \pm \sqrt{\frac{1}{4}P^2 - Q}$
- $P = k_{21} + k_{12} + k_{23} + k_{31}$
- $Q = k_{31}(k_{21} + k_{12}) + k_{23}(k_{31} + k_{12})$
- $\frac{k_2 + k_{31} - k_{12}k_{23}/k_{31}}{k_1 - k_2}$.

[19] A coherent beam of light is especially known for its constant phase; therefore, the intensity must fluctuate maximally on a microscopic level. This equals a maximum randomness of the distances between photons, which is described by a Poisson-distribution.

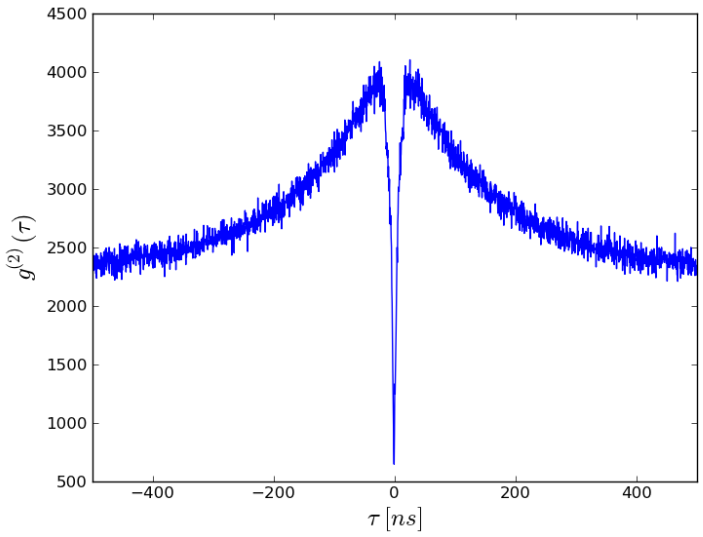

Figure 3.8: The photon count correlation measurement of a NV center shows a characteristic dip at $\tau = 0$, indicating that this light source is a single NV.

3.2.3.3 Power broadening

In a two-level system the excitation and decay rate determine the equilibrium occupation numbers of the energy levels. When a radiation field is present and the energy of its photons ($E_{photon} = \hbar\omega$ with ω being the angular frequency) is close to the energy difference between the ground and excited state ($\Delta E = E_{excited} - E_{ground}$) the following processes may occur:

- Absorption: A transition from ground to excited state is performed at the cost of a photon of the field.
- Spontaneous emission: An excited state decays to the ground state, thereby emitting a photon of an energy ΔE. The impulse of that photon has an arbitrary direction and the phase is random as well.
- Stimulated emission: A phonon of energy ΔE bypassing a system in an excited state will induce its decay into its ground state, but is not absorbed itself. Thereby a photon of the same energy, direction and phase, equalling the bypassing photon, will be emitted. Therefore, that process is used to create a beam of coherent light as it is utilized in lasers. Stimulated emission can be understood as a two-level system, more precisely an electric dipole interacting with a classical electromagnetic field [Sli90].

If the pumping power is low, so that the excitation probability is far smaller than the decay probability, the equilibrium settles at a high ground state occupation compared

to the excited state occupation. That low excited state occupation causes the effect of stimulated emission to have almost no contribution to the entire emission rate. Therefore, the line width is determined by the natural line broadening (and other non-power-dependent processes like the Doppler broadening).

For higher pumping power, stimulated emission becomes relevant. The dependency of the emission intensity from pumping power and the line broadening due to power increase can be derived from the rate equations of a pumped two-level system [ME10]:

$$\frac{dN_2}{dt} = -\frac{\sigma(\nu)}{h\nu} I_\nu (N_2 - N_1) - A_{21} N_2 \tag{3.13}$$

$$\frac{dN_1}{dt} = -\frac{\sigma(\nu)}{h\nu} I_\nu (N_2 - N_1) + A_{21} N_2, \tag{3.14}$$

where σ is the cross section in dependence on the transition wavelength λ, the spontaneous emission rate A_{21} and the line-shape function $S(\nu)$ as:

$$\sigma(\nu) = \frac{\lambda^2 A_{21}}{8\pi} S(\nu). \tag{3.15}$$

The line shape of natural broadening is a Lorentzian with FWHM $\delta\nu_0$:

$$S(\nu) = \frac{(1/\pi)\delta\nu_0}{(\nu - \nu_0)^2 + \delta\nu_0^2}. \tag{3.16}$$

The steady-state solutions $\bar{N}_2$ and $\bar{N}_1$ obtained by setting the derivatives equal to zero and introducing $N = N_1 + N_2$ are easily found to be

$$\bar{N}_2 = \frac{\sigma(\nu) I_\nu / h\nu}{A_{21} + 2\sigma(\nu) I_\nu / h\nu} N \tag{3.17}$$

$$\bar{N}_1 = \frac{A_{21} + \sigma(\nu) I_\nu / h\nu}{A_{21} + 2\sigma(\nu) I_\nu / h\nu} N. \tag{3.18}$$

Introducing the saturation intensity

$$I_\nu^{sat} = \frac{h\nu A_{21}}{2\sigma(\nu)}, \tag{3.19}$$

it is possible to calculate the relative occupation numbers

$$\frac{\bar{N}_2}{N} = \frac{\frac{1}{2} I_\nu / I_\nu^{sat}}{1 + I_\nu / I_\nu^{sat}} \tag{3.20}$$

$$\frac{\bar{N}_1}{N} = \frac{1 + \frac{1}{2} I_\nu / I_\nu^{sat}}{1 + I_\nu / I_\nu^{sat}}. \tag{3.21}$$

For low pumping power the ground state is almost fully occupied and the excited state almost empty. At the limit of strong pumping power the states are equally occupied.

The small signal absorption coefficient is expressed as

$$a_0(\nu) = \sigma(\nu)N. \tag{3.22}$$

The saturation intensity for increased pumping powers can be calculated from the above equations:

$$a(\nu) = \sigma(\nu)(\bar{N}_1 - \bar{N}_2) = \frac{a_0(\nu)}{1 + I_\nu / I_\nu^{sat}}. \tag{3.23}$$

After some simple algebra using equations 3.23, 3.15, 3.16 and 3.19, one can find that

$$a(\nu) = \frac{\lambda^2 A_{21}}{8\pi} N \frac{(1/\pi)\delta\nu_0}{(\nu - \nu_0)^2 + \delta\nu'^2_0} = a_0(\nu_0)\frac{(1/\pi)\delta\nu_0}{(\nu - \nu_0)^2 + \delta\nu'^2_0}, \tag{3.24}$$

with

$$\delta\nu'_0 = \delta\nu_0\sqrt{1 + I_\nu / I_{\nu_0}^{sat}}. \tag{3.25}$$

This increase of the line width with the pumping power is known as power broadening. It approaches a linear growth with the pumping power at the limit of high power. It has to be noted that the natural line broadening expressed in equation 3.16 is just one example for a line-shape. The Doppler broadening for instance is created due to the motion of the atoms of a medium interacting with the electromagnetic field, which causes red- and blue-shifts in the emitted frequency, which increases with temperature, and has a Gaussian line-shape, which in turn convolves with the other broadening shapes forming a Voigt-profile.

3.3 Spin measurement and manipulation using ODMR

Optically detected magnetic resonance spectroscopy is a technique to determine the spin state of specific molecules (and defect centers) by fluorescence measurements. Molecules suitable for this method must to exhibit different fluorescence intensities for their spin states. By exposition of the NV to an irradiated alternating magnetic field whose frequency is resonant with the spin transition, the distribution of occupation densities between the spin states can be shifted (see section 2.2.3). In order to obtain a shift which yields a distinct change of fluorescence intensity, the system needs to be initially spin-polarized or become polarized upon measurement.

The record of the fluorescence intensity as dependent on the frequency of the applied alternating magnetic field is called an ODMR spectrum. It is usually intended to detect resonance frequencies; thus in general, pulse lengths for driving decided spin transitions are unknown. Instead a continuous wave can be used, which increasingly balances the occupation densities of spin states upon approaching the resonance frequency of the spin transition.

In case of the NV the illumination exciting the fluorescence polarizes the spin into the $m_s = 0$ state, which provides the brighter luminescence compared to the $m_s = \pm 1$ states. Irradiation of microwaves close to their resonance frequency refills the $m_s = \pm 1$ state, and therefore creates a dip[20] in the ODMR spectrum.

When the resonance frequency is known, Rabi-oscillations can be observed (see 6.2.1) to determine the length of MW-pulses (especially pi- and pi-half-pulses) necessary for arbitrary spin manipulations. Pulse durations can be extracted from a fit of a damped sinus curve onto the recorded data of the Rabi-oscillation. The combination of Larmor precession and driven spin transitions can be theoretically used to perform any sequence of single qubit gates.

Due to the imperfect darkening of the $m_s = \pm 1$ state, fluorescence measurement of NV spin states delivers just such a statistical result. Additionally, the spin state prepared by a pulse sequence reverts inevitably to $m_s = 0$ by the illumination utilized for measurement. Thus, the fluorescence signal distinguishing the spin states is only a transient: The photon count within the first 0.5 µs is compared with the photon count at equilibrium (see 3.2.2.1). The experiments carried out in this thesis usually require about 10^6 to 10^7 repetitions to show interpretable results.

[20] A contrast of 40 % is theoretically possible [Chi07].

4 Confocal microscopy of NV centers

As it is our aim to observe quantum systems characterized by their emittance of light, the obvious choice of measurement is light microscopy. Further, it is aspired to read out single NVs which are naturally close to the surface, but scattered throughout the diamond's volume. To be able to focus on a single NV one needs a detection mechanism which can adjust the position of the focal spot in all three dimensions with high resolution. Conventional microscopes deliver an image superimposing the sharp picture from the focused plane and blurred, out-of-focus images. In contrast, confocal microscopy meets these requirements, as it collects light exclusively from the focal plane. The main disadvantage of the confocal microscope is the observation of just one single point at a time. Therefore the creation of images requires more time compared to wide-field microscopes. Fortunately NVs are trapped in the diamond's crystal lattice and don't move.

4.1 Confocal microscopy

A confocal microscope can produce a fully three-dimensional image of the object observed with it's resolution only restricted by diffraction.

In a confocal microscope the illuminating light is focused into the sample through the objective, and the scattered light is then collected by the same objective, to be projected onto a pinhole aperture. To avoid collecting light which comes directly from the illumination source, a beam splitter is used between objective and pinhole. Behind the pinhole a detector is mounted, counting incoming photons. This means that information which is not originating from the (con)focal plane is suppressed twice. The intensity of illuminating light and therefore scattered light decreases quickly anywhere outside the focal spot. Further, any light from a source outside the focal plane is not projected onto the pinhole aperture, but in front or beneath it instead. On that aperture's plane light from such a spot will appear as a disk from which most light will be blocked.

The resolution of a microscope is limited by diffraction. The resolution is defined as the smallest distance between two equally bright point-like light sources that can be discerned. According to the Rayleigh criterion, discernibility has been reached when the brightest spots have a distance greater than the radius of the first minimum[1]. An Airy disk is the central spot, the circular area inside the first minimum of the diffrac-

[1] One different definition of discernible light sources is, that the maxima of zero order of the corresponding Airy disks do not overlap [uni12]. This means the intensity would drop to zero between the spots, whereas it would drop to $8/\pi^2$ in case of the Rayleigh criterion, which is about 81%.

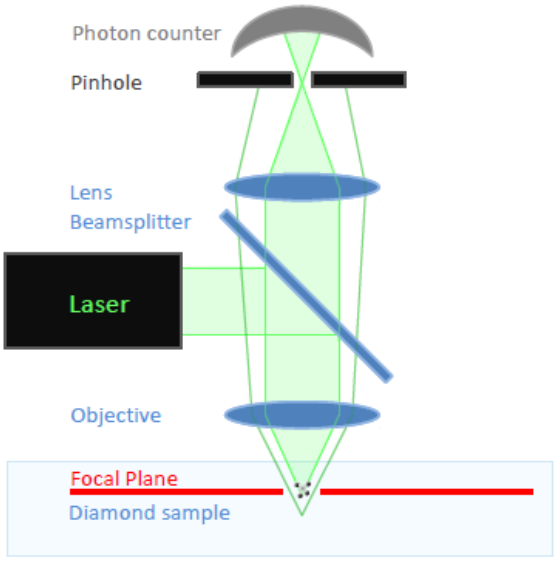

Figure 4.1: Scheme of the confocal microscope. Light beams from the confocal plane are indicated in light green. Light beams originating from sites off the focal plane – indicated dark green – generally won't pass the pinhole and therefore are not imaged by the microscope.

tion pattern created by light passing through a circular aperture. The radial intensity distribution can be calculated via Fraunhofer diffraction and is:

$$I(r) = I_0 \left(\frac{2J_1(x)}{x} \right)^2 \tag{4.1}$$

$$x = ka \sin(\theta), \tag{4.2}$$

where I_0 is the intensity at the center, J_1 the Bessel function of first order, k the wave number, a the radius of the aperture and θ the opening angle. As the first minimum of the J_1 is found at 3.8317, the Rayleigh criterion for the angular resolution (2θ) can be derived:

$$\sin(\theta) = 1.22\lambda/D, \tag{4.3}$$

with $D = 2a$ being the diameter of the aperture. Within that area, 86% of all light is concentrated. The FWHM diameter is found at $1.028\lambda/D$.

Optical errors are not fully described by the diffraction of a single blend. It can be observed that the full point spread function has a more complex pattern. One needs to consider the point spread function of the focal spot, which is in addition not a spot but a inhomogeneously lit area. That product of point spread functions lends further complexity to the pattern but reduces the FWHM, effectively enhancing the resolution by

about 30% (in case the pinhole is exactly the diameter of the Airy disk). The resolution d of a confocal microscope is ideally approximated as [Web96]:

$$d \approx 0.4\lambda/NA. \tag{4.4}$$

The numerical aperture NA is a quantity for describing the range of angles over which the optical system can collect light[2]. For objectives this explicitly depends on the refractive index of the medium between the optical instrument and the sample and on the half of the opening angle.

4.2 Experimental Setup

4.2.1 Illumination path

Illumination is provided by a frequency-doubled, diode-pumped laser. A laser provides a continuous wave of 450 mW, which makes it a class IV laser. It radiates a green 532 ± 1 nm Gaussian beam of approximately 2 mm diameter and approximately 99% linear polarization.

The fluorescence of NVs can be excited off-resonantly. This is possible because the phonon-sideband contributes a large portion to the absorption spectrum. Therefore illumination can be performed with frequencies above the ZPL, which allows observation of the fluorescent light almost exclusively, while any scattered light from illumination can be filtered out.

Power stability of the laser is maintained by a feedback loop. An AOM is positioned in the coincident focal spots of two positive converging lenses (focal length f=300 mm). The AOM driver includes a radio frequency which functions best in its linear regime. In this operating range, about 50% of the laser intensity is diffracted into the first order of the AOM. Behind it, a beam sampler (a 1 mm thickness microscope slide) guides a small portion of the light onto a photo diode to measure the power. Its signal is fed into a proportional integral derivative (PID) controller[3].

For several experiments, time dependent illumination – especially laser pulses of precise duration – is necessary. Therefore a second, fast AOM may interrupt the laser beam.

[2] The numerical aperture is defined as [Dem08]: $NA = n \sin(\theta)$

[3] This device attempts to readjust the power by tuning the AOM in three ways. The proportional control creates a correction signal proportional to the present error. Therefore, the error decreases until only a steady-state error is left. This error occurs, because if no error is present no correction signal will be created for compensating the successive drift. Adding a correction signal proportional to an integral over past errors compensates that disadvantage, but results in an overshoot. This creates an oscillating signal, which can be damped if the gain of the controller is small enough; otherwise, the signal will diverge. To compensate for that overshoot, a derivative control, an estimation of the future error by time derivation of the present error, is added. That way, the stability of the laser increases significantly. Stefan Putz measured a drop of the relative standard deviation from 2.2% to 0.46%.

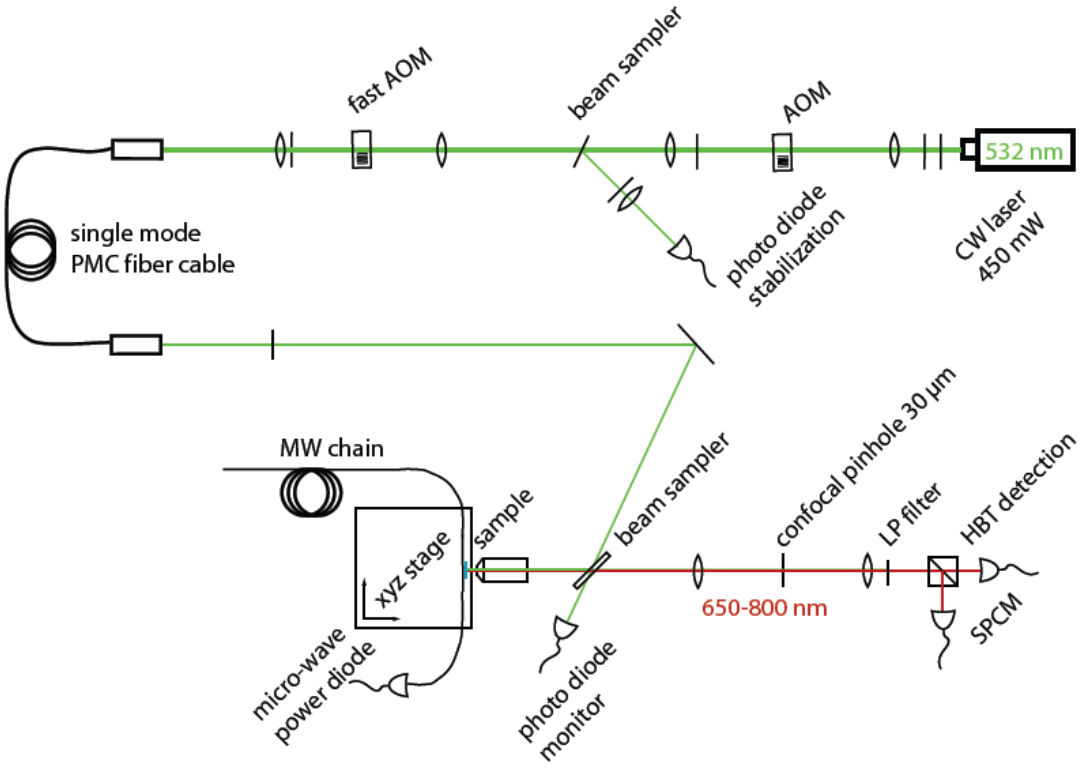

Figure 4.2: Sketch of the illumination path.

It is possible to switch on from 0 % to 90 % intensity within about 18 ns. This AOM is positioned in the focal spot of two 100 mm converging lenses, which form an afocal system. An afocal system leaves incoming rays, which are parallel to the optical axis, parallel. Around 70 % of the laser power is diffracted into the first order of the AOM. To restrain the outbound laser beam to that first order of diffraction, an iris diaphragm blocks all other rays.

Coupling into the polarization-maintaining single-mode glass fiber does not only separate the area of laser preparation from the very light-sensitive measurement area, but also cleans up the mode profile. Only the Gaussian light beam of lowest order is able to pass through. Behind the collimator is one further half-wave plate to control polarization of the light.

The beam is then directed onto a beam sampler reflecting a portion of the illumination light onto the sample. The photons scattered by the NVs return along the same route; therefore, the reflectivity of the beam sampler has to be low, as otherwise, most of the already weak scattering light beam would get reflected back into the light source instead of the photon detector. On the uncoated optical surface of the beam sampler, incoming

green light undergoes Fresnel reflection, which depends on the angle of incidence and polarization, and reflects 1-10 % of the intensity in the sample's direction. The rest is collected by a photo diode for monitoring the excitation intensity.

As it is desirable to collect as much of the NV's fluorescence signal as possible, an oil immersion objective (Olympus PLAPON 60XO) with a large numerical aperture of 1.42 is used. The immersion oil reduces the reflection and the angle of refraction off the optical axis on the diamond's surface, because the oil has a much higher refractive index (n=1.5) than air (n=1). This increases the number of rays entering the objective lens, which means a higher NA, resulting in a higher optical resolution. As light focused onto as well as emitted from the focal spot is affected by the point spread function, one will observe a convolution of both in the final image of the confocal microscope.

4.2.2 Translation stage

As it is rather difficult to move the beam axis and focal depth of such a confocal microscope over a sample, it is advisable to move the sample using a piezoelectric stage. This stage, a Melles Griot 17MAX301, is mechanically shifted using coarse and fine micrometer screws, and its piezoelectric device has a closed-loop accuracy of 5 nm and a range of 20 microns in all three directions. The stage carries a tightly fixed, but easily removable construction, which resembles a horizontal mounting for microscope slides, but instead may contain the sample holders.

An NV can be tracked by frequently scanning the area around the NV to determine the current position of the maximum intensity. The stage thereby attempts to always keep the NV at the focal spot of the microscope.

The immersion oil creates a small drag on all samples that are just fixed by a covering wire onto the sample holder. This creates characteristic distortions on the samples' images, usually tilted elongations of spots like NVs, but easily lets one discern immersion oil from diamond or glass, as one will observe many bright thin horizontal lines in the oil, which are emitted from dust particles and impurities; these will most likely not remain in the same location until the next line is scanned.

4.2.3 Microwave chain

For conducting experiments involving spin-manipulation, it is necessary to supply the sample with a microwave signal, typically on the order of 2.87 GHz. The microwave chain consists of the following devices:

- The microwave is provided by a signal generator (ANRITSU MG3691B), which operates in a range from 2 GHz to 10 GHz tunable in 0.01 Hz steps. The manufacturer states the accuracy to be the same as the 10 MHz time base, which gets

slightly broader in sweep mode. Frequency changes can be made quickly, typically 5 ms/GHz when no band switches are being crossed. It has a maximum output power of 30 dBm (1 Watt), but the regular operating range is up to 20 dBm. Usually at least a 10 dBm attenuator is attached directly to the generator to prevent damage to the following devices due to high power. For many experiments, attenuators of up to 50 dBm were utilized, as the micro-structures constructed do not need or even withstand such high power.

- For producing short pulses for spin manipulation, a fast microwave switch controlled by a pulse generator (Spincore PulseBlasterESR-PRO-II) is used. The pulse resolution achieved is 2.5 ns.
- Finally the signal is amplified by a Minicircuits ZHL-16W-43+ amplifier by a gain of 45 dB $\hat{=}$ 16 Watt, which is then transported to the sample.

Table 4.2.3 gives the MW losses and gains caused by the components between the microwave generator and the sample holder and was carried out by Stefan Putz [Put11]:

component	loss/gain in dB
attenuator	-10 (or more)
MW cable	-1
switch (+cables)	-3
amplifier	+45
MW cable	-1
Σ	30

From the coaxial cables, SMA connectors pass the signal to a co-planar wave guide (CPW) on the sample holder. The construction aims to transport the signal to the sample with as little loss as possible. Unfortunately, there are no measurements available characterizing the loss/gain of the CPW on the sample holder with the micro-structure on the diamond sample connected to it. One may assume that the micro-structure on the diamond will cause the component to almost completely reflect the signal, because it forms a short circuit. This means it has a very low impedance Z_L, compared to the coaxial cable and CPW, which have $Z_0 = 50\,\Omega$. As a result, the microwave is almost completely reflected at the shortcut on the diamond sample; therefore, reflectivity $r \approx 1$, since reflectivity is expressed as

$$r = \frac{Z_L - Z_0}{Z_L + Z_0}. \tag{4.5}$$

The diamond sample is positioned in the middle of the sample holder and thus completely interrupts the center line of the CPW. Therefore, the signal would be largely reflected at the cut line, delivering a very small and misshapen signal to the sample. A thin wire soldered to both sides of the center line bridges the electromagnetic signal and provides a strong microwave signal all throughout the sample. Additionally the wire functions as

fixation of the sample to the CPW[4]. The experiment was changed to utilize a short circuit directly on the diamond's surface, so instead of a wire, bonds transport the microwave onto the diamond.

4.2.4 Sample holder

Sample holders are $80 \times 25 \times 1.52\,\text{mm}$ boards with a milling in the center. Usually, sample holders for single NV diamond samples have a 2.2 mm square milling with 0.4 mm depth, whereas the ensemble NV diamond samples are positioned in sample holders with a 4.7 mm square milling, which is 0.9 mm in depth. For some samples the milling is turned around by 45° to allow a larger length of the edges to be accessible for bonding. Below the milling there is a 1-2 mm-wide drilled hole to ensure that no illumination light traversing the sample is scattered back into the objective by the sample holder, which would inadvertently contribute to the signal detected.

Another function of the board is conducting microwaves from coaxial cables to the sample. To achieve this, the board is constructed as co-planar wave guide (CPW). The core is a 1.48 mm Rogers RO4400 (a glass-fiber reinforced hydrocarbon/ceramic zaminate) board, which is an insulator with a dielectric constant of $\epsilon \approx 3.54$ [PP12]). On top and on the bottom it is coated with a copper layer of 0.02 mm thickness. The center conductor is 1.7 mm wide and the gaps between center conductor and ground conductor are 0.25 mm wide. Both ground conductor plates on the top are connected to the ground conductor plate on the bottom with rows of vias. These are vertical electrical connections between different layers of conductors[5]. This configuration results in a $50\,\Omega$ impedance, calculated using the RF (radio frequency) design software AppCad [Ava02][6]. The gaps are widened at the ends of the boards where the SMA connectors are soldered to the CPW.

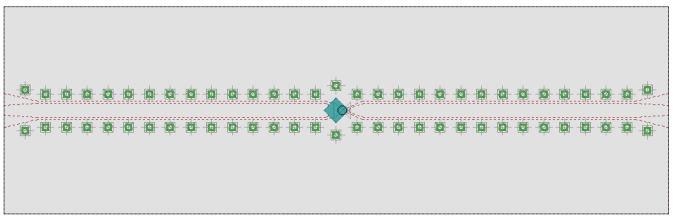

Figure 4.3: Sketch of the sample holder board created using Eagle. The dotted red lines indicate the borders of the CPW metal plates on the top; the vias are marked green, the milling is coloured in teal and the hole beneath the area of the sample observed is marked by a black circle.

The milling for the diamond sample completely interrupts the center conductor. To allow

[4] In many cases the wire is to loose to hold the sample in place; therefore, sometimes is additionally glued to the sample holder.

[5] Vias are often referred to as through-holes, although conventional through-holes do not necessary connect layers of electric conductors but one conductor layer and electronic devices such as resistors.

[6] http://www.hp.woodshot.com/

the microwave to traverse that site, a rectangular golden wire of 30 µm is extended from the ends of the center conductor over the diamond sample. This wire also serves to affix the sample in some cases; in other cases, it has been attached using glue. In the course of the thesis project, this wire was replaced by an electronic micro-structure upon the diamond surface. Then, instead of that wire, bonding wires connect the CPW conductors to the electronic structure on the sample and attachment is exclusively provided by gluing the sample to the sample holder.

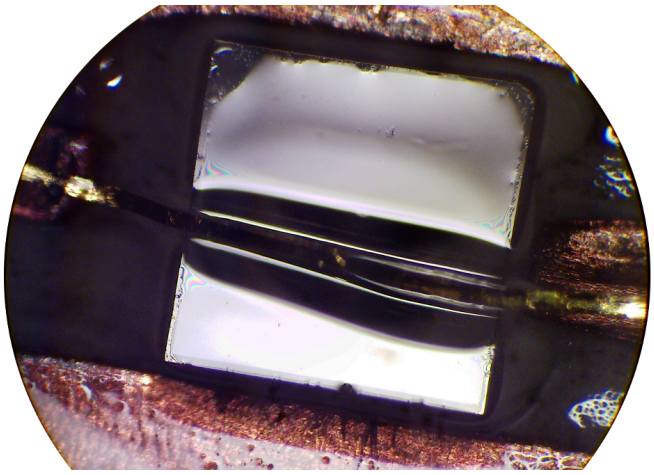

Figure 4.4: This picture shows a magnification of a diamond sample inserted into the milling on a sample holder held in place by a gold wire with a rectangular cross section. The liquid upon the sample and the CPW is immersion oil, which causes the rainbow-colored interference patterns and dark "shadows" due to adhesion.

4.2.5 Detection path

The fluorescence and, unfortunately, stray light returning from the objective pass through the beam sampler once again. That beam is corrected for infinity, so one needs a tube lens to recreate an image again. With a focal length of $f = 100\,\mathrm{mm}$ an magnification factor of $M = 33$ is achieved. That image features an Airy disk of about 15 µm in diameter. A pinhole of 30 µm in diameter is installed in the focal plane. It prohibits light originating from locations off the focal plane of the objective from entering the detection area. The pinhole is twice the size of the Airy disk, reducing the resolution, but allows for higher transmitted intensity, which enhances the signal-to-noise ratio [Put11].

After the pinhole the light needs to be focused onto the detectors. Placing a convex lens two times the focal length away from the image recreates it on the other side at the very same distance. This is done here using another achromatic lens of $f = 100\,\mathrm{mm}$.

A long-pass filter, which blocks light below 650 nm, prohibits detection of illumination light. Fluorescence light from the NVs' ZPL with 637 nm still cannot pass, but a considerable amount of the fluorescence belong to the strong phonon side bands.

For measuring photon correlation functions, which is impossible with one detector due to the length of dead time, the beam is split. This is carried out by a non-polarizing 50:50 beam splitter. Such a detector arrangement is known as a Hanbury-Twiss detection scheme.

The actual measurement is provided by two single-photon counter modules (Perkin Elmer SPCM-AQRH-13). These basically consist of two highly sensitive avalanche photo-diodes. Care has to be taken, never to expose these diodes to ambient light while they are switched on, as their normal operating current is already very high (300 mA; maximum allowed current: 1.2 A [Per12]). The counter operates linearly in a range from 1 to 10^6 incident photons and saturates at about 29×10^6 c/s (counts). The detection signal is read out via a National Instruments counter card or, alternatively, by a time-tag card with 80 ps resolution, when time-resolved measurements are conducted.

4.2.6 Effective resolution

For our confocal microscope we use an objective with a numerical aperture of 1.42 in immersion oil. The objective is designed for use in immersion oil with a refractive index of 1.5 and loses its effectiveness in the medium of air. From that, one could calculate the diameter of the first Airy disk to be about 150 nm, once the the green illumination light determined the resolution.

But as the pin-hole is two times larger than the Airy disk imaged, the loss of resolution allows calculation as for for a wide field microscope. In that model the Rayleigh criteria [Car07][Dem08] is valid for calculating the minimal distance of two discernible points [Ame94][Dem08]:

$$r_{x,y}^{min} = \frac{0.61\lambda}{NA} = 0.23\mu m \quad , \quad r_z^{min} = \frac{2n\lambda}{NA^2} = 1.3\,\mu m. \tag{4.6}$$

In that formula NA is the numerical aperture of our objective, which is 1.42, λ is the wave-length of our laser, which is 532 nm and n is the refractive index of the medium, which is 2.4.

Aside from the resolution one can take a look at the first dark ring of the Airy pattern in order to characterize the optical properties. With the focal length f, the diameter d_{Airy} $= 2.44\ \lambda f/D \approx 1.22\ \lambda\,\mathrm{NA} = 0.46\,\mu\mathrm{m}$. The shape of the intensity distribution resembles a Gaussian distribution. A Gaussian distribution reaches $1/e^2$ of its maximum, which is also the definition waist radius ω_0 of a Gaussian beam, at about 33% of the dark ring of the corresponding Airy disk [FTGY08]: $2\omega_0 = 1.64\ \lambda f/D$. A focal spot defined that

way would measure about 0.31 µm in x,y-diameter in our case. The three dimensional excitation intensity distribution can be approximated as [Wol09]:

$$I(x, y, z) = I_0 e^{-2(x^2+y^2+(z/\kappa)^2)/\omega_0}, \tag{4.7}$$

with the eccentricity $\kappa = \frac{r_{x,y}^{min}}{r_z^{min}} = \frac{3.28n}{NA} \approx 5.6$ [Ame94]. An isosurface at $1/e^2$ of the maximum intensity confines the confocal volume to $V = 4\pi/3\ \kappa\omega_0^3$. Nevertheless, a different effective confocal volume is used in the literature [BKK+09]: $V_{eff} = \pi^{3/2}\kappa r_{x,y}^3 \approx 0.4\,\mu m^3$. Experiments on our single-NV diamond samples resulted in measurements from which a 2 µm confocal volume was calculated.

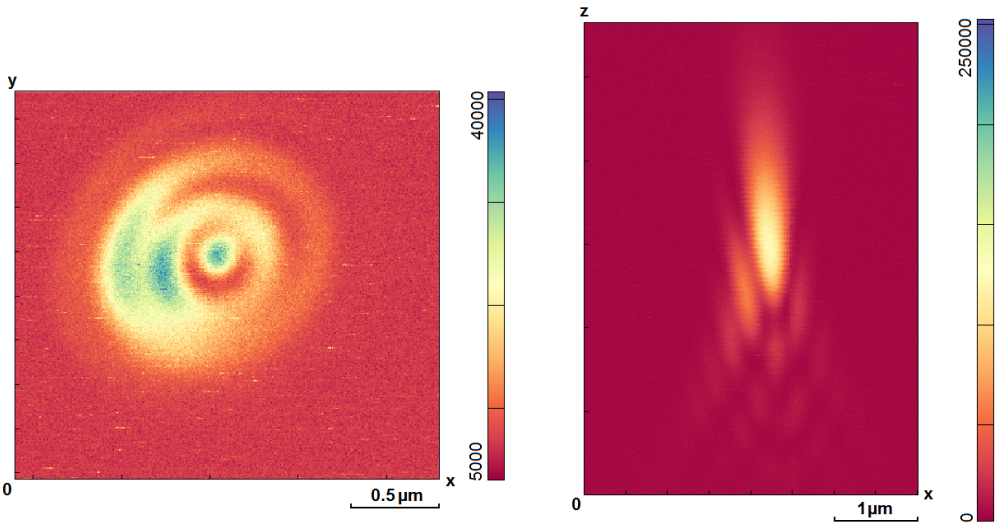

Figure 4.5: The images above show the diffraction pattern of a single NV center recorded using the confocal microscope. The picture to the left shows a scan of a plane through the center of the brightest spot perpendicular to the illumination beam direction. The picture to the right shows the scan of a plane along the beam direction.

4.3 Diamonds in use

There are three types of diamonds used: Bulk diamonds for NV ensemble studies and bulk diamonds for single NV studies and nano diamonds.

NV ensemble diamond samples The diamonds for NV ensemble studies are Type 1b samples, produced in a high-pressure, high-temperature (HPHT) process. They have a high nitrogen content, resulting in a yellow-brown tint, and were irradiated with neutrons and annealed (see 5.3.1) in order to achieve greater NV density. The final

samples have an NV concentration of about 8 ppm. The samples are quadratic prisms with spacial dimensions of $2.9 \times 2.9 \times 0.5$ mm. The roughness is likely to be greater than the manufacturer specified ($R_a < 5$ nm), due to aggressive chemical treatment during the cleaning. The surfaces are (100)[7] planes.

Single NV diamond samples The diamond samples for single NV studies are CVD-diamonds (chemical vapour composition) of type IIb, grown by Element 6. They are completely transparent and specified to contain less than 5 ppb single neutral nitrogen defects and less than 1 ppb boron impurities. As only 1-2% of the nitrogen participates in a NV one may expect less than 1 NV per μm^3. The sample is a quadratic prism with a size of $2.1 \times 2.1 \times 0.5$ mm. The specification sheet provides a surface roughness of R_a <5 nm. The surfaces are (100).

Nano-diamonds Nano-diamonds are either available as a suspension or as a powder of mono-crystalline grains of 0-0.05 µm diameter. In suspension of a high concentration they form a black liquid with a purple-brown tinge, probably due to the presence of nitrogen impurities, NVs and graphite. The suspension we used was basically diamonds in water and was diluted in a series to concentrations allowing observation of single crystals. A proper concentration was reached at 1000 ml^{-1}. A drop of the dispersion was applied onto a 170 µm -thick cover glass, where it had to dry for several hours under air circulation provided by a clean-room work bench. It was then affixed to a microscope slide with the diamond-coated side facing it. A gap between slide and cover was created using glue drops to maintain a high contrast in the confocal microscope image when approaching the surface.

Bulk diamonds with high NV densities

With bulk diamonds one has to deal with a high concentration of NVs and therefore a fluorescence intensity many orders of magnitude higher than in case of single NV observations occurs. Filters of 10^7 extinction were installed to protect the APDs (avalanche photo diode) in the detector. The intensity I increases proportionally with the illumination intensity I_0, the effective confocal volume V_{eff} and the NV concentration c. A unit conversion factor K relates the 1 ppm with 175830 NVs/μm^3 concentration (see 3.2.3.2). Additionally the back-scattering intensity I_{back} also contributes to the intensity:

$$c \approx \frac{I(x,y) - I_{back}}{I_0 V_{eff} K}. \tag{4.8}$$

[7] miller index notation

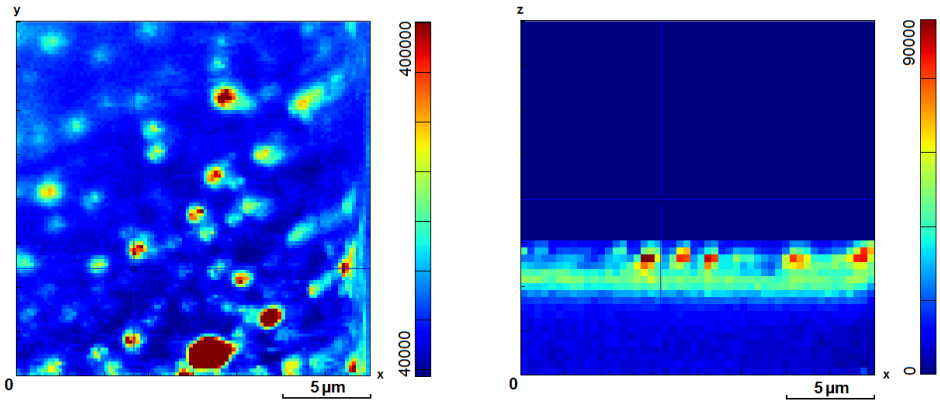

Figure 4.6: This image shows nano-diamonds on the surface of a glass cover slide in a dilution allowing the observation of single nano-diamonds. The diamonds were applied onto the back side of a glass cover slide what was glued to a microscope slide with an air gap in between to reduce the backscattering of illumination light.

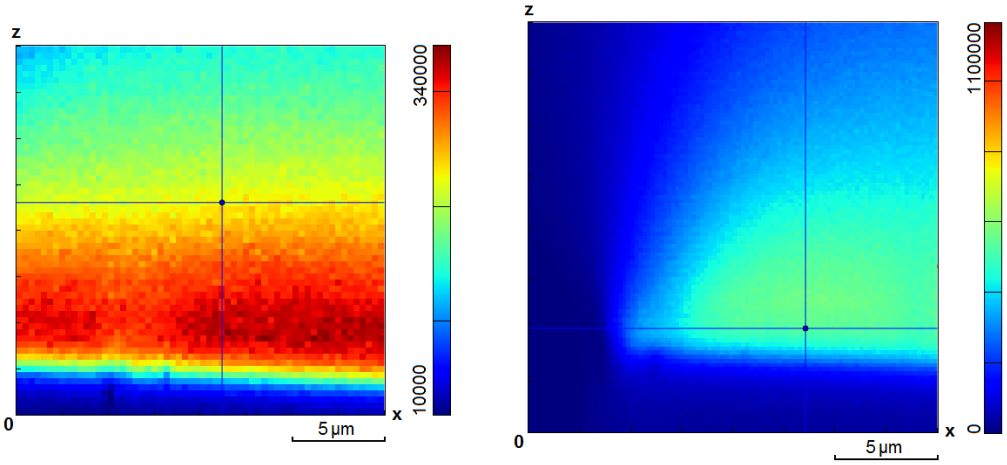

Figure 4.7: The images show confocal scans of an ensemble NV diamond sample. The vertical axis of the diagram is perpendicular to the sample surface. Both images show a cross section of the sample surface along the lower edge. The image to the left shows the sample on an unobstructed area, whereas the picture to the right shows the left edge of a thin metal layer reflecting light.

5 Design and fabrication of microwave micro-structures

5.1 Design considerations

The spin state of an NV can be initialized and read out by off-resonant fluorescence excitation (see section 3.3). Spin 0 states are initialized by driving fluorescence cycles induced by the same optical means as the state readout. Thus, readout inevitably destroys the state as it resets it to spin 0 at the same time. Arbitrary operations on spin states cannot be performed by optical means. Instead, the qubit is controlled coherently by resonantly driving the spin transition in the microwave (MW) range. Since a spin is a magnetic dipole moment, we couple it to the magnetic component of the MW field. To achieve an arbitrary change of the qubit state the duration of the MW irradiation has to be chosen to be a portion of the Rabi period of the spin, where a full period equals a 360° rotation on the Bloch sphere around an axis orthogonal to the z-axis. Resonant driving is achieved when the frequency of the MW irradiation matches the Larmor frequency of the spin, which corresponds to the energy difference between the $m_s = 0$ and $m_s = \pm 1$ of the ground state of an NV, which is about 2.88 GHz. Such microwaves are in the regime of a few centimeters wavelength.

5.1.1 Minimizing focus to antenna distance using micro structures

In order to enhance the application of microwaves to the NV it is necessary to know the geometric shape of the magnetic field distribution created by the microwaves traversing the diamond sample. The field is of special interest in the plane of the diamond surface in the gaps between the ground conductors of the sample holder and the metal conductor on the diamond surface. In principle, the field in the gap between the wire and one ground plane resembles the field between two straight wires with inverse currents. In this respect there is quite a similar field in the gaps of a co-planar wave guide. However, there are some geometric details that prohibit an accurate estimation of the field geometry. In contrast to a co-planar wave guide, which features a plane where all magnetic field vectors are orthogonal to that plane, it would be beneficial to have that plane match the diamond surface. This is prohibited in the case of the wire set-up, as the wire is located much higher than the ground conductor. On the transition from CPW to the wire, the gap also increases by a factor of 2 to 5, depending on the sample holder, which creates edges on the ground conductor in the direction of wave progression. In the microwave regime these edges are capacitances that distort the electrical field (see figure 5.3). As

this is a dynamic field this affects the wave form in general. At the same location the current becomes constricted, which changes the shape of the source of the magnetic field. Further, the wire's position is quite arbitrary and changes with each insertion of the diamond into the sample holder.

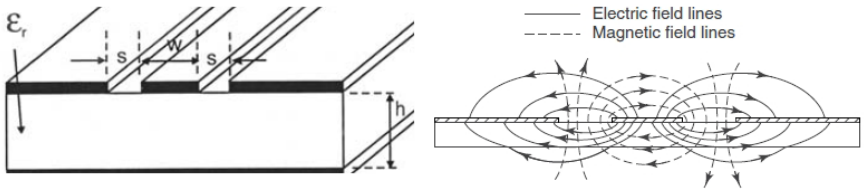

Figure 5.1: A sketch of a CPW with the relevant dimensioning to the left and cross section of the CPW showing the field lines of the magnetic field to the right.

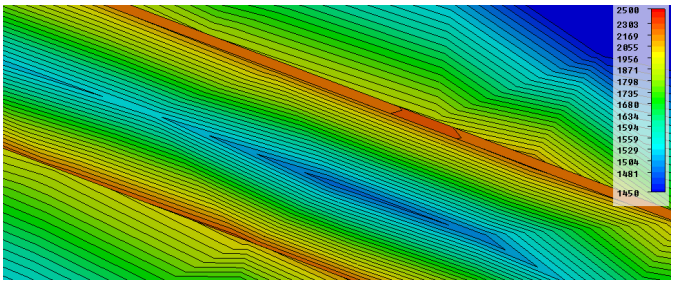

Figure 5.2: Finite element simulation of the magnetic field strength in z-direction in a gap of a CPW. This CPW has a gap width of 10 µm , 40 µm center conductor width, 1 µm height and mounted on top of a diamond. The excitation of the system was simulated with a 3 GHz microwave of 1 W energy. This results in a magnetic field strength of a few kA/m.

Another important issue is that one cannot observe NVs in close vicinity to the wire, where the highest magnetic field strength is to be expected. This is due to the great angle in which the objective is able to collect photons[1]. This means the rays reaching the focal spot with an angle of 18.8° are already reduced by a factor $1/e$ in intensity compared to the central beam. If the wire rises 0.1 mm above the diamond surface, the nearest point to the wire on the surface fully suited for observation is 313 µm from the center of the wire. Unfortunately, the wire never lies flat on the diamond surface, so generally a greater distance has to be expected.

[1] With NA=1.42 and n=1.5 the opening angle becomes $\alpha = 71.2°$.

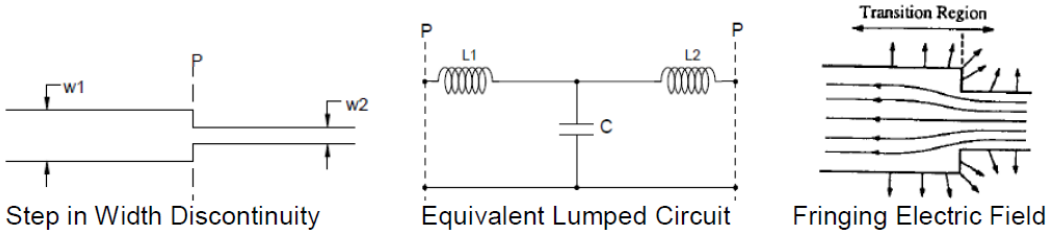

Figure 5.3: The transition from the CPW center conductor to the wire can be compared to a change in the width of a strip line. The confinement of the current to a smaller cross section changes the impedance, and the edges facing in the direction of wave propagation act as a capacitance.

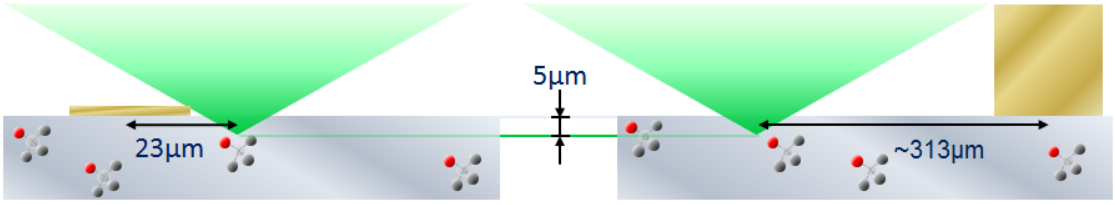

Figure 5.4: The image shows a cross section of the loop of the micro-structure to the left and the wire to the right. The cone including all rays of light that can be emitted/collected (which is the case if geometric optics are assumed, there being no sharp borders when diffraction is considered) by the objective is highlighted in green. An observed spot of five µm beneath the diamond surface is assumed, because most NV centers are usually found at this depth. The resulting distance of the closest observable spot to the center of the current density is 15 times higher for the wire set-up than for the micro-structure.

It is the aim of that thesis to overcome some of the above disadvantages by constructing an electronic structure attached to the diamond sample. It needs to be especially flat in order to minimize the minimum distance of NVs to the metal structure at which they can be observed. Such a device is best created in the form of a structure of thin metallic plating applied by the means familiar from semiconductor device manufacturing. In contrast to the set-up using a wire, such a device can not slip out of place as regards the position of the NVs.

The two basic methods for creating the structure in the metal layer, lift-off technique and etching, both in combination with photo-lithography will be described in section 5.3. These techniques easily allow geometric structures of several µm precision; hence, the shape of the magnetic field can be estimated with considerable accuracy even in close vicinity its source. Aiming for a metal layer of about 1 µm thickness allows for a

minimum focal spot distance[2] from the structure of about 20 µm to the wire.

5.1.2 Planar MW structures for maximum magnetic field strength

For maximizing the current locally it was decided to design the structure as a short circuit of the CPW. The impedance of a wave guide is usually expressed as

$$Z_l = \sqrt{\frac{R + j\omega L}{G + j\omega C}}, \tag{5.1}$$

with R being the resistance in the direction along the guide, G being the resistance of the insulator between center and ground conductor, L the inductance and C the capacitance, all per unit length of the guide. In the presence of a large amount of leakage the impedance approaches zero. The reflection coefficient at a boundary between two impedances Z_1 and Z_2 is expressed as:

$$\Gamma_{12} = \frac{Z_2 - Z_1}{Z_1 + Z_2}, \tag{5.2}$$

thus it approaches -1 for a short circuit ($Z_2 = 0$). This means that the voltage signal picks up a 180° phase shift, while the current stays in phase. Therefore, one finds double the inbound current inside the circuit. Unfortunately, it is quite difficult to estimate the power effectively transferred to the short circuit, as it is impossible to measure the reflections caused by unwanted but inevitable changes of impedance between the CPW junction and the short-circuit.

In order to minimize the reflected MW in front the short circuit, it is desirable to maintain the impedance constant virtually up to the short circuit. Fortunately, all structures with an impedance other than 50 Ω are very small compared to the wavelength, so they will not contribute much to the scattering of the wave (3 cm of wavelength vs. several millimeters of the diamond and connection set-up). To create a link between CPW and the short circuit which is smaller than the center conductor by a factor of 50, the CPW was tapered towards the short circuit. As all three conductors of the CPW are intended to extend onto the diamond, space for the connectors between sample and sample holder needs to be considered.

A straight short circuit between the ground an center conductors offers a very small area (see section 5.2.2) with sufficient field strength for magnetic resonance experiments. This is due to high gradient of the magnetic flux density and the relatively small length of the short.

Due to the low resistance of the metal band constituting the short circuit and the excellent heat conductivity of diamond (see section 3.1.2.1) the short circuit can be elongated to form a loop. Therefore one obtains a large circular area (see section 5.2.3)

[2] taking into account that we experienced NVs to occur only 5 µm or deeper beneath the surface

affected by the magnetic field. It is especially beneficial that the field of a loop does not drop to zero on the inside of the loop.

On the outside a ground plane surrounding the loop ensures an equal phase of the MW on both sides of the ground conductor. Simulations show no significant effect on the internal magnetic field if a circumventing ground plane is present (see figures 5.13, 5.15). The decay of the field strength on the outside becomes less severe when a ground plane surrounds the loop, because it provides a counter current regarding the loop. One can imagine the magnetic field lines shifted from an infinitely expanded volume into the gap. Basically, the field inside the gap behaves like that of a CPW gap, but gets distorted asymmetrically by the curvature. Nevertheless, the construction prohibits the field from behaving in similar fashion at every location. There is a spot on the ground conductor, where the phases of the waves travelling along the gaps cancel each other and the current induced by the loop out. Thus, no rotational symmetry is present; the influence of the ground conductor disappears at about the middle of the loop. The resulting area with sufficient field strength for NV experiments is so small, that by leaving only a small gap between ground conductor and loop, there appears to be no relevant waste of observation area on the sample surface.

5.1.3 Final design for the ensemble NV sample

The milling for the 3×3 mm diamond sample for ensemble-NV-observation is in the center of the sample holder with faces parallel to its sides. At the edge of the sample at which the microwave power enters, there are three large rectangular metallic plates. These are designed to accommodate the bond wires which connect the metal structure on the diamond sample with the CPW on the sample holder. Eight bonds connect the center conductors and six bonds connect the ground conductors on each side; the gap between center conductor and ground conductor is 200 µm the center conductor measures 800 µm at this location. These dimensions were chosen, as they result in about 50 Ω [3] impedance. The conductor plates are then linearly tapered to form a final structure characterized by a 10 µm gap and a 40 µm center conductor width. The loop connecting the center conductor to the ground conductor as a short circuit has a 200 µm inner diameter and a width equal to the center conductor. The construction is depicted in figure 5.5. The ground conductor does not surround the loop. A distance of 100 µm was kept from each side of the sample for technical reasons[4].

[3] The desired impedance could not be accomplished, as the thickness of the gold plating could only be estimated inaccurately. Further, a unit conversion mistake when using AppCAD (by Avago technologies, 2002) causes further deviations from the desired impedance. As the structure is a tenth of the microwave wavelength the error does not contribute to the experimental results significantly.

[4] The photo resist used in the manufacturing process tends to form beads at the edge of the sample, which renders the photo-lithography process imprecise.

5.1.4 Reworking of the sample holder for single NV samples

In order to fabricate the bondings to the electrical conductors of the micro-structure one has to consider that the areas where the bonds are attached make up for the largest part of the micro-structure. This becomes a problem when attempting to connect a 2×2 mm sample to the CPW. Unfortunately, these were the largest diamonds of sufficient purity for single NV experiments at that time. If the milling for the sample is created in the conventional way, with edges parallel to the edges of the sample holder only, one edge will be usable for the areas where the bonds are attached. By turning the diamond sample 45°, two sides become available.

As the width of the center conductor, which will change into the short circuit at the end of the CPW, is 40 µm and the center conductor on the sample holder is 1.7 mm, the transition between these orders of size has to be carried out by continuous narrowing of the center conductor and the gap separating it from the ground conductor. This tapering is extended over both, the sample holder and the diamond surface. It starts on the sample holder at about 1.5 mm from the edge of the sample and ends at about the center of the diamond sample. The end of the opposing part of the center conductor is not considered in the design, as the microwave is expected to be reflected and not transit that part of the sample holder.

5.1.5 Final design for the single NV sample

The 2×2 mm CVD diamond samples used for single NV experiments will be inserted into the sample holder turned by 45°, due to reasons mentioned in section 5.1.4. The edge of the design is shifted 100 µm into the inside of the surface of the sample. The reason for this is the same technical issue as for the ensemble NV sample, but becomes a much more critical problem for the smaller sample. The design for 2×2 mm samples features a tapering that starts on the CPW and continues on the sample – the gap approximately in the middle of the edge of the sample, 734 µm from the edge of the center conductor, 261 µm edge for the gap and 800 µm for the ground conductor. This provides enough space for 12 bonds to the center conductor and 8 bonds for each ground conductor. The tapering was chosen to be as flat as possible to minimize the effect of corners, as corners equal capacitances in microwave electronics. The flat angle is also chosen to reduce the difference between the parallel and radial geometry that might influence the wave propagation. The final dimensions of the wave guide before the circular short circuit are 10 µm for the gap and 40 µm for the center conductor. The loop has an inner diameter of 500 µm . This design ensures an impedance of 50 Ω at least at both ends of the tapering[5]. As the center conductor and gap are quite fragile, the loop is positioned to have a safety distance from the sample edge of 300 µm . This is necessary as effects of

[5]The difference in permittivity of the underlying dielectric, the missing bottom ground conductor on the diamond sample and the differing metal layer thickness and conductivity make it impossible to preserve a constant impedance without creating a discontinuity in the gap width

the edge when manufacturing could severely damage the fragile short circuit and gap. The construction is depicted in figure 5.5. The design was manufactured with a closed ground conductor around the loop. Thereby, a larger area is available for attaching the metal layer to the diamond surface, which is preferable, because the degree of adhesion between gold and diamond is rather weak.

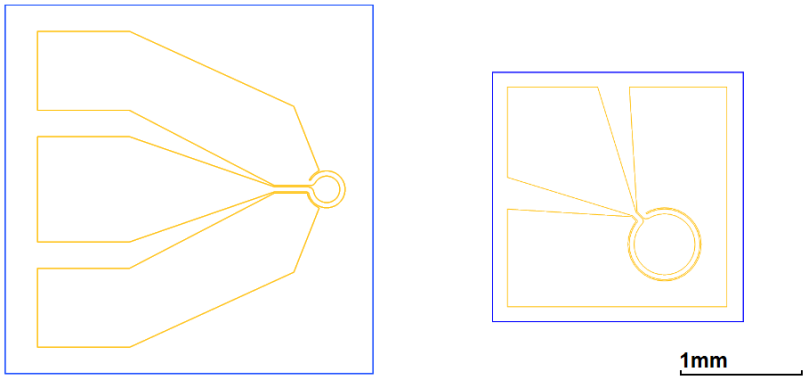

Figure 5.5: This picture shows the sketches for the micro-structures. Blue lines represent the borders of the diamond sample, golden lines represent the edges of the micro-structure. The sample on the left is a NV ensemble diamond sample and the right one a single NV diamond sample.

5.2 Finite-element simulations

All simulations of the micro-structures were carried out using Comsol 4.2a, a finite-element simulation program, which supports various physics calculations and allows for the use of combinations of them. The geometric models were created using Autodesk Inventor 2013, which accommodates easy changes to the dimensioning. Exporting these to the STEP-format, using surfaces only and a fine resolution, allows one to import the model into COMSOL without any compatibility issues.

5.2.1 Wire configuration

For simulation of the wire configuration of the experimental set-up, alternating current (AC) simulations with Ampere's law & current conservation applied onto the metal structure and Ampere's law elsewhere were performed. Radio frequency (RF) simulations, which were performed at lower precision, as they consume much more processing time, showed no significant differences. The skin effect, for example, has no influence on the magnetic field at distances relevant for the experiment, due to the geometry of

the set-up. Figure 5.6 shows a cross section of a quadratically shaped wire on top of a diamond surface.

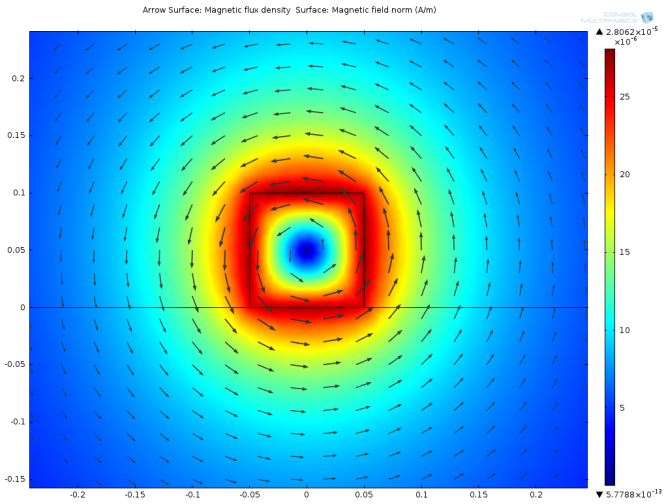

Figure 5.6: The magnetic field strength and direction around a current-carrying wire perpendicular to the drawn surface represented by color and arrows.

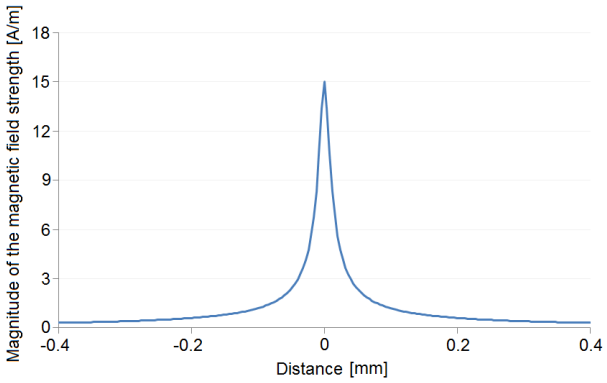

Figure 5.7: An 1D-plot illustrating the magnitude of the magnetic field strength along a straight line, which orthogonally crosses the wire 50 microns beneath it.

Figure 5.7 shows an illustration of the magnitude of the magnetic field strength along a straight line which horizontally crosses the wire at the center of the diamond sample and some µm beneath the diamond surface. A free straight wire would show a 1/x dependency for the the magnetic field strength as regards the distance from the source. For small distances to the wire the dependency deviates from 1/x, because the center of the wire is passed through by the line and the distributed current density does not cause a singularity of the magnetic field. For distances over 1 mm the edge of the ground

conductor noticeably influences the magnetic field strength, and it starts to increase again, when the edge of the ground conductor is approached. Unfortunately the NVs can only be detected 1 mm away from the center, resulting in a local field strength being only a 50th of the maximum field strength.

5.2.2 Straight short

This model for a micro-structure extends onto the co-planar wave guide on the diamond surface and is terminated by straight shorts connecting the center conductor with each ground conductor. It has to be noted that the width of the short has to be of a small size; otherwise, much sample surface area of reasonable field strength gets lost, as it is covered by metal. Another important question was to determine, how the distance of the shorts which are passed by electrical current in inverse directions affects the fields. Simulations show that the distance plays no significant role for distances on the order of the desired center conductor width, which was about 40 µm or above (see figures 5.9, 5.11). The fine meshing necessary in order to deal with the metal coating, which is of a factor 100 thinner than the other dimensions, turned out to be a major problem, but can be solved by selecting different meshing sizes for specific areas of the model.

Another interesting discovery was that the distance between the shorts does not play a significant role for the field strength.

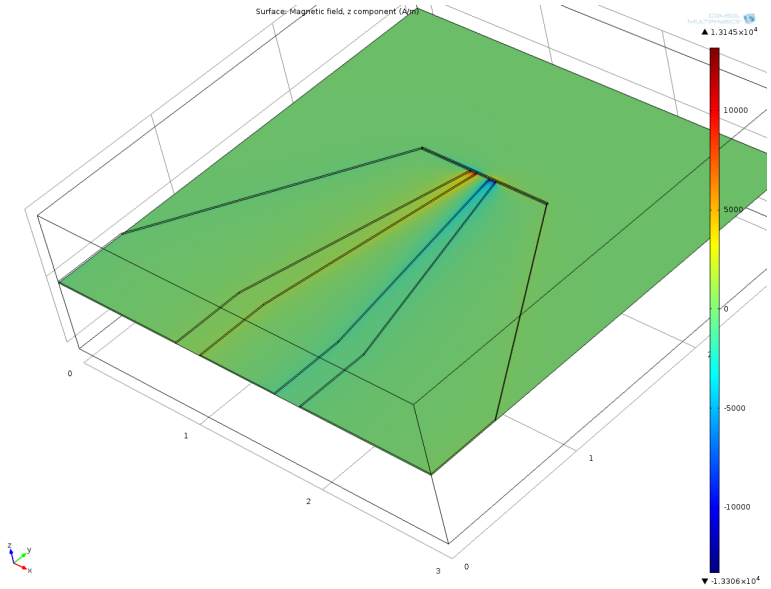

Figure 5.8: This is an exemplary view of a co-planar wave guide model with a straight short terminating it. The color plot depicts the magnetic field strength in z-direction.

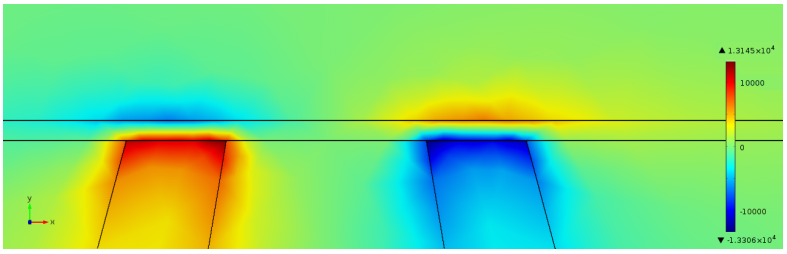

Figure 5.9: The detailed view of the shorts show, that the relevant area of observation is only about a few times the size of the area covered by the short itself.

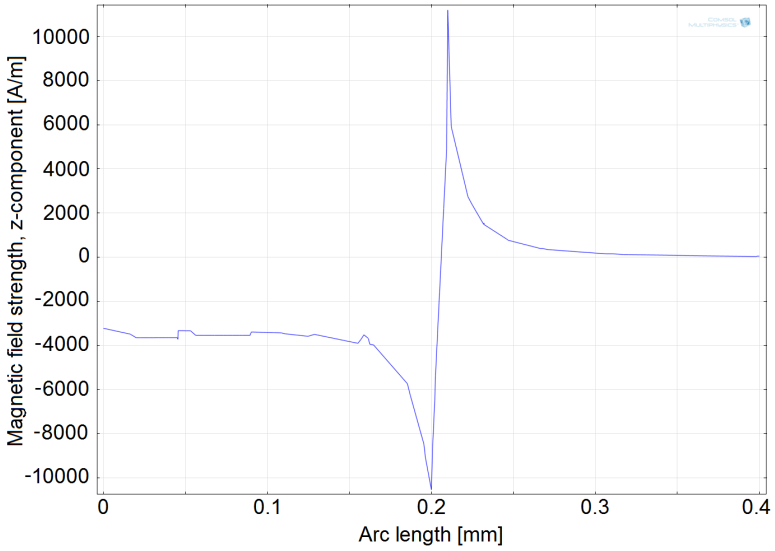

Figure 5.10: This 1D-plot was created from the magnetic field in z-direction along a line on the surface perpendicular to the short. The left side extends into the gap between center and ground conductor, whereas the right side into the uncovered space suitable for observation of NVs. The asymmetry results from the currents that mainly occur on the edges of the gap.

5.2.3 Looped short

The simulation of the micro-structure is performed on a model of a 200 µm loop on top of a 3×3 mm diamond sample. Figures 5.12, 5.13, 5.14 and 5.15 illustrate the results. This time, RF simulations were performed, as electromagnetic induction and skin effect influence the distribution of the current density inside the metal strip that forms the loop.

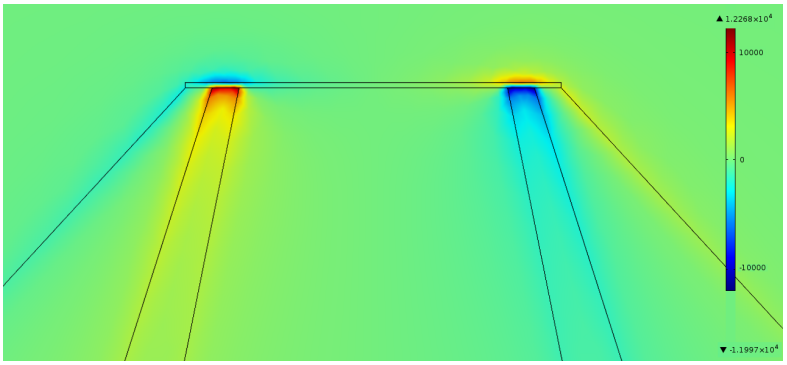

Figure 5.11: Increasing the distance between the shorts shows no significant increase of the magnetic field strength.

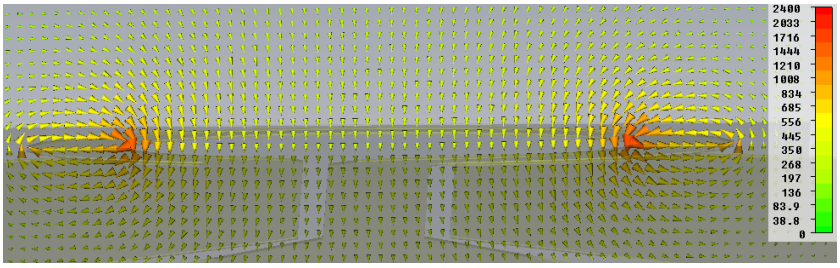

Figure 5.12: This 3D-plot shows the magnetic field direction as cones, the size and colour indicating its strength. The cross section cuts the loop through its center and is orthogonal to the CPW direction.

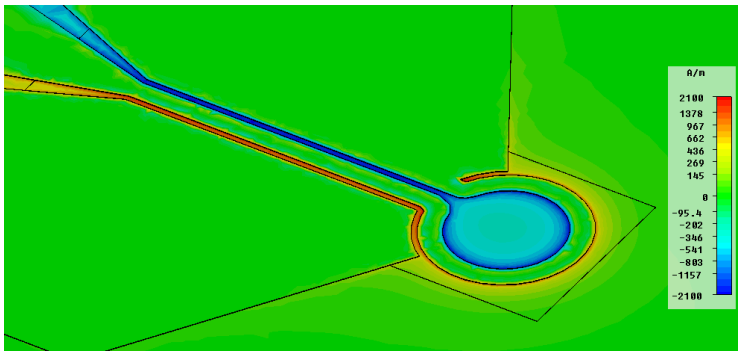

Figure 5.13: This 3D-surface-plot shows the z-component of the magnetic field according to the colours of the legend. The CPW gaps show inverse magnetic fields of high field strength. One can also see that the field at the inside of the loop decreases much more slowly than outside and has a lowest magnetic field strength greater than zero.

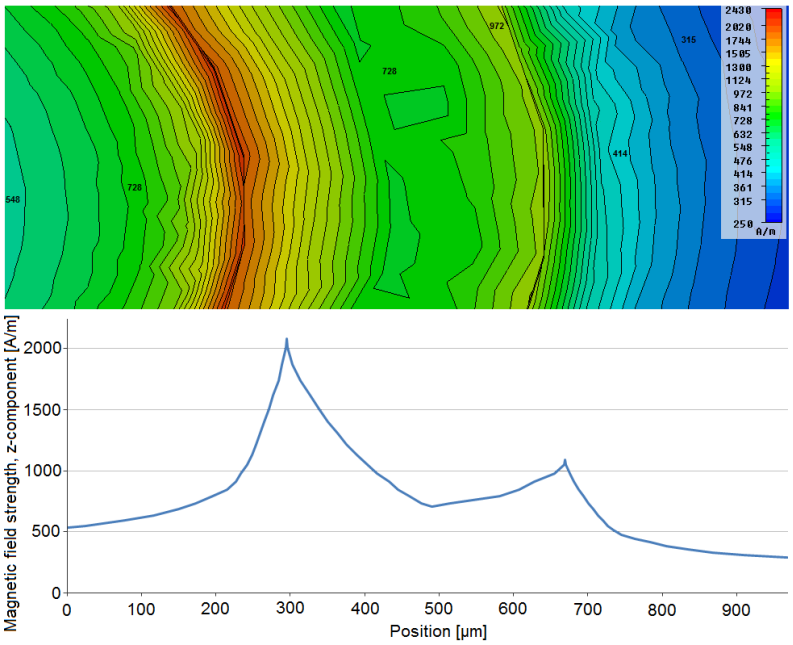

Figure 5.14: This 3D-plot shows the absolute value of the z-component of the magnetic field according to the colours of the legend. In the 1D plot below, the colours along the line crossing the loop are translated into numbers.

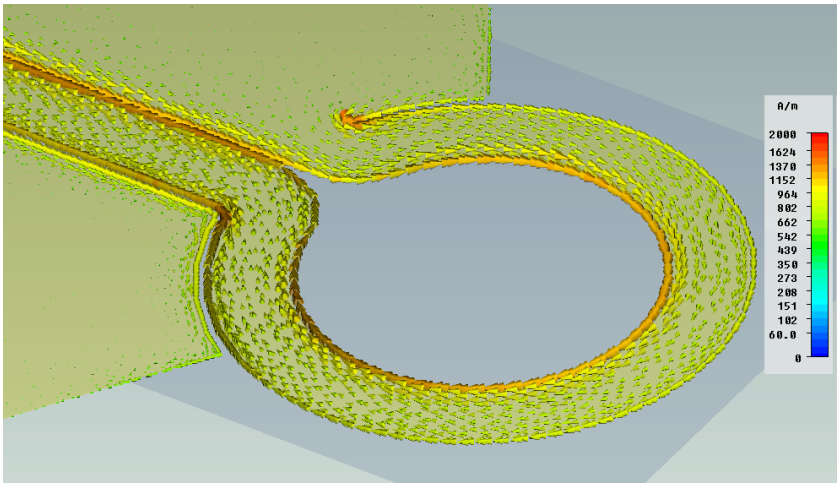

Figure 5.15: This 3D-plot shows the surface current density on the loop and the CPW. One can see that the currents stay mainly at the edges. The inner edge is preferred in areas where no current is present in the outer conductor (e.g. when the phases cancel each other out at the far end of the CPW or if there is no outer conductor at all).

5.2.4 Thermal simulations

An interesting question is, whether such a structure can withstand the thermal stress due to the high local currents. The simulations show that the heat is created primarily at the location of the smallest gap (see figure 5.16), but the high heat conductivity of diamond is able to transport it to the copper plates fast enough to prohibit the temperature from rising significantly (see figure 5.17).

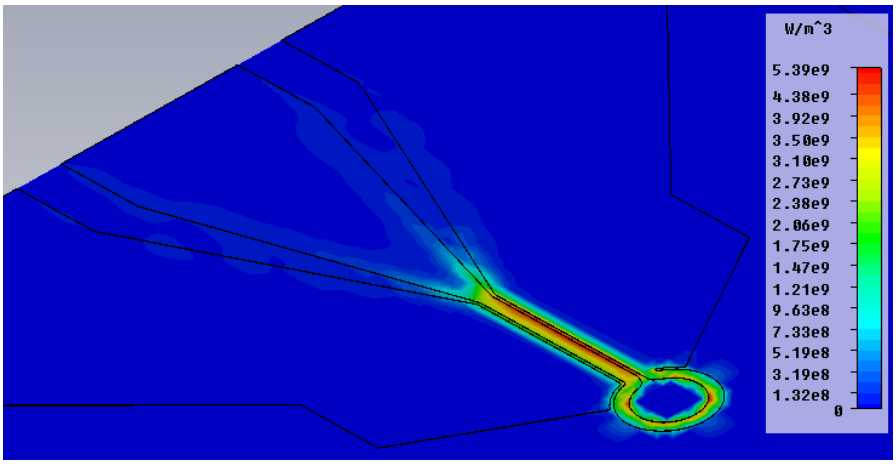

Figure 5.16: Heat generation caused by 1 W microwave power passing the microwave structure plotted at the surface of the diamond and micro-structure using a colour scale.

5.2.5 Conclusion

As it is desirable to have a maximally large area of high magnetic field density for observation of often sparsely distributed NVs, the decrease of field density is of great interest. As demonstrated based on the simulations conducted in the preceding sections, for different geometries, the magnetic field strength decay depends on the distance ρ from the axis of the system, with scales according to the following relations:

- Wire: $1/\rho$
- Straight short: $1/\rho^3$
- Circular short (outside, no ground conductor[6]): $1/\rho^3$
- Circular short (inside): $1/\rho$

[6] The stated dependency of the magnetic field strength regarding ρ is only valid if no ground conductor surrounds the structure. In case a ground conductor is present, the outer area is reduced to a gap which features characteristics of the CPW gap in some areas (see section 5.1.2), whereas the effect of the ground conductor vanish at elsewhere.

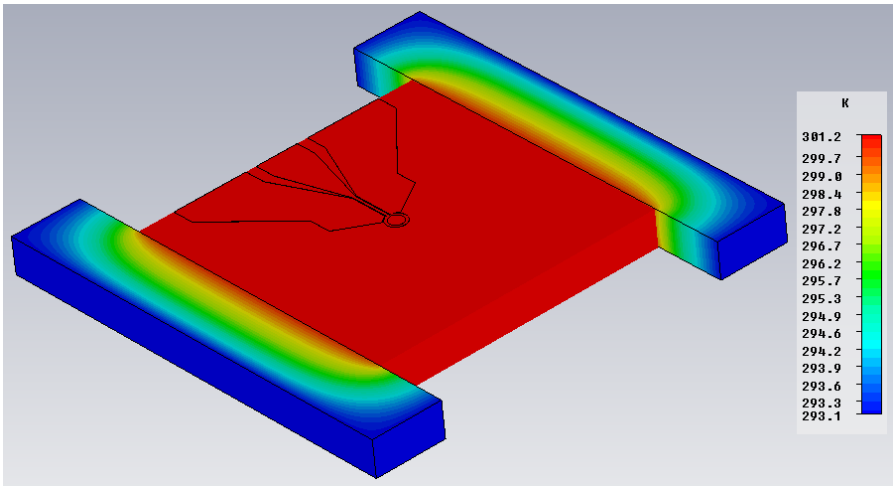

Figure 5.17: This plot shows the temperature of the diamond and micro-structure heated by the currents created from 1 W microwave power passing the micro-structure. The large bars on both sides of the diamond samples were defined to be made of copper and have a constant temperature at their borders, which is room temperature. Between the copper bars and the diamond sample a sheet of thermal grease was assumed to obtain more realistic circumstances. It seems as if the diamond almost completely shifts the heat gradient into the copper plate. Therefore the temperature of the diamond sample and micro-structure is almost homogeneously distributed and amounts to 8 K above room temperature.

The suitable area becomes more narrow the steeper the gradient of the field density. Therefore, only the wire and the inner area of the circular short circuit are usable from that point of view.

Another aspect worth mentioning is the area shielded from illumination by the metal components.

- The wire configuration shields the largest area because of its height. 0.1 mm-wide strips on each side of the wire are thus not fully illuminated.
- The shielded area next to a micro-structure is only 3 µm wide. In case of a straight short the CPW covers half of the suitable area.
- The loop configuration allows one to observe a the full face of a circle 6 µm smaller in diameter than the inner radius of the loop.

The advantage of the loop configuration is mitigated by the fact that one can run the wire system with higher microwave power input, such that the area providing a sufficient field expands outwards. Nevertheless, there are considerable benefits of a micro-structure,

most notably the fixed location of the stationary structure and the known field geometry. It is expected that this conjecture would allow one to observe the dependency of the Rabi frequency from the shape and direction of the electromagnetic field created by the loop. Further, it is anticipated that it was possible to identify NVs by their position as regards the micro-structure. This would permit one to find a particular NV again if, e.g., the sample was remounted.

5.3 Microfabrication

All microfabrication steps were carried out at the center for micro- and nanostructures (ZMNS) of TU Vienna, which is an excellently equipped clean room utilized for research and education, providing an optimal environment for creating microscopic devices. In addition to the equipment, they also generously provided us with their expertise, helpful hands, hints and calibrations. The work accomplished in this chapter was performed together with Matthias Stüwe, our workgroup's technician.

5.3.1 Sample preparation

5.3.1.1 Irradiation and annealing

To create a highly NV-enriched sample, one can use a Ib CVD diamond and try to create a large amount of vacancies. This can be achieved by irradiating the sample with particles that can pass the crystal lattice easily and only eventually collide with carbon atoms, which are tossed away from their position. Using neutrons for this task was an obvious choice at ATI, as the institute operates a nuclear research reactor of the TRIGA Mark II type. The irradiation of the sample used for ensemble NV experiments[7] lasted for 100 hours at normal reactor operation of $250\,\mathrm{kW_{Th}}$ yielding a maximum neutron flux of $10^{13}\,\mathrm{cm^{-2}s^{-1}}$. The exact neutron flux density at the probe holder could not be calculated as neither the probe holder's position in the reactor pool nor the flux distribution was known exactly.

After irradiation the crystal had to be annealed to let the vacancies recombine with the nitrogen impurities. A tube furnace was used to reach desired temperatures of 890°C. A quartz glass tube was continuously flooded with argon to avoid oxidation of the diamond. The diamond was placed in a ceramic dish with several small pieces of Zirconium plate to getter residual oxygen. The suitable duration had previously been tested and therefore 3 h of maximum temperature were applied with a 5h heating up before and approximately 6 h of cool-down afterwards.

[7] Sample BS3-3B

5.3.1.2 Cleaning by etching

For NV fluorescence microscopy as well as for constructing micro-structures upon the diamond surface, the surface has to be cleaned thoroughly. Besides dirt, graphite layers are a particular problem: they are not just scattering light, but they are also electric conductors. Any graphite layers on the surface can eventually short electronic structures, change their impedance and affect the geometry of the magnetic field. Usually such graphite layers appear on the thin sides of the diamond. This issues from the cutting process of diamonds grown from a chemical-vapor-deposition (CVD) process. The diamond sheet, created by the CVD, is cut into pieces by a CO_2-Laser that sublimates carbon atoms. Unfortunately thermal interaction is inevitable and thus diamond locally recrystallizes to graphite. Graphite layers also occur on annealed diamonds that suffered too much heat exposure. On such samples the graphite appears as a coarse, discontinuous layer with a spot-like pattern. One can measure the reduction of the surface resistance by 3 orders of magnitude. While the resistance along the edges of our typical cleaned diamonds is on the order of 10 MΩ, it is only a few kΩ for uncleaned samples.

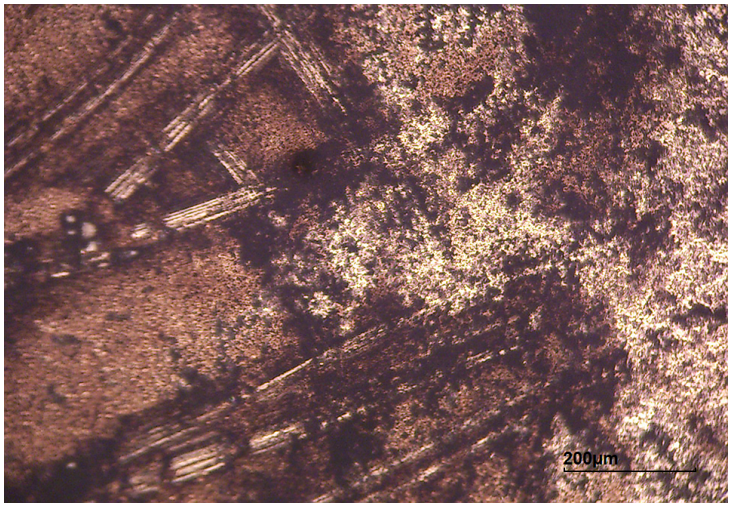

Figure 5.18: The surface of the diamond sample shows severe graphitization after annealing at 890°C.

To remove graphite residuals we use a 1:1:1 mixture of sulfuric (concentrated to 65%), nitric (65%) and perchloric acids (70%). Additionally to the general safety rules when handling acids, it shall be noted that concentrated perchloric acid may explode at temperatures over 50°C and sulphuric acid creates vast amounts of heat (95.4 kJ/mol at 25°C) when mixed with water. As all acids have a highly oxidative effect, cations with a standard electrode potential higher than hydrogen can be bound. Although this solvent is able to create carbocations it is not able to break the covalent bonds of diamond.

Diamond is known [RFR99] to be chemically inert[8] below temperatures of 700°C. In order to increase reactivity, the acid mixture is heated up to 280°C, which is far above the boiling point of several ingredients on their own. Boiling the mixture would lead to an extensive loss of solvent, therefore a backflow condenser was used. The procedure was carried out for 60 minutes and leaves no visible or electrically measurable traces.

5.3.1.3 Identification of sample sides

For production reasons a type IIb CVD-diamond sample has one side comprising a much higher NV-density than the other, which I denote as the rich and the poor side. Whereas the rich side contains a suitable number of NVs for the experiments with the confocal fluorescence microscope, the poor side still does contain a few NVs, but they are rather hard to find. In order to ensure sample fabrication on the rich side, the number of NVs was counted manually beforehand. The results varied between 3 and 72 NVs per cube of 20 µm edge length on the rich side and 0 and 1 NVs on the poor side.

The sides were recorded via photographs through a wide-field microscope. For some samples the sides were indiscernible by vision so I marked one side by abrading an edge. Care has to be taken, as it is undesirable to leave any scars elsewhere on the diamond surface. Diamond sandpaper does not work properly, as the corners of the sample cut into the paper and misplaced diamond grains may damage the surface. Using a glass cutter also endangers the diamond, as diamond can easily be cleaved, especially in the [111] plane. It proved to be the best method to use a worn diamond file with a drop of oil on it to keep loosened diamond pieces from jumping onto the samples surface.

5.3.2 Optical lithography and thin film deposition

The first sample that was actually manufactured into an on-diamond-circuit was the sample BS3-3B. It is a neutron irradiated, thus black, type Ib CVD diamond, rich in nitrogen, with a size of $2.9 \times 2.9 \times 0.5$ mm. I chose that co-planar wave guide design, which was the most heavily tapered one with the smallest short circuit loop. The decision was made mostly due to space restrictions, but my preference for the ring compared to a linear short arises from considerations mentioned in section 5.1.

A lithographic mask (chrome on glass) suitable for contact-lithography was produced at the ZMNS. Technician Matthias Stüwe and me performed the lithography at the ZMNS cleanroom.

The photo-lithography process is illustrated in figure 5.19. The first step is to apply a layer of photo-resist with appropriate thickness to the diamond. One common mechanism to obtain a layer of defined thickness is spin coating. The sample is mounted

[8] Diamond begins to be soluble in a mixture of potassium dichromate and sulphuric acid at 700°C. This super-acid can be used to clean off graphite layers at low temperatures [Vog05].

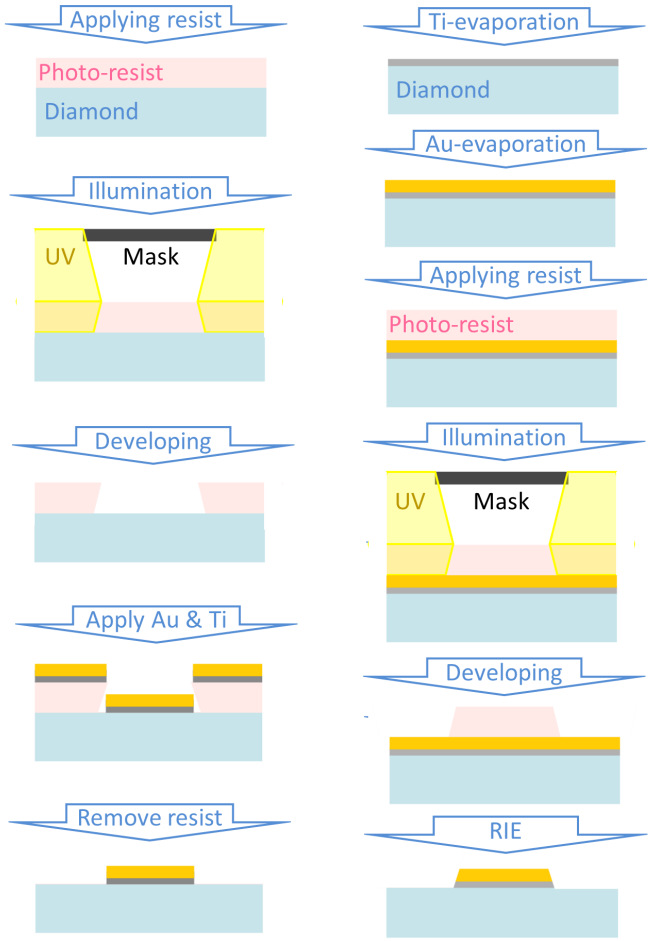

Figure 5.19: Comparison of the processing steps for the lift-off technique (left) and an eroding etch (right) like reactive ion etching.

centrally on a rotary disc, held in place by underpressure created through a suction hole in the disc. A drop of resist is poured onto the sample before ramping up the rotation speed of the wheel. One problem was that the diamond was far too small for the suction hole. Consequently, the diamond was glued to a piece of silicon (which makes it necessary to carefully clean the sample in the very last step of the manufacturing, as the glue itself might fluoresce). The fixation to that base was achieved using a so-called carbon pad, which is a very sticky, chemically and physically quite resistant sticker of 1 cm diameter. A rule of thumb is to use at least twice the thickness of resist compared to the thickness of the gold layer when applying resist via spin coating for a subsequent lift-off procedure or ion etching. The use of negative (AZ nLof 2070) photo resist and 4000 rotations per minute for 35 seconds led to 4 µm of resist. Afterwards the sample - removed from the base - is "baked" at 120°C for 2 minutes, to evaporate the solvent and

water and stabilize the resist.

The sample, again fixed to silicon base, is inserted into the mask aligner[9]. Using a microscope one is able to align the sample to the mask. But the microscope is only available when the sample holder is moved close to the mask. Additionally the sample is drawn near the mask by reducing the air pressure between the plate holding the sample and the mask. The ideal pressure has to be adjusted to a predefined setting, then the sample is released again before the final settings for the exposure can be made. Sometimes the sample sticks to the mask, falls down and thus the position is lost. The exposure settings were 7 seconds at around 200 W of ultraviolet light. As the resist is a negative photo resist it gets dissolved by the developer solution where it was not exposed to UV light.

The resists data sheet recommends to bake the sample again. Afterwards one has to let it cool off before putting the sample into the cold developer, otherwise cracks may corrupt the lithography. The sample was immersed into the developer MIF726 for 120 s, which resolved the resist in the shadowed regions. Afterwards the sample was immediately cleaned with water to stop the development, as the developer also tends to dissolve unlit areas, though at a significantly smaller rate.

Next, the gold layer has to be applied. It is known that gold does not stick well to silicon and therefore a thin chromium or titanium layer is applied in between. We expected it to be the same with diamond. As chromium has anti-ferromagnetic properties we chose titanium. Further we chose sputtering as the deposition process, as it is easy to handle. The sputterer is first used to carry out the cleaning step by sputtering on an empty sample table. Then the titanium is applied to the sample which can be achieved in one sputtering step as only several tens of nanometres of titanium layer are necessary. In contrast, the sputterer needs about 100 steps for 1 µm of gold layer. Between these steps a one minute break is scheduled to passively let the sample cool off. The sputtering took place at a maximum power of 50 W.

Unfortunately, we observed increased bubble formation with thicker gold layers chosen to be sputtered onto the sample. We suspect the reason for this to be heat, which is insufficiently carried away and makes the gold plate expand much more than the diamond, so it detaches from the substrate and expands upwards. As this deformation is partially plastic it does not recede afterwards (the gold layer would not re-attach itself properly anyway).

5.3.2.1 Lift-off process on larger samples

Because the desired thickness of the gold layer could not be achieved using sputtering we replaced the process with evaporation coating. This technique applies a compact

[9] A Karl Suess MLB4 with 200 W ultraviolet exposure

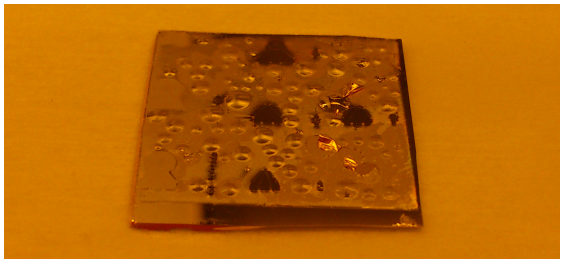

Figure 5.20: Bubbles lift the gold layer off the substrate.

metal film by condensing the metal from the gaseous phase onto the cooled sample. The heat needed for evaporation of the metal is provided by a high current transferred through a tungsten boat holding the metal load. The amount of gold needed to obtain a specific layer thickness was tried out before.

To measure the achieved thickness, partly covered test samples are always inserted in addition to the sample which is going to be used for lithography. The step hight between the covered and uncovered sites were measured with a stylus profilometer named DEKTAK[10]. In the evaporation process the load of the boat usually gets completely depleted. Therefore, the amount of gold inserted into the boat relates directly to the thickness of the gold layer created in the evaporation process. For each µm of gold layer we used up 2 g of gold. The titanium layer thickness cannot be measured that way, instead it is measured using a quartz sensor in the evaporation chamber: this sensor consists of a uncovered quartz oscillator which gets coated by the evaporating metal just like the sample, changing its resonance frequency. This shift is converted into coating thickness, based on user-supplied parameters such as material density. Since calibration data for the quartz sensor was available, little further effort was required to obtain a 30 nm titanium layer.

The process of evaporation starts with filling two tungsten boats with one titanium pellet and 2g of gold droplets respectively. These are mounted between two pairs of massive electrical connection sockets, providing the current necessary to heat the boats up to several hundred degrees (gold evaporates at 3129 K, titanium at 3560 K and the boat itself at 5828 K). The evaporation chamber is then evacuated to about 10^{-1} mPa. At such pressures the thin hot metal gas drifts away radially from the source without any oxidation taking place. Reaching this pressure with the ZMNS evaporator (Balzers PLS-500 Labor System) needed about 3 hours. When the base pressure is reached the shutter is closed, meaning that a simple plate is moved in between the sample and the vapour source. It will be opened again once the optimal evaporation rate has been achieved. An optimal evaporation rate is a compromise between a long waiting time and an excessive heat transfer to the sample. We used a rate well tested by ZMNS members. In order to avoid contamination of the metal layers on the sample it is advisable to

[10]resolution of up to 1 $\AA$

open the shutter not until some time after the metal has melted, since this ensures that organic surface impurities have already eradiated. The current heating the boats is controlled manually; a proper current is adjusted using visual control and the sensor's rate measurement. The titanium layer was applied at a growth rate of some parts of nm per second whereas the growth rate of the gold layer was about $2.5\,nm/s$. Unfortunately the current control knob scale is not calibrated to Amperes, but one can expect several tens of amps running through the boat. Boats get regularly destroyed due to the stress of being heated or a rapid temperature change when the cooling effect of evaporation falls after the evaporation material has been depleted.

After the evaporation step, sample BS3-3b was covered with gold, with the underlying structures clearly visible as relief-like patterns. A $90°C$ bath in NEP (N-Ethyl-2-Pyrrolidone, a highly effective solvent for organics, especially for resist residuals, which is less toxic than its predecessor NEP) was used to remove the resist beneath the gold (and titanium). On all sites designated to have a metal structure the metal indeed stuck to the diamond whereas elsewhere it was washed away with the resolved resist. In summary, the fabrication on sample BS3-3b worked as expected. For an evaluation of the resulting microwave properties see section 6.3.

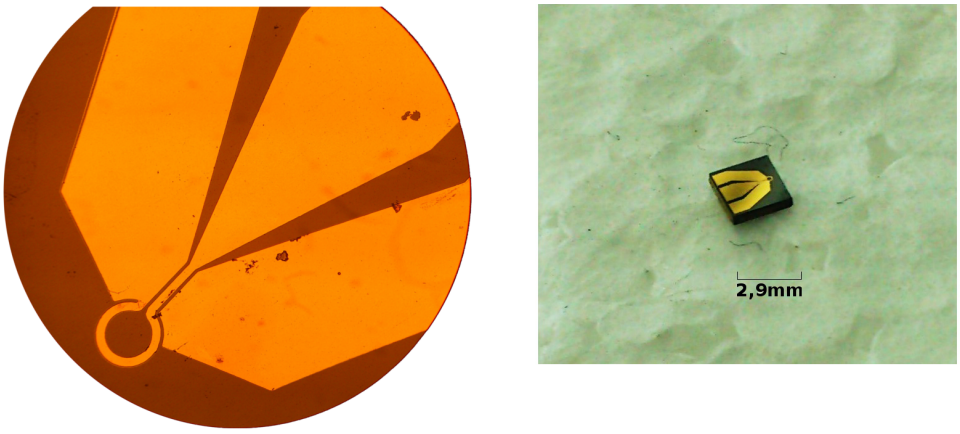

Figure 5.21: The black diamond BS3-3b seen on the right with its visible gold structure is viewed through a microscope on the left. The structure almost perfectly matches the pattern except for a small particle on the edge of the ring.

5.3.3 Bonding

As it is necessary to electrically connect the electronic micro structure on the diamond to the copper co-planar wave guide on the sample holder, bonding wires are a proper option. Bonding wires have a typical diameter of 25 µm and are used to form electrical connections between locations usually some tenth of a millimetre apart. As soldering is

impractical at such dimensions, a machine similar to a sewing machine is used. That machine's needle does not penetrate the underlying material, but rubs the bonding wire onto the surface using ultrasonic vibrations. This destroys the oxidation layer and the punctually created heat melts the wire to connect it with the underlying surface. Now the needle can be carefully lifted and shifted to the location of the next connection, where it is pushed down again, once more initiating the vibrations. The bridge thus generated is under tension, depending on the curvature and the material stiffness. Pushing the needle down therefore causes a risk of tearing the first connection off. By releasing the needle for a second time, it tears off the filament after the connecting point, if the connection was tight enough.

For my samples aluminium bonds were used, as these were known to be suitable for both gold and copper surfaces. The distance the bonds had to span was about 1 mm. Bonding was conducted by Christian Koller with a Kulicke & Soffa Industries inc. 4523A Digital manual wire bonder at the ZMNS. About six bonds were successfully drawn to connect the ground conductors of the sample and coplanar wave-guide for each side, as well as eight bonds for the centre conductor.

5.3.4 Reactive ion etching on smaller samples

Unfortunately, the procedure described in the previous chapter did not work for the slightly smaller single-NV samples: With 2×2 millimetres the diamond sample (sample A2, clear type IIa) is so small that the application of a flat layer resist becomes impossible using spin coating: on the edges of the sample a bulge of resist will form as well as a hump in the centre and further smaller arbitrary buckles. Without a flat layer of resist, it is difficult to move the sample close enough to the mask to obtain a sharp image, which eventually results in disconnected electrical conductors. Pressing the sample forcefully to the mask causes fatal damage to the resist. A careful optical inspection of the lithography needs to be carried out before any other processing steps are conducted. Another problem appeared to be the unbalanced development of the resist due to the varying deepness of the valleys into which the developer has to cut. While in some areas the developer would still need time to cut deep enough into the resist to reach the diamond's surface, other parts are soon fully free of superfluous resist. Furthermore, resist in the surrounding area becomes unfavorably dissolved, eventually reducing the undercut. The metal applied to the sample afterwards should be placed on top of the resist or down on the diamond, but due to insufficient undercut the levels are not separated everywhere and connections of the gold layers remain. When removing the upper level of gold while dissolving the resist, that gold tends to rip off parts of the lower gold level, which again results in broken conductors. This is essentially caused by the diamond's surface, which is not easy to adhere strongly to, not even when applying a titanium adhesion layer.

A first approach to avoid these problems is to apply reactive ion etching (RIE) with argon ions, in order to avoid chemical reactions with the sample. The term "reactive" is thus not appropriate, as only the kinetic aspect is used. By using this technique,

mechanical processes, which would rip off parts of the created structure, can be avoided. Another advantage of this process is that no organic material (like resist or solvent) can remain under the adhesion layer.

The sample was first covered with 30 nm of titanium and a 1 µm gold layer via evaporation coating. On top of that a layer of positive (AZ5214) photo-resist was applied (spin coating at 2000 rpm for 35 s) and baked for 60 s at $100°C$. After lithography had been performed as mentioned before this sample was immersed into the developer MIF726 for 45 s and then rinsed with water. With the resist removed from areas where the metal was to abraded, the sample was inserted into a reactive ion etching device (Oxford PlasmaPro System 100 (R&D)). As several gases (e.g. oxygen, chlorine, argon) are used frequently, it is important to clean pipes that transport more than one kind of gas of unwanted residues before operating the machine. This can easily be done by generously evacuating the chamber down to 5×10^{-7} mbar, while the valve connecting it to the appropriate supply pipe is kept open. The gas of choice is argon in this case since we are not interested in the chemically reactive but kinetic aspect of the process as gold is chemically inert anyway. After a series of tests it turned out that the sample needed to be exposed for 45 minutes at 200 W ICP (inductively coupled plasma) power and at a base pressure of 5 mTorr to etch through all of the thick metal layers and expose the diamond on desired sites. A strike pressure of 40 mTorr was necessary to ignite the plasma, driven by a 13.56 MHz radio source, and a 20 sccm flux was used to blow away particles.

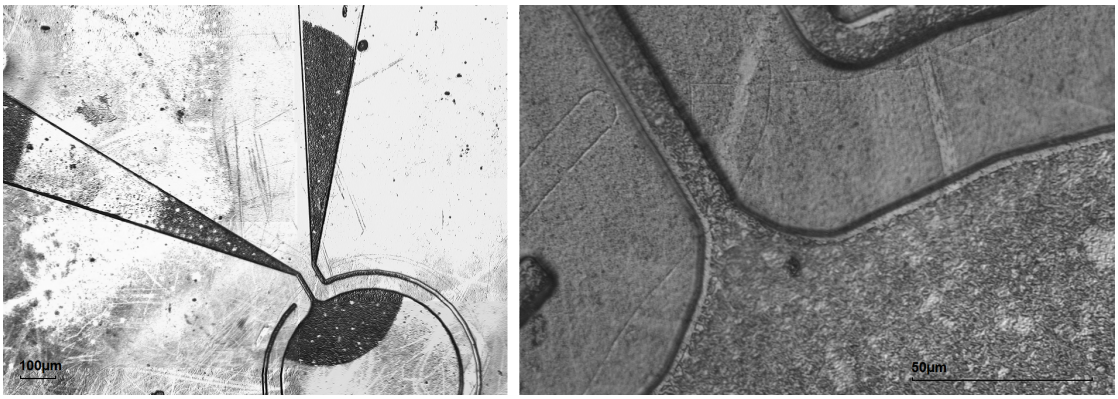

Figure 5.22: The centre of the sample A2 shows an area of clearly visible roughness due to heavy etching of the diamond surface by ion milling.

Unfortunately the duration required for this etching process is so long that especially in the centre of the sample too much material is stripped off, producing different thickness of the gold layers, imprecise shapes or broken conduction lines. Occasionally, also wrong connections, forming shorts, are observed for an unknown reason. It seems that, due to the long duration of the ion bombardment, there is some heating of the sample,

which causes the resist to move or melt. The experiment described in section 5.3.4.2 underlines that hypothesis. Finally the surface of the diamond gets roughened in the sample's centre, which renders that area unusable for measurements with the confocal microscope as light is arbitrarily scattered there.

5.3.4.1 A silver mask for local passivation

The need for a manufacturing process, which is almost independent of the spatially varying resist thickness initiated the development of a new approach. An additional very thin metal layer should protect the gold from the etchant. Though of the same shape as the developed resist, it is even, because it is applied by evaporation or sputtering. Any further processing is therefore eased. An additional advantage: since wet-chemical etching is possible, the diamond will not get harmed in any way.

Now, the pattern of the developed resist has to be brought to the newly introduced thin metal layer – let us call it stencil so as not to confuse it with the mask – which is again done using the kinetic aspect of RIE. Since the stencil layer is thin compared to the gold and resist it is easily entirely penetrated. This process depends exclusively on whether the stencil layer is fully penetrated or not. The amount of material removed beneath the stencil layer (i.e. gold) does not matter, as that material is going to be removed in the following process anyway. On sites that are not desired to be freed from gold, the resist is most probably much thicker than the stencil, so the stencil will hopefully not even be scratched. After this step, the resist may be cleaned off with a longer bath in warm acetone or NEP. Removal of the organic solvents is advisable.

A stencil material resistant to the next etching process has to be chosen. Using aqua regia one can effectively dissolve gold ($2\,\mathrm{Au} + 2\,\mathrm{NOCl} + 6\,\mathrm{Cl_{nasc.}} + 2\mathrm{HNO_3} \rightarrow 2\mathrm{HAuCl_4} + 4\mathrm{NO_2}$) due to the creation of the highly oxidizing nascent chlorine ($\mathrm{HNO_3} + 3\,\mathrm{HCl} \rightarrow \mathrm{NOCl} + 2\,\mathrm{Cl_{nasc.}} + 2\,\mathrm{H_2O}$) that vigorously binds the trace amounts of $\mathrm{Au^{3+}}$ created by nitric acid. On the other hand it is incapable of attacking ruthenium, tantalum, iridium, osmium, titanium, rhodium and some others due to passivation at least at room temperature. As titanium has been used for the sticky layer before it seemed natural to reuse it for the stencil as well. Further the stencil could be removed with the finally exposed sticky layer applying so-called base piranha. Base piranha is commonly known from the Standard-Clean-1 (SC-1), which is part of the Radio Corporation of America (RCA) clean. This process utilizes ammonium, hydrogen-peroxide and DI-water in a ration of 1:1:5 or with higher water content [var08]. Regrettably, after a long duration of ion etching (more than 40 minutes), which rendered the whole procedure pointless, there were still some misplaced connections left in the stencil layer. Titanium has Mohs' hardness of 6, which is far above that of gold and resist.

Unfortunately all other metals named above are either very hard or unavailable. But silver is a good selection as it is very tender, with a Mohs' hardness of 2.5 to 3. Being

below hydrogen in the activity series it is not soluble by hydrochloric acid, and — above all -– it will not build up a passivation layer. Additionally it is soluble by nitric acid. The reason for its indissolubility in the mixture of hydrochloric and nitric acids is based on the created nascent chlorine, which is able to form a white layer of silver chloride, effectively protecting the silver.

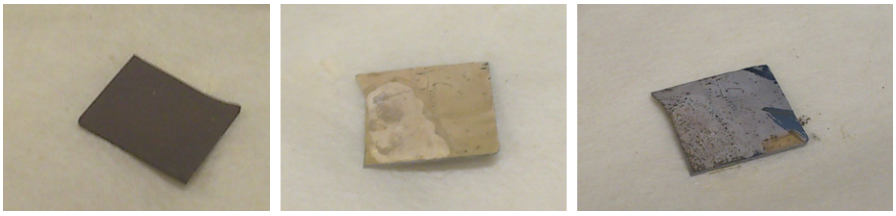

Figure 5.23: The processing steps of the silver-coated sample are oxidation to Ag_2O, the treatment with hydrochloric acid to AgCl and finally the etching with aqua regia, unfortunatly removing the gold due to the porousness of the layer.

The chemical process works indeed as described. 10 minutes of 350 W plasma ashing delivers a dark grey cover of silver oxide Ag_2O. A bath in room-temperature hydrochloric acid for a few minutes allows that layer to be transformed into white silver chloride ($Ag_2O + HCl \rightarrow 2AgCl + H_2O$), which should act as passivation layer. But the final etching in aqua regia for a minute shows the chloride layer to fail, the acid dissolving the gold, while the white patina stays untouched. This is most probably due to the chloride layer being porous and perhaps due to the sputtering process which created a layer of silver particles forming a conglomerate structure rather than a dense layer. Furthermore the chemical reaction changes the size of the crystal material, probably leading to microscopic stress in the layer, breaking small portions off the layer. The fact that it was possible to scrape a fine white powder off the surface demonstrates the unusable structure of the chloride as passivation layer.

5.3.4.2 Cryogenically refined ion etching

Previous experiments with altering layer arrangement inspired me to change the sticky layer thickness from 30-50 nm to around 100 nm. Thus the diamond will not be corroded by the etching ions as the increased thickness allows all gold to be removed on the desired sites, while some titanium is still left on the stronger eroded locations. Another problem addressed by this approach is the somehow molten resist filling up the valleys and thus creating shorts. The reactive ion etching chamber has a liquid nitrogen inlet, which can be utilized for cooling the sample table. We decided that $-40\,°C$ should suffice to freeze the resist under all circumstances. Again, the high heat conductivity of diamond comes in very helpful. As we reduced the temperature the plasma becomes less likely to ignite. Therefore the strike pressure – a pressure higher than the working pressure held until the plasma ignites – has to be adapted (i.e. doubled). After 40 min of ion etching the microscope revealed much sharper edges than ever before, small islands

of gold were completely absent and the titanium layer was fully intact.

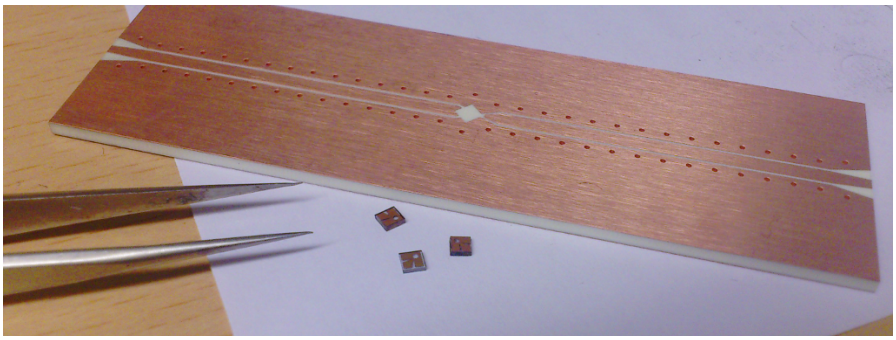

Figure 5.24: Three samples produced using cooled RIE-processing.

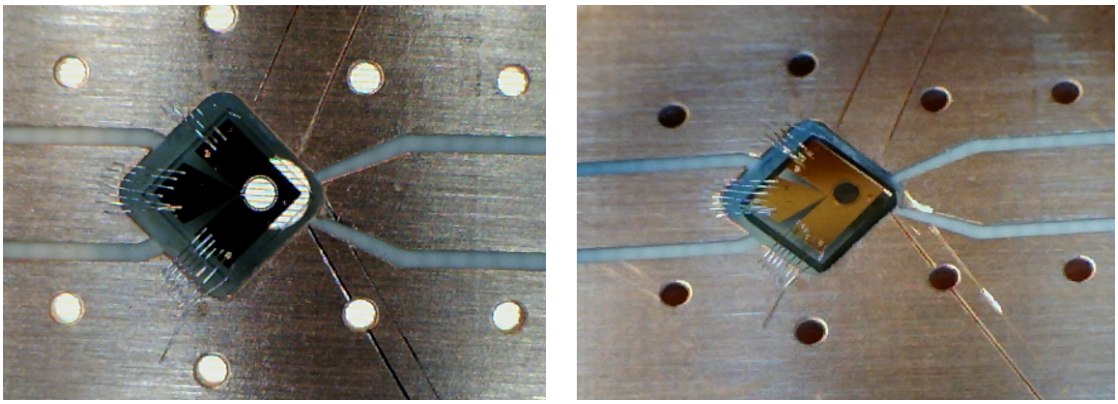

Figure 5.25: A close-up using a low-magnification microscope shows the sample bonded to the sample holder with two illumination directions, from the rear and from above, showing the loop structure and 17 properly applied bonds.

The next step was to remove the titanium. Titanium can effectively be removed by mixtures containing hydrofluoric acid or ammonium fluoride or ammonium bi-fluoride. In order to avoid these dangerous substances base piranha was used as alternative. This mixture under-etches particles and rather noble metallic residues, oxidizes surfaces and electrically charges surfaces and particles to separate them. It does indeed remove thin titanium layers, but rather breaks them off, forming particles suspended in the solvent rather than dissolving them. This makes it hard to control the solvent's behaviour; in particular, thinning the solution makes the titanium removing effect vanquish all of a sudden. Normal piranha acid is reported to work too [var08], but in our experiments it did not: a black layer was formed on the titanium, keeping it intact. Some sources say that reductive acids are to be preferred to oxidizing acids. This explains the trouble with above mixture, which is extremely oxidizing due to the hydrogen peroxide and

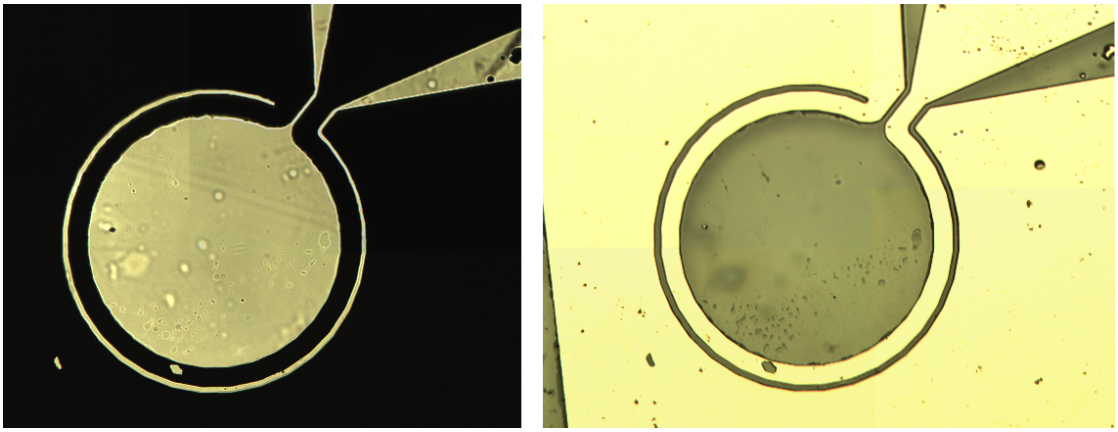

Figure 5.26: Front and back-light microscopy images of the micro structure upon the surface of a 2×2 mm sample. It shows a continuous gap of 10 µm width and a loop of 40 µm width without any interruption.

therefore prohibits the dissolving process by creating passive oxide layers. As Professor Max Bichler pointed out to me, nitric acid should slowly dissolve titanium. According to one source [JCW+06], nitric acid creates a smooth and clean etched surface – unlike hydrofluoric acid – at low etch rates and is thus to be favored, since only 3 nm need to be removed. Etching titanium using nitric acid is only possible for hot pure acid or vapour condensates of nitric acid [azo13], as otherwise the dissolution is prohibited by the oxide layer created in the process, which cannot be penetrated at low temperatures. These technical difficulties led to another solution: oxalic acid, which is able to etch titanium in aqueous solutions of 5% weight and above and at temperatures above 70°C [mi72].

The first test of this solvent utilized an aqueous solution of oxalic acid[11] at maximum concentration at 100°C [12]. Under such conditions almost 50 % of its weight is oxalic acid. Within one and a half hour a titanium sponge particle of 2 mm in diameter was dissolved and left a yellow to brown solution behind. For an examination of the surface etch rate of an aqueous oxalic acid solution, titanium platelets of 50 µm thickness were used. As the top and bottom surface of 3.5×3.5 mm is large compared to the other faces, the etch rate in weight can be directly related to a surface etch rate. This assumption is confirmed

[11] It is not possible to use oxalic acid by itself, because it is not a liquid at room temperature and does not melt at elevated temperatures, but decomposes at 157°C.

[12] To achieve the desired temperature of the solution, the beaker was immersed into a boiling water bath. Both the bath and the beaker were covered to ensure they have the very same temperature. Heating the beaker itself would have required a temperature sensible heating, which was not available. The boiling of the solution is no proper temperature indicator, as the mixture of water and oxalic acid most probably has a higher boiling temperature than water itself. This hypothesis was confirmed, since the solution — unlike the water in the bath -. did not start to boil. Moreover, a boiling solution was not desired, as water would evaporate and thus the concentration would rise. Glass granules were used to prevent boiling retardation.

by the observation that the tiny plate does not visibly shrink from the edges inwards but instead dissolves rapidly in the very last moment before completely disappearing. The plates used were of 99.9 % pure and dense titanium – which agrees with the properties of the evaporated titanium surface produced in the microfabrication process – and have masses of about 2.5-3 mg. The etch rate needs to be known on the order of magnitude, thus the required precision of temperature and concentration is not too important. As a maximum saturated solution at 100°C appeared too aggressive, a lower concentration was chosen. A 9-10 % concentration can be easily achieved by producing a completely saturated solution at 20°C. The etching was carried out at 100°C, because the etch would stay inert at room temperature. The estimated surface etch rates are:

Platelet's mass [mg]	Duration [min]	Final mass [mg]	Etch rate $[nm/s]$
2.60	330	0.00	0.13
2.52	280	0.00	0.15
2.52	329	0.05	0.12
2.60	317	0.04	0.13
3.00	180	1.28	0.14

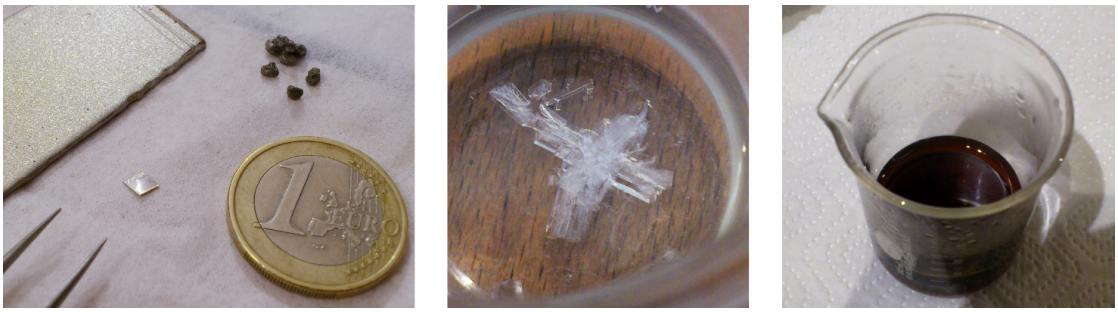

Figure 5.27: The picture to the left shows the titanium sample used for estimating the surface etch rate, with massive titanium and titanium sponge depicted above. The image in the middle shows an oxalic acid crystal forming in a cooled down and therefore over-saturated aqueous solution. The picture to the right shows the solution after large quantities of titanium sponge were dissolved in it.

Obtaining a final measurable mass from the remaining titanium samples proved particularly difficult. Even before the corners start becoming round, the titanium sheet turns translucent and therefore almost impossible to recover in one piece. For the final sample a duration was chosen in which no visible effects occurred, but the remainder could be weighted in form of a compact plate. As a conclusion, a 12 minute immersion of the prepared diamond sample in 10 % aqueous oxalic acid solution of 100°C should sufficiently remove the titanium residuum.

6 ODMR experiments with NVs

6.1 Continuous wave spectrum

We now employ the measurement technique introduced in section 3.3 [HW02] in order to explore the spin resonance spectrum and dephasing environment of NV centers and evaluate the performance of the MW micro-structures.

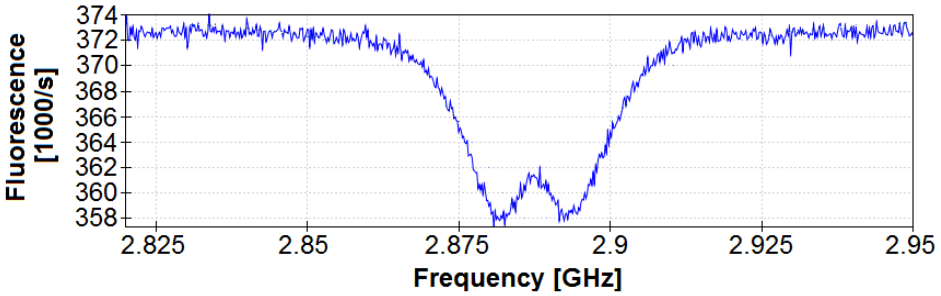

Figure 6.1: ODMR spectrum of an ensemble of NVs in zero magnetic field. Two transitions at $D \pm E$ can be identified, which correspond to the $m_s = 0$ to $m_s = \pm 1$ transitions resulting from the Hamiltonian expressed in equation 6.3. The peaks are symmetric around 2.88 GHz, which matches the zero-field splitting D. This spectrum was integrated for about 10^6 to 10^7 cycles.

In order to record an ODMR spectrum, we sweep the frequency of a MW field while counting fluorescence intensity, resulting in a plot as shown in figure 6.1). An ODMR spectrum is recorded under constant illumination in order to polarize the system into its bright state $m_s = 0$, when the MW is off-resonant with regards to the spin transition. Upon resonance, spin transitions are induced, which leads to a higher proportion of dark states $m_s = \pm 1$ start to mix, creating a lower luminescence rate. The spectrum in figure 6.1 shows characteristic Voigt profiles for each transition, which are a Lorentzians created by the natural line width convoluted with a Gaussian distribution in the case of ensemble NV samples, that results from the individual lattice strain at each NV in the focal spot. The FWHM of these dips equals $\frac{1}{\pi T_2^*}$.

Spin Hamiltonian of the NV- ground state triplet The eigenenergies of the spin-system can be found by diagonalizing its Hamiltonian $\hat{\mathcal{H}}_S$. For spin resonance experiments on NVs, we consider the Hamiltonian:

$$\hat{\mathcal{H}}_{\mathrm{S}} = \hat{\mathcal{H}}_{\mathrm{zfs}} + \hat{\mathcal{H}}_{\mathrm{Z}} + \hat{\mathcal{H}}_{\mathrm{hf}} \tag{6.1}$$

Each of the Hamiltonians in this composition describes an effect that particularly influencing the resonances of an NV system. These are:

- Zero-field splitting (zfs) $\hat{\mathcal{H}}_{\mathrm{zfs}}$
- Electron and nuclear Zeeman (Z) interaction $\hat{\mathcal{H}}_{\mathrm{Z}}$
- Hyperfine interaction (hf) $\hat{\mathcal{H}}_{\mathrm{hf}}$

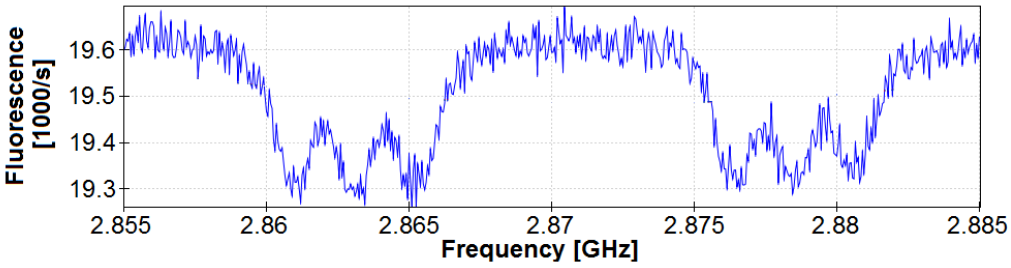

Figure 6.2: By measuring at lower microwave and laser power, power broadening can be avoided and a greater resolution is achieved. This allows the observation of further splitting into three equally high peaks, which can be interpreted as interaction with a triplet state. Considering that the most likely spin one system in the vicinity of the NV is a nitrogen nucleus a splitting of about 2.2 MHz is expected[Chi07] which is in good accordance with this measurement.

6.1.1 Zeemann effect

The potential energy E_{pot} of a magnetic moment $\vec{\mu}$ in a magnetic field $\vec{B}$ is dependent on the strength of that field: $E_{pot} = -\vec{\mu}\vec{B}$. The same applies to spins ($\vec{S}$). For simplicity let's assume a magnetic field $\vec{B} = B\vec{e}_z$, therefore S_z and m_s are good quantum numbers.

$$\hat{\mathcal{H}}_{\mathrm{Z}} = -\gamma_e \hbar B S_z \tag{6.2}$$

with $\gamma_e = g_e \mu_b / h = -28\,\mathrm{GHz/T}$ being the gyromagnetic ratio for an electron. The full Hamiltonian can be expressed as:

$$\hat{\mathcal{H}}_{\mathrm{Spin}} = \frac{1}{\hbar} g_e \mu_B \vec{B}_0 \hat{\vec{S}} + \frac{1}{\hbar^2}\left(D\hat{S}_z^2 + E\left(\hat{S}_x^2 - \hat{S}_y^2\right)\right). \tag{6.3}$$

Throughout this work, we can neglect the nuclear Zeeman effect, since it is smaller than the electron Zeeman effect by a factor 2000. The fist-order Zeeman splitting for a single NV amounts to $m_s \cdot 2.8\,\mathrm{MHz/G}$.

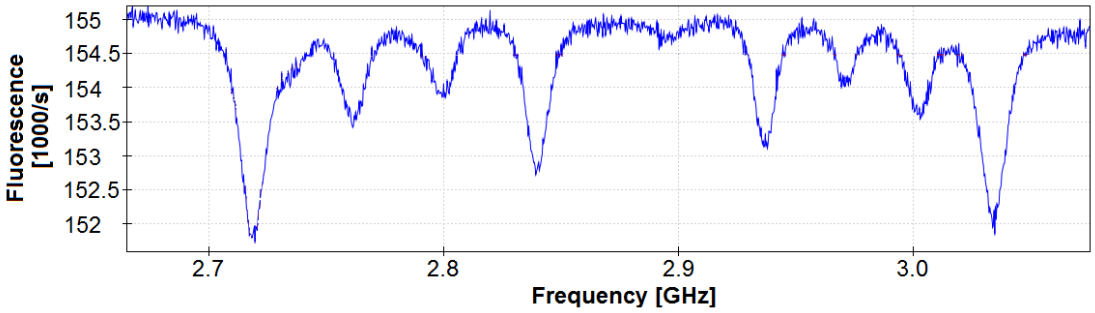

Figure 6.3: When an external static magnetic field is applied to an NV, the energy levels split due to the Zeemann effect. At maximum eight peaks occur in the ODMR spectrum of an ensemble NV diamond. Since the component of the magnetic field along each of the four NV axes can be different, the energy levels experience individual Zeemann shifts. The peaks are generally not equal in strength, because the NVs along each axis can have a distinct transition probability due to the orientation of the MW field vector with respect to the transition dipole axis.

Diagonalization of the full Hamiltonian For including the Zeeman interaction into the spin Hamiltonian one needs to add the respective Hamiltonians of zero-field-splitting and Zeemann interaction:

$$\hat{\mathcal{H}}_{\text{Spin}} = \hat{\mathcal{H}}_{\text{zfs}} + \hat{\mathcal{H}}_{\text{Z}} = \begin{pmatrix} D-E & -i\gamma_e B_z & i\gamma_e B_y \\ i\gamma_e B_z & D+E & -i\gamma_e B_x \\ -i\gamma_e B_y & i\gamma_e B_x & 0 \end{pmatrix} \tag{6.4}$$

in the vector basis $\{S_x, S_y, S_y\}$. The in order to calculate the transition energies ϵ, one needs to solve the Schrödinger-equation $\hat{\mathcal{H}}_{\text{Spin}}\sigma = \epsilon\sigma$ for the spin-wave-function σ fir each spin state [HW02]. Analytical solutions are easily calculated for special directions of the magnetic field regarding the NV axes. Assuming the magnetic field along z-direction one can derive the eigenvalues dependent on m_s:

$$\epsilon(\pm 1) = D + \sqrt{E^2 + (g_e \mu_z B_z)^2} \tag{6.5}$$

$$\epsilon(0) = 0 \tag{6.6}$$

As for coupled pendulums an avoided crossing of eigenfrequencies dependent on the field strength can be observed. Such a level-anti-crossing (LAC) [CGMB90] can be observed for the ground state at a magnetic field of 500 G and at 1025 G for the excited state. The degenerate eigenstates for $m_s = \pm 1$ are $\epsilon_{\pm 1} = D$ higher in energy than the $m_s = 0$ energy (if there is no strain E). If the Hamiltonian for zero-field splitting and Zeemann effect are added, the resulting eigenvalues show LAC at the appropriate field strength.

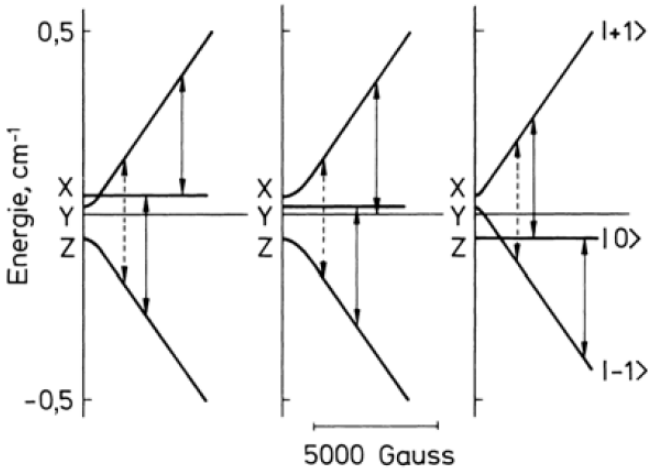

Figure 6.4: This picture illustrates the term scheme of a triplet state (example of naphthalene given in [HW02]) as function of an external magnetic field B_0. The direction of the field is – from left to right – along the long axis, the short axis and the axis perpendicular to the molecule plane, respectively.

Four NV axis orientations occur in the diamond lattice and for each NV axis two orientations are possible. The energy levels for the $m_s = \pm 1$ states equal those of the $m_s = \mp 1$ states of an NV orientated in opposite direction; thus, the NV orientations along the same NV axis are indiscernible. Consequently eight peaks can occur in the ODMR spectrum of an ensemble NV sample. Since the component of the magnetic field along each of the four NV axes can be different, the eight resulting energy levels experience individual Zeemann shifts. In general, the peaks are not equal in strength, because the NVs along each axis can have a distinct transition probability. The orientation of the MW field vector with respect to the transition dipole axis is generally different for each of the four NV axis directions; hence different transition strengths occur. By selecting a magnetic field direction along an NV axis three other axes will show identical resonances, therefore the number of peaks observed halves. It is possible to reduce the number of peaks observed by another factor of two by selecting an angle in the middle between two NV directions. Thus the projections of the NV axis onto the magnetic field vector is equal for all directions.

It is noteworthy, that the NV axis is a good axis for the spin projection quantum number for fields lower than the zero field splitting. For high magnetic fields, the Zeeman effect becomes dominant and the spin along the NV axis is not a good quantum number anymore, instead the axis of the magnetic field becomes the quantization axis.

6.1.2 Microwave power broadening

Power broadening is encountered twice at NV experiments. On one hand there is the power broadening due to the laser power, which becomes significant for single NV observations only. For our ensemble NV diamond samples the number of two-level systems is much to high and the power of the laser too low to observe any saturation effects. Fortunately a line broadening does not disturb magnetic resonance experiments because the optical excitation is pumped in the broad phonon-side-band far off the zero-phonon-line.

In contrast the power broadening introduced by strong microwave irradiation is of significance for both, single and ensemble NV experiments. Dreau et al.[DLR+11] give the following expression for the line shape of an NV spin transition in ODMR:

$$\mathcal{I}(\nu_m) = \mathcal{R}\left(1 - \mathcal{C}\cdot\mathcal{F}\left(\frac{\nu_m - \nu_0}{\Delta\nu}\right)\right), \tag{6.7}$$

with $\mathcal{R}$ being the rate of detected photons. $\mathcal{C}$ is the maximum ODMR contrast, as determined by the transition dynamics of the system. $\mathcal{F}$ is the line-shape: A Lorentzian in the single-NV case, a convolution of a Lorentzian with the Gaussian distribution of resonance frequencies in an inhomogeneous ensemble. Its arguments are the microwave frequency ν_m which can be detuned from the resonance frequency ν_0 and the line width $\Delta\nu$, which is the quantity characterizing the broadening. Usually this is a FWHM for Lorentzian and a standard deviation for Gaussian distributions, and reflects the variety of different spin precession frequencies and thus the dephasing rate T_2. The derived formula for the line width,

$$\Delta\nu = \frac{\Gamma_c^\infty}{2\pi}\sqrt{\left(\frac{s}{s+1}\right)^2 + \frac{\Omega_R^2}{\Gamma_c^\infty\Gamma_p^\infty}}, \tag{6.8}$$

particularly rises with the amplitude of the incoming microwave signal. In the model of that paper, the rates Γ_p^∞ and Γ_c^∞ are introduced. The former is the rate of polarization at saturation, which is fixed by the lifetime of the metastable state (It is about 200 ns at room temperature which results in $\Gamma_p^\infty \approx 5\cdot 10^6\,\mathrm{s}^{-1}$). Optical pumping of the system also causes relaxation of the spin coherence, thus the number of optical cycles per second also influences the line width. The rate at saturation is named Γ_c^∞ and is set by the excited state lifetime, which is on the order of 13 ns, creating a rate of about $8\cdot 10^7\,\mathrm{s}^{-1}$. The polarization and optical pumping rates for finite laser powers are related to the saturated values by: $\frac{s}{1+s}$ with s being the ratio between actual optical pumping power and the saturation pumping power. Ω_R is the Rabi frequency at which the spin is rotated, it is proportional to the MW amplitude.

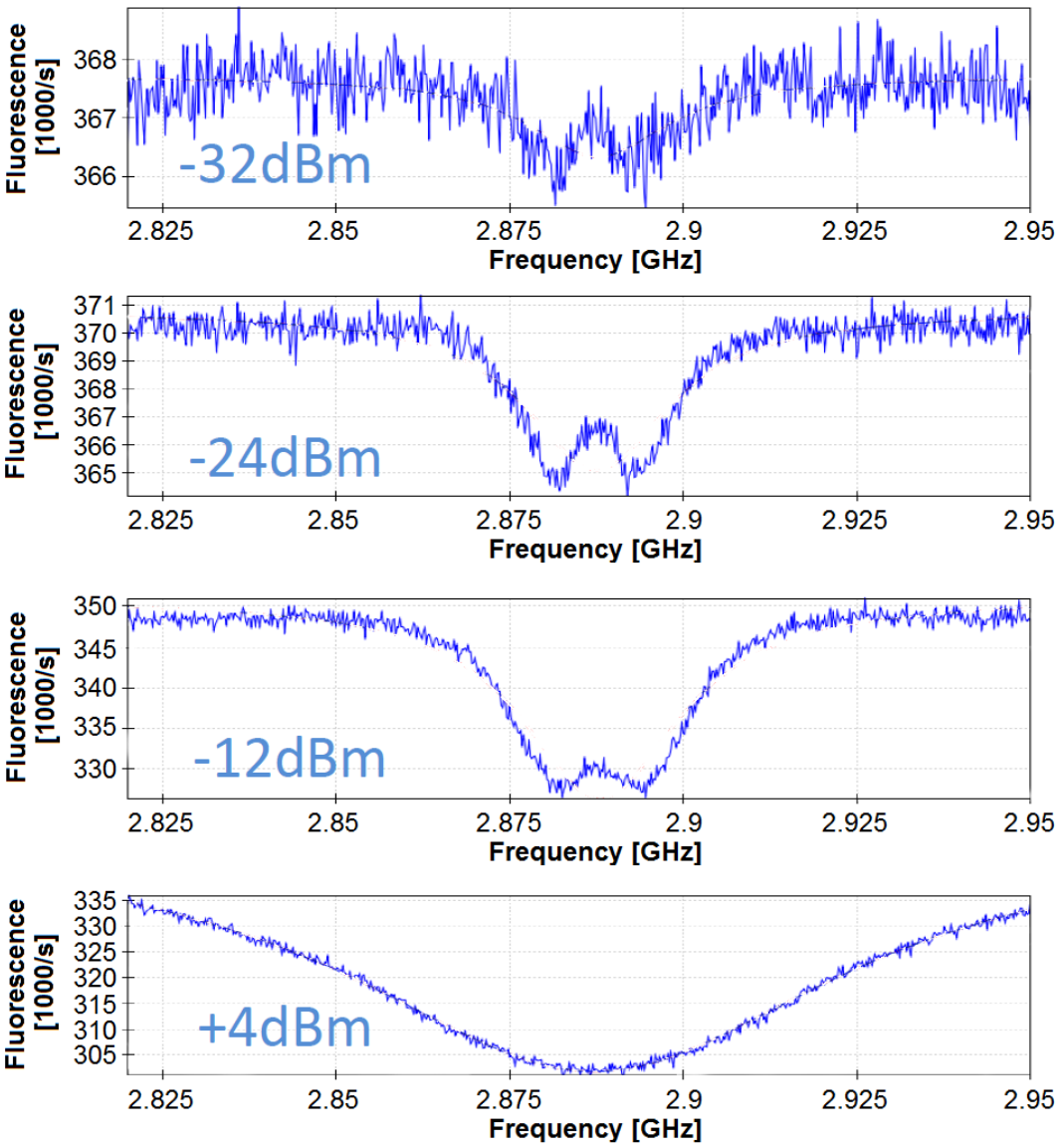

Figure 6.5: This image shows the ODMR spectra of a peak associated with one NV direction (these were separated by choosing a proper angle of an external magnetic field, such that all NV directions were subjected to a different Zeemann-splitting) at different microwave power levels. The denoted power refers to the output power at the signal generator.

6.2 Coherent manipulation of NV spins

For rotations around an axis perpendicular to the z-axis need to be implemented to obtain the complete set of single-qubit transformations. Therefore pulses are formed, notably pi- and pi-half-pulses. In order to prove the ability to perform coherent spin manipulations continuous driving is sufficient, as it shows Rabi oscillations.
Quantum information processing using NVs requires to be able to rotate a spin qubit around all the three axes. For rotating it around the z-axis, we simply let it precess freely. One full rotation around the z-axis requires one Larmor period of time (see section 2.2.1). For the other two axes, we apply an alternating electromagnetic field oriented parallel to these axes, and resonant with the Larmor frequency. This field, a microwave field on the order of a few GHz, drives Rabi oscillations of the spin qubit (see section 2.2.3). By applying this field only for a specific fraction of the Rabi period, it is possible to rotate the spin by a specific angle, such as π or $\pi/2$. In the following we discuss the pulsed measurement scheme employed in our experiments and evaluate the results.

6.2.1 Measurement sequence for pulsed experiments

The driving of Rabi oscillation is one example of a single qubit gate. Like all our pulsed measurement sequences it consists of three basic parts:

- Initialisation: In order to polarize the centers in $m_s = 0$, we excite the centers optically (1 mW, 532 nm) for 3 µs in order to achieve a polarization of approximately 80 % [Put11]. The spin-selective shelving mechanism described in chapter 3 initializes the centers in $m_s = 0$. Constant illumination is maintained for 3 µs at saturation power and reaches a polarization of approximately 80 % [Put11].
- Manipulation: Hereafter a programmable MW pulse sequence is applied driving the Rabi oscillation. The durations that can be achieved with the experimental setup range from 12.5 ns to several hundred µs. The resolution is limited to 2.5 ns.
- Readout: After the MW pulse sequence is finished the readout starts. It consists of one measurement of photo-luminescence at the beginning of an illumination pulse and another towards the end of the pulse, 3 µs later. The integrated photon count of the first measurement depends on the spin state of the NV whereas the second measurement acts as reference measuring the steaty-state photon count. The duration of the first measurement is chosen to be approximately 0.5 µs in order to comprise exclusively the time frame, in which the luminescence rate differs from the steady-state luminescence rate.

In order to speed up measurements the reference measurement serves as initialization for the next measurement.

A small magnetic field up to 100 G was used to increase the difference between energy levels. Due to the Zeemann effect the energy difference between $m_s = 0$ and $m_s = -1$

states decreases, whereas it increases between $m_s = 0$ and $m_s = 1$ states. This separation prevents transitions between more than two states, which would cause a beating of the according Rabi oscillations.

6.2.2 Using rabi oscillations for field mapping

In order to verify the simulated EM field strength distribution around the micro-structures, we exploit the fact that the Rabi frequency increases linearly with the magnetic field strength. Since the locations at which NVs are available are restricted in ultra-pure samples, we chose to use samples containing high densities of NVs for the task of mapping the field distribution. Although the coherence time in these samples is much shorter (hundreds of ns instead of hundreds of µs), we can still observe Rabi oscillations. In addition, single NVs have the disadvantage of having four possible directions for the NV axis. It is advisable to compare spots on a curve that are exposed to the same field direction, because the transition rates and thus the hight of the peaks in the ODMR spectrum depend on the angle between MW field and NV axis direction.

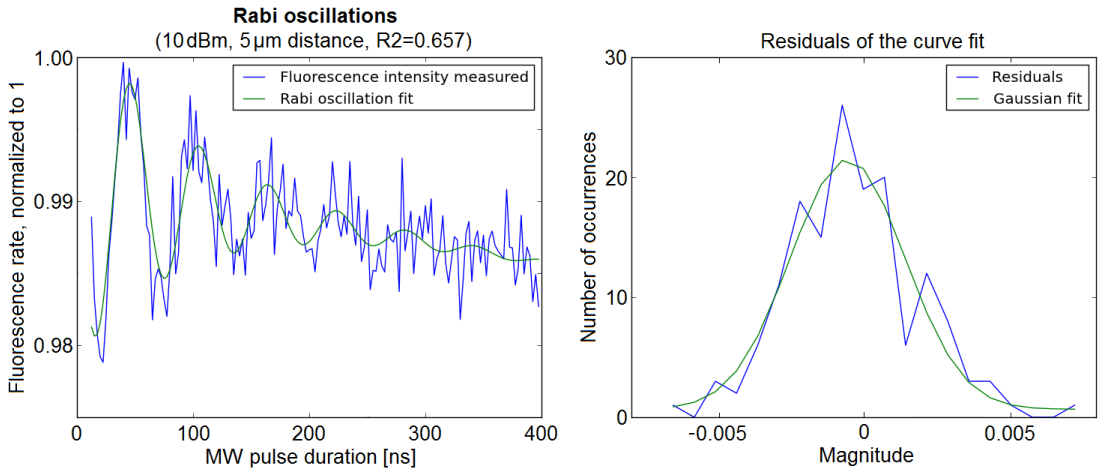

Figure 6.6: Rabi oscillations observed on in an ensemble NV diamond sample at 20 dBm.

Inside the loop the magnetic field is predicted to be almost perpendicular to the diamond surface, except for the area, where the center conductor enters the loop. A radial line was chosen in direction of the CPW. This was decided to ensure that the observed effect originates from a current through the wire. If the magnetic field originated from the CPW on the sample holder the observed Rabi frequency should be constant. Measurements show that the Rabi frequency increases towards the edge of the loop. Unfortunately the quality of the data didn't allow to determine the dependency of the magnetic field strength from the distance to the loop, but at least the data shows no conflict with the assumption of an $1/r$ dependency.

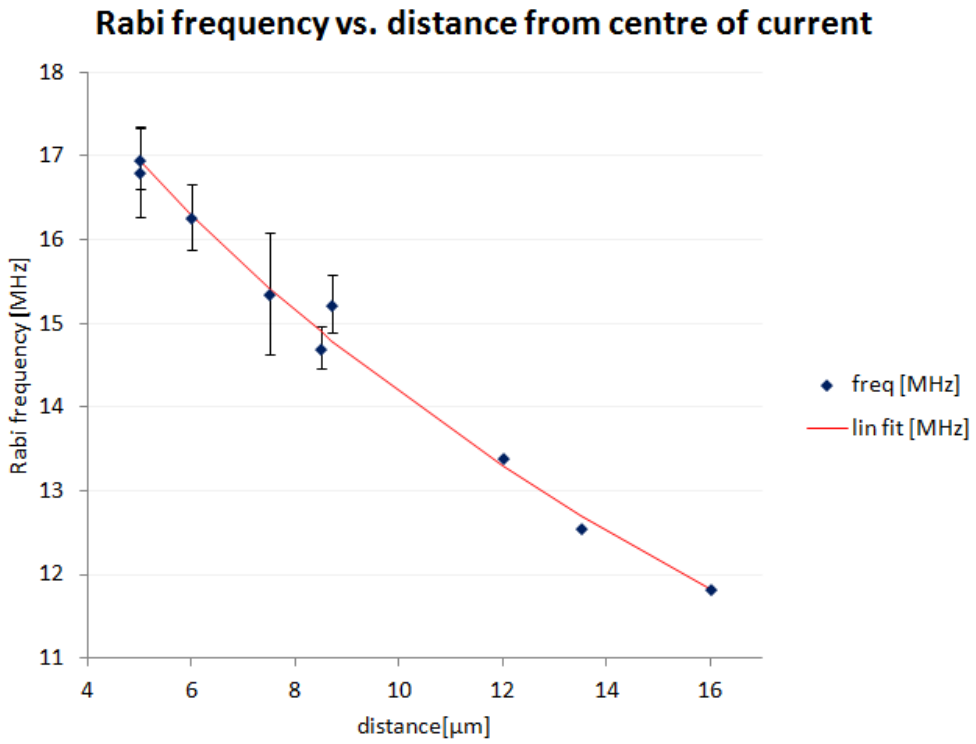

Figure 6.7: Rabi frequencies at distances of 5 to 16 µm to the inner edge of the m loop at 20 dBm microwave power. The 1/r proportional fit, which approximates the data better than a linear fit, allows estimation of the center of the current distribution about 20 µm from the edge into the conductor.

6.3 Performance evaluation of the MW micro-structures

There are several differences between the effect of the use of a wire upon the diamond sample and a metallic micro structure.

6.3.1 Qualitative differences

Advantages of the micro structure[1]:

- The focal spot of the confocal microscope can be placed much closer to the inner edge of the loop compared to the edge of the wire by a factor of approximately 14. This means the horizontal distance between the center of the current distribution and the NV is reduced by a factor between 8 to 14[2].

[1] This is just regarding the structures including a short circuit loop and a gold conductor of 1 × 40 µm forming that loop.

[2] Depending on the location in the construction the maximum current is on the inner or outer side of the

- Since the micro-structures are fabricated on the diamond surface with µm precision, the field distribution around the structure can be simulated (up to an unknown attenuation constant[3]). Contrary to the simple wire antenna, the micro-structures don't move and provide reproducible experimental conditions.

- The structures provides a visual reference to pinpoint the location of an NV, allowing to find it again after moving the sample. This is possible because the size of the Airy disk of an NV is on the order of the accuracy of the structure and distances between NVs are generally much larger in a single NV diamond[4].

- A loop covers the full range of azimuthal angles of microwave magnetic field directions regarding NV directions, whereas only an angle of 45° is possible for the wire plus an uncertainty as the wire is slightly bent. The polar angle has to be controlled via depth and distance of the NV regarding the source of current.

- The contrast of the ODMR spectrum increased. This effect varied very much and could not be generally quantified. The best achieved contrast was about 8.7% which is about ten times the contrast measured with a sample utilizing a wire transmission line above it. The maximum theoretically achievable contrast is about 30 % [Chi07]. The achieved contrast is even more surprising as the sample was an ensemble NV sample, in which the NVs should have slightly varying transition energies due to local variations of the NV surrounding (the field of other spins, lattice strain). A possible explanation might be the high power broadening, which causes NVs in a wider range of spin transition energies to be affected by the MW field. The higher the number of NVs participating in the spin transition with regards to the total number of NVs, the more NVs are found in the dark state, which is responsible for the dip in the ODMR spectrum.

Advantages of the wire set-up:

- A large area can be used to search for NVs. In contrast the micro structure samples just offer the area within the loop and an area around the loop (see 5.1).

loop. The current is on the inside edge of the loop, when no ground conductor is present or when the currents from both ground conductor sides and the inducted current by the center conductor cancel each other out, which is practically the case for one single spot. It is possible to reduce the difference of current maximum on the inside and outside by (considering heat dissipation and manufacturing issues) decreasing the width of the conductor to 10 µm resulting in a distance of 12 µm between current distribution center

[3] The power at the bonds is possible to be estimated when comparing it to a CPW of the same configuration, but the amount of power reflected at the bonds and the tapering is most likely impossible to estimate, probably this could be done by analysing the phase shifts caused by the reflection

[4] The density of NVs found within a cube of 20 µm edge length varies between 70 and none at all. Further the type IIa diamond samples vary in NV content too. There an average distance is hard to estimate. The sample used for the final experiments had distances over 20 µm for any two NVs. Exact numbers are not available as the mechanical screws made precise movements a inconvenient challenge.

- The amount of power the wire can be subjected to is much greater than that of the loop[5]. Nevertheless the loop can withstand great power compared to its cross section, which is due to the unsurpassed heat conductivity of diamond.

The effective magnetic field strength an NV is subjected to and the power needed to achieve that field strength are rather difficult to pin down precisely. The most evident indicator of the magnetic field strength are Rabi oscillations. Due to the limited timing resolution of our set-up, the Rabi frequencies we can still resolve are limited by Nyquist's rule. In order to evaluate the field strength very close to the structure, where it is highest, we exploit the power broadening of the resonance lines (see section 6.1.2).

6.3.2 Achievable Rabi frequencies

The Rabi frequency is directly proportional to the field strength of the MW field. The fastest oscillation observed was about 17 ± 0.4 MHz at a distance of 6 µm from the inner edge of the loop and a MW power of 20 dBm. The oscillation signal was approximated using a 6 parameter fit curve representing a damped oscillation (described by frequency, phase, amplitude and decay), which is shifted by something assumed to be a linear function. The reason for that shift is unknown to me, but as all measurements allowing a curve fit at all were 'successfully' fitted that way, I assume the model to be appropriate (see figure 6.6). The reason the ensemble NV diamond sample[6] was used instead of a single NV sample was, that it was almost impossible to find an NV in a position close to the edge of the loop conductor, as their density was so low.

Compared to measurements performed using the wire construction, the achieved frequency is about 70% higher. The highest frequencies observed using a wire construction[7] were about 10 MHz at a microwave power of 42 dBm at the input port of the sample holder. The distance to the wire was about 100 µm from the wire edge, which is about 115 µm from the center of the current distribution in the conductor. In contrast, the measurement on the micro-structure sample presented above was taken at 20 dBm[8]. Compared to the wire structure the power is about a factor of 150 smaller. This results in an increase in the ratio of effect per utilized power of about 250.

The distance of the focal spot from the edge of the micro structure was about 5 µm resulting in a distance of 25 µm to the center of the current distribution inside the conductor[9]. Fitting the data to the expected $1/r$ decay of the magnetic field inside a current loop results in a fit curve showing a pole at 20.4 µm inside the conductor, which matches the expectations (see figure 6.7). Unfortunately, the quality, of the fit is rather poor[10],

[5] It was observed that the immersion oil between the diamond and microscope objective started to scatter or fluorescence heavily, when the power was risen to about +25 dBm

[6] Sample BS3-3b, see figure 5.21

[7] Information provided by Stefan Putz

[8] At a generator power of 10 dBm and a -30 dB attenuator (instead of -10 dB)

[9] Evaluating the current distribution inside the loop conductor showed that the maximum current density is to be found on the edges and changes the preferred edge along the loop

[10] The R2 statistic is at least better for the $1/r$ fit than for a linear fit or $1/r^2$ fit.

because the change of the Rabi frequency along the measurement range was very low.

6.3.3 Comparing power broadening effects

A more accurate way to compare the relation between power and Rabi frequency between the two setups is possible by comparing the line width of the ODMR spectra. The dips in the spectrum can be approximated by a Lorentzian shape.

As the Rabi oscillation is proportional to the microwave field strength, the formula 6.8 will be satisfied by the measured line widths except for a constant factor. Due to the low saturation of the NVs in an ensemble NV diamond sample, the saturation term will not contribute[11]. The equation will therefore simplify to $\Delta\nu = \sqrt{\frac{\Gamma_c^\infty}{\Gamma_p^\infty}}\frac{\Omega_R}{2\pi}$. The Rabi frequency is directly proportional to the magnetic field and the dipole matrix element μ_{12}. With both setups the magnetic fields (moving the focal spot along the ring changes the azimuthal angle of the magnetic field of the microwave, additionally some static fields were used to have a small Zeeman effect separating the lines of individual NV directions) were chosen to have a maximum distinctness of the dip in the ODMR spectrum so μ_{12} is surely not equal for both experiments but likely to be at the same order of magnitude. The magnetic field of the microwave created by the loop resp. wire itself depends directly on the amplitude of the incoming microwave signal. The ratio between incoming amplitude and applied magnetic field is described by the inverse dependence on the distance from the center of the current distribution in the conductor and the ability of the setup to transfer the incoming field to the NV.

In the limit of low saturation the line width rises linearly with the MW power. A linear regression was performed with two data sets, one with the wire setup and one with the micro structure, recorded at comparable conditions. The quotient of the gradients was determined to be 170, which means an observed spot on the sample with a wire construction is subjected to a field strength which is -22.3 dB smaller than when using a micro-structure at the same distance. The uncertainties of the power broadening fits and the linear regressions are negligibly small compared to the uncertainty of the distance from the wire resp. loop conductor edge, which contributes as an inversely proportional factor to both magnetic field distributions. For both setups a small uncertainty is caused

[11] For a single NV the term including the saturation at laser powers high above the saturation power (which is defined to be at 50% saturation) equals the term including the Rabi frequency at $\Omega_R^2 \approx 8 \cdot 10^7 \cdot 5 \cdot 10^6$. Therefore approximately $4 \cdot 10^7 = \Omega_R = \mu_B g \Delta m_s B_0/\hbar = 9.274 \cdot 10^{-24} \cdot 2 \cdot B_0/1.054 \cdot 10^{-34} = 1.750 \cdot 10^{11} B_0$, which results in a field of $B_0 = 2.273 \cdot 10^{-4}$ T$\approx$ 2.3 G in 10 µm distance to the inner edge of the loop if the magnetic field is perfectly aligned to the NV axis. That field strength may be achieved using at least 0.25 mW if all radiation energy is channelled into the current in the loop. As it is most likely that at least several mW reach the loop, the term involving saturation will not contribute substantially. Further the assumption of highly saturated NVs is not valid for the ensemble NV diamond sample in the experiment. The laser of the experimental setup currently applies about 1 mW to the diamond sample and therefore does hardly reach 80% saturation with even a single NV. As one will find about 10^6 NVs in the confocal volume the relative saturation power will be close to 0.

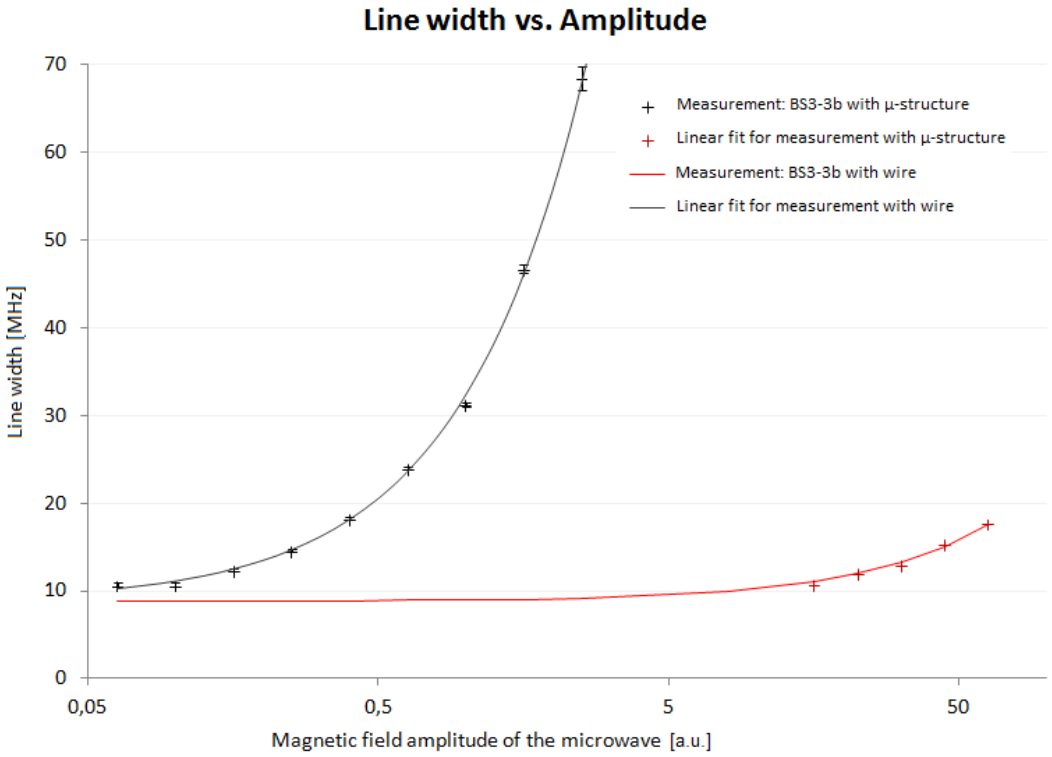

Figure 6.8: The line broadening recorded at powers of -28 to 8 dBm with the sample BS3-3b with micro structure was compared to old data of the same sample with the wire attached. The linear fits differ in their gradient by a factor of about 170

by the hysteresis of the translation micrometre screws and a large one results from the possible movement of the wire when the sample is shifted in front of the microscope objective. Further the distances from the wire are unknown, because the data was recorded prior to this thesis project.

7 Conclusion and outlook

The main aim of this thesis was to enhance the coherent control of the electron spin states of nitrogen vacancy (NV) defect centers in diamond. This was made possible by designing, simulating and manufacturing a microwave micro-structure on top of the diamond samples in use. This process is covered in chapter 5. The success of this endeavor was evaluated with coherent spin manipulation experiments, which are presented in chapter 6. The technique utilized for these experiments is called optically detected magnetic resonance (ODMR) which is reviewed in chapter 2. Chapter 3 provides the necessary information about the NVs and how to detect it. The device that allows observation of NVs is a confocal microscope, which is the main component of the experimental set-up, described in chapter 4.

One of the major achievements of this thesis project is that the device created enables one to measure the relative position between NVs and a reference point. This allows one to uniquely identify and reuse specific NVs after, e.g., remounting the sample. The fact that the micro-structure has a well-defined geometry and a fixed position also allows one to calculate the exact shape of the electromagnetic field in its surroundings and predict its effects on a specific single NV.

A further opportunity is to control the stationary field strength by coupling a DC current into the microwave guide. By creating independently connected orthogonal strips next to the short circuit loop it could be possible to change the magnetic field's direction as well, but the polar angle (the deviation from the z-direction) would then still be dependent on the depth. Utilizing the other side of the diamond could probably give full control of the field, but this would require a second, different fabrication procedure; making transversal shifts of the structures towards each other might be difficult to prevent. The full control of the static magnetic field would give the opportunity to manipulate the Zeemann shift of an individual NV in order to tune its spin transition energy to match the microwave frequency. Thus single NVs may be selected for qubit transformations. Nano-diamonds lend themselves more easily to investigations of the directional magnetic field dependence, as they can for example be applied to a microscope slide and the electronic structures can be enlarged by several orders of magnitude, reducing the problem of accuracy.

It would be equally interesting to create multiple individually accessible short circuit loops within one diamond sample. Implanted NVs could form an array of qubits and the scalability of such systems could be tested. This would not allow multi-qubit operations by itself, as the NVs do not become entangled by such a device, but this could probably

be achieved by photon entanglement of the fluorescence using optical means. An idea I would like to pursue is using two layers of arrays of microwave guides, each with several independent lines holding several short-circuit loops. The loops superimposed over each other are driven with different frequencies, such that their middle frequency – the microwaves that interfere to cause the beating should be beyond any NV resonances – is resonant with the NV. Such an access via two guides permits the amount of individually accessible NVs to rise quadratically relative to the number of microwave conductors.

Another achievement aimed for in this thesis is that it be possible to reduce the power needed for an ODMR recording, featuring an optimal ratio between low noise and low power broadening, by about 18 dB, or approximately a factor of a 100th. This is essential to NV experiments applying microwaves within a cryostat, where any additional creation of warmth has to be avoided.

8 Appendix

8.1 History of the field

The subject deal with in this thesis is primarily founded in two separate branches of physics, that were only recently – around the millennium – combined to promote development of the implementation of the quantum system discussed in this thesis. One of these is quantum information processing, particularly quantum computation, which was a rather theoretical field at the time of its invention. The other one is the study of crystallographic defects, which started out as a subject of experimental physics. This research area yielded the discovery and analysis of the nitrogen vacancy defect center, which became of great interest to quantum physicists as it forms a qubit.

Discovery and analysis of the NV

- 1862: W. A. Miller discover that diamonds show different absorption spectra [Mil62].
- 1934: Robertson, Fox and Martin divide diamonds into two main types depending on the spectra. These mainly differ in the ultraviolet cut-off frequency and infra-red absorption bands [RFM34].
- 1959: Kaiser and Bond find nitrogen to be the main impurity responsible for the characteristics of the two types of diamonds [KB59].
- 1965: Dyer and du Preez show that the 1.95 eV absorption line can be created by annealing radiation damage in nitrogen rich diamonds [DP65].
- 1971: Clark and Norris use polarized luminescence measurements to determine that the structure of the defect may be trigonal, monoclinic I or rhombic I [CN71].
- 1972: Messmer and Watkins publish a theoretical analysis of the electronic structure of deep-level semiconductor defects using linear combinations of atomic orbitals. The nitrogen donor in diamond is treated as an example. Their simulations show an energy state between the valence and conduction band, which they identify as the nitrogen deep donor[1] state [MW70].
- 1976: Davies and Hamer determine the structure of the 1.945 eV defect (often called W15) to be trigonal. The zero phonon line is split under pressure and corresponds

[1] A deep donor can be an electron source in a semi-conductor, but is defined to need energies greater than supplied by room temperature to donate it - in contrast to shallow donors used in semi-conductors.

to a transition between the states ^{1}A and E. They conclude that the spectrum of the vibrational side band is compatible with the model of a nitrogen vacancy center [Dav76].

- 1978: Loubser and Wyk detect an ESR signal of an NV spin, but only should the sample be optically excited simultaneously. They postulate an additional $^3A_2$ state to be responsible for this effect. They also propose an explanation for the spin one of the NV. If the NV captured an electron from a surrounding nitrogen donor, it would possess two unpaired electrons [LW78].

- 1984: Harley et al. report that their spectral hole burning measurements exhibit a splitting of the excited state [HHM84].

- 1987: Reddy, Manson and Krausz claim to have determined the ground state of the NV to be ^{3}A, as their spectral hole burning measurement showed the same 2.88 GHz as the ESR measurements. Additional features observed led to the conclusion that instead of an excited ^{1}E there is actually a triplet ^{3}E state present [RMK87].

- 1997: Gruber at al. observe the fluorescence of a single NV and perform an ODMR scan upon it, therefore rendering a single spin visible [GDT+97].

- 2003: Nizovtsev et al. analyzes photo-kinetics of the NV under ODMR to obtain transition rates between states [NKJ+03].

- 2006: Manson et al. propose an intermediate state ^{1}E above $^1A_1$ to explain why the spin polarization under optical illumination is less than perfect [MHS06].

Applications of the NV

- 1999: Draebenstedt et al. mention the possible use in quantum computation [DFT+99].

- 2000: Kurtsiefer et al. observe photon anti-bunching from an NV compatible only with a single NV. That makes it a solid-state single-photon source [KMZW00].

- 2007: Fu et al. characterize the properties of nano-diamonds as bio-markers [FLC+07].

- 2008: Degen describes a scanning device where a single spin is used as an ultra-sensitive, nano-scale magnetic field sensor [Deg08].

Quantum information processing until 2001

- 1969 (1983 pub.): Stephen Wiesner proposed "quantum money" which designates a quantum state which is impossible to be copied due to lack of knowledge of its basis states. The underlying conjugate coding theorem is one of the first attempts to practically utilize the properties of quantum systems for information processing [Wie83].

- 1973: Holevo publishes his theorem about the information capacity of a quantum system [Hol73].
- 1979: Paul Benioff discusses the representation of a Turing-machine with quantum mechanical Hamiltonians, but that model does not utilize the advantages of particular quantum mechanical processes [Ben80].
- 1981: Richard P. Feynman elaborates on simulation of physics using quantum computers, which would be impossible on classical devices [Fey82].
- 1985: D. Deutsch presents a general, fully quantum mechanical model for computation and explores the advantages over a classical computer [Deu85].
- 1992: D. Deutsch and R. Jozsa present the first algorithm to fully exploit the advantage of quantum parallelism, though the problem solved was rather artificial [DJ92].
- 1994: P. Shor finds an algorithm for factorization in polynomial time, gaining high public attention as it implies breaking of RSA encryptions [Sho94].
- 1995: Barenco et al. show that a set of all one-qubit gates and one two-qubit gate[2] exclusive or gate suffice to establish universal means to fully manipulate arbitrarily many qubits [BBC+95].
- 1995: P. Shor discovers that quantum errors caused by decoherence can be corrected for other means than the categorically impossible creation of redundant copies [Sho95].
- 1995: Cirac and Zoller propose a quantum computer using two qubits in form of two degrees of freedom of an ultra-cold trapped ion interacting via laser light [CZ95].
- 1995: Monroe et al. realize a controlled NOT gate using a trapped ion [MMK+95].
- 1996: The first algorithms for quantum system simulation are proposed [Wie96] [Zal98].
- 1997: L. Grover creates an algorithm for searching databases within the square root of the time needed for the same operation on a classical system [Gro97].
- 1998: B. E. Kane proposes the realization of qubits in form of dopant atoms in silicon. This therefore is the first specific solid state implementation of a quantum computer [Kan98].
- 1998: Jones and Mosca solve Deutsch's problem using a two qubit quantum computer by means of nuclear magnetic resonance [JM98].

[2] They discussed the exclusive OR gate in this paper, but this is not the only option; e.g. the CNOT gate is also possible

- 1999: Voila, Lloyd and Knill show how to achieve noise tolerant universal quantum control on the full state space of the system based on purely unitary open-loop manipulations, which do not require any extra space resources [VLK99].
- 2001: Knill et al propose a scheme for performing quantum operations using linear optics exclusively [KLM+01].

Spin manipulation and quantum-computation with NVs

- 2001: Wrachtrup et al. suggest the use of C-13 nuclear spins near an NV for quantum computation [WKN01].
- 2004: Jelezko et al. observe Rabi oscillations and Hahn echo of a single electron spin and the coupling to ^{14}N nuclear spin [JGP+04a]. Further they implement a conditional two qubit gate, a so-called CROT. The qubits were the NV electronic spin and a neighbouring ^{13}C spin [JGP+04b].
- 2006: Childress et al. show that electronic spins can be used to manipulate nuclear spins of nearby ^{13}C atoms [CGDT+06].
- 2008: Hanson et al. show that both the internal interactions of the bath and the coupling between the central spin and the bath can be tuned in situ, specifically changing an external magnetic field acting on the sample to prolong the spin echoes lifetime [HDF+08].
- 2010: Lange et al. show that it is possible to prolong the spin coherence beyond the bath correlation time, by decoupling the spin from the bath. This universal mechanism is called double axis dynamical decoupling using pulses [LWR+10].
- 2012: Sar et al. realize amethod to run the decoupling process synchronously to a progressing conditional quantum gate [SWB+12].
- 2012: Grotz et al. allow the charge state of the NV to be controlled by electrolytic gate electrode [GHD+12].

8.2 Basics of quantum mechanics

This section will summarize the basic concepts necessary to understand the behaviour of quantum states. It is entirely based on the introductory chapter of the book "Mathematical Methods in Quantum Mechanics"[Tes09] except of statements denoted to be from a different source.

8.2.1 Quantum states

The existence of superposition states in quantum physics, systems that consist of a combination of multiple mutually exclusive values of physical properties in a single state, implies that – according to the Copenhagen interpretation of quantum

mechanics – such states can not be entities of reality. Instead quantum states are formal objects [AP01], whose mathematical structure is going to be discussed in this section.

In classical physics the states describing a macroscopic system reside in an euclidean phase space, the $\mathbb{R}^{2n}$ with n position and n momentum coordinates. In contrast, the state of a quantum system is always described by a vector in Hilbert space $\mathfrak{H}$.

The space of quantum states is spanned by a set of basis vectors $\{\phi_i\}_{i=1}^{dim(\mathfrak{H})}$. A quantum state is then defined as linear combination of basis states with complex coefficients c_i:

$$\psi = \sum_{i=1}^{dim(\mathfrak{H})} c_i \phi_i \tag{8.1}$$

The dirac (or Bra-Ket) notation denotes quantum states $|\psi\rangle$ and their pendants in dual space $\langle\psi|$ and was introduced following the notation of the scalar product of vectors in Hilbert space.

For any pair of quantum state vectors $\psi, \phi \in \mathfrak{H}$ a positive definite sesquilinear form, a map $\langle . \,|\, . \rangle : \mathfrak{H} \times \mathfrak{H} \to \mathbb{C}$ is defined, which is called scalar product. A very common quantum states is the stationary wave function in $\mathbb{R}^3$ for which the scalar product takes the form

$$\langle \psi \,|\, \phi \rangle = \int_{\mathbb{R}^3} \psi(\vec{x})^\dagger \phi(\vec{x}) d^3x \tag{8.2}$$

Another example would be the scalar product of states described by a combination of a discrete number of levels, like it is the case for a qubit:

$$\langle \psi \,|\, \phi \rangle = \sum_{j \in \mathbb{N}} \psi_j^\dagger \phi_j \tag{8.3}$$

The scalar product of a state with itself allows to define a norm

$$\|\psi\| = \sqrt{\langle \psi \,|\, \psi \rangle} \tag{8.4}$$

A vector ψ is called normalized when

$$\|\psi\| = 1 \tag{8.5}$$

Two vectors are called orthogonal when

$$\langle \phi \,|\, \psi \rangle = 0 \tag{8.6}$$

The projection of a state onto another is given by

$$\psi_{||} = \langle \phi \,|\, \psi \rangle \, \phi \tag{8.7}$$

Any quantum state vector can thus be written as sum of its projection onto the basis state vectors $\{\phi_i\}_{i=1}^{dim(\mathfrak{H})}$:

$$\psi = \sum_{i=0}^{dim(\mathfrak{H})} \langle \phi_i \,|\, \psi \rangle \, \phi_i \tag{8.8}$$

This may be rewritten by defining a projection operator P_i onto each basis vector:

$$P_i = |\phi_i\rangle \langle \phi_i| \tag{8.9}$$

$$\psi = \sum_{i=0}^{dim(\mathfrak{H})} P_i \, |\psi_i\rangle \tag{8.10}$$

Using the Gram-Schmid process every finite set $\{\phi_i\}$ of linear independent vectors can be transformed into a orthonormal set. If the set spans the complete vector space it is called an orthonormal base (ONB).

8.2.2 Measurement

A measurement of a quantum system is essentially different from a measurement of a macroscopic system. A macroscopic physical system is in one state at a time, which means it has one value for each observable property. In ideal measurements of a repeatedly identically prepared macroscopic system, the result is always the same with 100 % probability and exactly reflects the state of the system in the moment before measurement.

General quantum states are superpositions of states measurable and as such in generally unequal to the states actually measured by macroscopic devices. This means the measurement probabilistically forces the superposition state into one of the measured basis states, which is called the collapse of the quantum state [Fox06]. This process equals a projection operation P_i onto the basis vector ϕ_i – an idempotent operation. Repeated measurement on the same state will thus always return the same result. If the state basis vectors form an ONB these states are projected exclusively onto themselves upon measurement. The measurement can be described by a hermitian linear operator called observable $\hat{A}$ and states are then eigenstates of this operator. The eigenvalue equation for a linear transformation $\hat{A}$ is

$$\hat{A}\phi_i = a_i\phi_i \tag{8.11}$$

The linear operator $\hat{A}$ needs to be hermitian –

$$\hat{A}^\dagger = \hat{A} \tag{8.12}$$

– to have only real numbers as eigenvalues a_i. For all other states except the eigenstates the measurement statistically distributes the measured values. The probabilities p_i for measuring a particular eigenvalue are determined by the Born rule:

$$p_i = |\langle \phi_i | \psi \rangle|^2 = \langle \phi_i | \psi \rangle \langle \phi_i | \psi \rangle = \langle \psi | P_i | \psi \rangle \tag{8.13}$$

This also gives reason to the postulated normalization of quantum states. A state inevitably needs to be in one of its basis states in case it is measured, since $|\psi\rangle = \sum \langle \phi_i | \psi \rangle |\phi_i\rangle = \sum c_i |\phi_i\rangle$. This means the coefficients get a physical meaning with their absolute squares being the probabilities of finding a arbitrary state ψ in that specific eigenstate ϕ_i:

$$|c_i|^2 = p_i \tag{8.14}$$

with

$$\sum_i |c_i|^2 = \sum_i p_i = 1 \tag{8.15}$$

The expectation value is a mean over infinite measurements of identically prepared states:

$$\left\langle \hat{A} \right\rangle_\psi = \sum_{i=1}^{dim(\mathfrak{H})} p_i a_i = \left\langle \psi \middle| \sum_{i=1}^{dim(\mathfrak{H})} a_i P_i \middle| \psi \right\rangle = \sum_{i=1}^{dim(\mathfrak{H})} a_i |\langle \phi_i | \psi \rangle|^2 \tag{8.16}$$

As the observable $\hat{A}$ is a self-adjoint operator following expressions are equal:

$$\left\langle \hat{A} \right\rangle_\psi = \left\langle A^\dagger \psi \middle| \phi \right\rangle = \langle \psi | A\phi \rangle = \langle \psi | A | \psi \rangle \tag{8.17}$$

8.2.3 Time evolution of states

In quantum mechanics the dynamics of all states are described by the Schrödinger-equation

$$i\hbar \frac{\partial}{\partial t} \psi(t) = \hat{H} \psi(t) \tag{8.18}$$

A time evolution operator $U(t_1, t_0)$ that acts in the following manner

$$|\psi(t)\rangle = U(\hat{t}, t_0) |\psi(t_0)\rangle \tag{8.19}$$

needs to obey the Schrödinger equation too[3]

$$i\hbar \frac{\partial}{\partial t} U(t, t_0) = \hat{H}(t) U(t, t_0) \tag{8.20}$$

In the approximation for arbitrarily small changes δt the role of the Hamiltonian $\hat{H}$ as generator of the time evolution becomes visible:

[3] Easily seen when inserting both states, at t_0 and t_1 into the Schrödinger equation.

$$U(\delta t + t, t_0) = (1 - \frac{i}{\hbar}\hat{H}(t)\delta t)U(t, t_0) + O(\delta t^2) \tag{8.21}$$

From that the time evolution can be calculated

$$U(t, t_0) = e^{-\frac{i}{\hbar}\int_{t_0}^{t}\hat{H}(\tau)d\tau} \tag{8.22}$$

Because the exponential function of a self-adjoint operator is always unitary $U$is a unitary operator. A bijective linear operator U is called unitary if it preserves the scalar product

$$\langle U\phi \,|\, U\psi\rangle_2 = \langle \phi \,|\, \psi\rangle_1 \,, \quad \phi, \psi \in \mathfrak{H}_1 \tag{8.23}$$

and thus the norm of a state

$$\|U\psi\|_2 = \|\psi\|_1 \tag{8.24}$$

This can easily be shown

$$\|U\psi\|^2 = \langle U\psi \,|\, U\psi\rangle = \left\langle \psi \,\middle|\, U^\dagger U\psi \right\rangle = \langle \psi \,|\, 1\psi\rangle = \|\psi\|^2 \tag{8.25}$$

From this one can also see that

$$U^\dagger = U^{-1} \tag{8.26}$$

This means transformations on a quantum state performed by U can be reversed by $U^\dagger$. Due to the generation of U the sequential application of this transformation results in $U(t_2, t_1)U(t_1, t_0) = U(t_2, t_0)$. Further $U(t_1, t_0) = U^\dagger(t_0, t_1)$ and $U(t_0, t_0) = 1$. These results are essential for the understanding of quantum gates.

8.2.4 Entanglement

A system that is a collection of several quantum states residing in n separate Hilbert spaces $\mathfrak{H}_i$ can be described by a vector in a combined Hilbert space

$$\mathfrak{H} = \bigoplus_{j=1}^{n} \mathfrak{H}_i \tag{8.27}$$

with its elements being tuples $(\psi_1, \psi_2, ..., \psi_n) \in \mathfrak{H}$. The scalar product between the states $\phi, \psi \in \mathfrak{H}$ is preserved when quantum systems are described as one state

$$\left\langle \sum_{i=1}^{dim(\mathfrak{H})} \phi_i \,\middle|\, \sum_{i=1}^{dim(\mathfrak{H})} \psi_i \right\rangle = \sum_{i=1}^{dim(\mathfrak{H})} \langle \phi_i \,|\, \psi_i\rangle_i \tag{8.28}$$

The dimension of the vector space $\mathfrak{H}$ is given as

$$dim(\mathfrak{H}) = dim(\bigoplus_{j=1}^{n} \mathfrak{H}_j) = \sum_{j=1}^{n} dim(\mathfrak{H}_j) \tag{8.29}$$

If $\{e_i\}_j$ is a set of basis vectors of $\mathfrak{H}_j$ (with $0 < i \leq dim(\mathfrak{H}_j)$), the basis vectors of the combined Hilbert space $\mathfrak{H}$ is given by:

$$\{(e_{11}, 0, ...), (e_{21}, 0, ...), ..., (0, e_{12}, ...), (0, e_{22}, ...), ...\} \tag{8.30}$$

This comprises not the complete number of combinations of basis vectors for forming tuples. When the Hilbert spaces $\mathfrak{H}_j$ are defined upon the same scalar field, this can be achieved using the Cartesian product $(\cdot \times \cdot)$ of vector spaces. This space consists of redundant states due to the equivalence relations of tensor products. The quotient space created by these relations is thus removed from it such that the tensor product space remains:

$$\mathfrak{H} = \bigotimes_{j=1}^{n} \mathfrak{H}_j \tag{8.31}$$

$$dim(\mathfrak{H}) = \prod_{j=1}^{n} dim(\mathfrak{H}_j) \tag{8.32}$$

In terms of quantum state this means that not only vectors of the form

$$|\Psi\rangle_{ab...} = |\Psi\rangle_a \otimes |\Psi\rangle_b ... = \sum_{i,j,...} a_i |\phi_i\rangle_a \otimes b_j |\phi_j\rangle_b ... \tag{8.33}$$

but also more general states

$$|\Psi\rangle_{ab...} = \sum_{i,j,...} c_{ij...} |\phi_i\rangle_a \otimes |\phi_j\rangle_b ... \tag{8.34}$$

with $c_{ij} \neq a_i b_j$ are allowed. This means not all states are factorizable into a product of independent quantum states. Those non-separable states are called entangled.

To give an example for an entangled state, let's have a look at the singlet state $\frac{1}{\sqrt{2}}(|01\rangle - |10\rangle)$. This common notation omits the symbol for tensor product, places the letters denoting the state in a single ket closure and assumes the states belonging to a subsystem of the quantum state by their order. This state consists of two product states mixed with equal weights. Therefore you have no information whether one system is in state $|1\rangle$ or $|0\rangle$, they are both equally likely. The unknowing about the state of a subsystem of this state is maximal, whereas the information about the overall state is known. This leads to the phenomenon of non-locality. If one subsystem is measured and thereby collapsed into one of the eigenstates, the other subsystem is instantaneously collapsing into the corresponding state. If in one subsystem the state is measured in $|1\rangle$ the other will inevitably be measured in $|0\rangle$ (with an inverse phase). This occurs independently of distance of the chance for interaction.

8.3 Linear combination of atomic orbitals (LCAO)

In order to understand the structure of energy levels an electron of the NV can occupy, theoretical considerations regarding the geometry of the system may be used to derive qualitative results. The electrons, despite being somehow located inside a hole in the crystal lattice instead of simply being surrounding atoms, form molecule orbitals. Molecule orbital theory, introduced by Friedrich Hund and Robert S. Mullikan, supposes electrons not to be assigned to individual bonds, as the complementary valence bond theory assumes, but forming molecular orbitals instead. These can be described mathematically by mixing the wave functions of the solitary atom's orbitals. This is known as the linear combination of atomic orbitals (LCAO), introduced in 1929 by Sir John Lennard-Jones, which is usually practicable for small-sized molecules[4].

The core assumptions for this model's orbitals are the following:

- Molecular orbitals are formed from an overlap, a normalized linear combination of atomic orbitals. The number of molecular orbitals equals the number of atomic orbitals involved.
- Only atomic orbitals of approximately the same energy interact to a significant degree.
- Only atomic orbitals with the same symmetry properties will interact. This means the interacting orbitals must obey the same behaviour regarding geometric operations like mirroring, inversion or rotations. All operations transforming the orbit into an identical (or negative) one are called symmetry operations. They form the allowed algebraic operations on the point group associated with the molecule's/lattice's structure. Thus, studying their group's symmetry properties lets one to derive the energy states qualitatively.[5]
- When two atomic orbitals overlap, they interact in two extreme ways to form two molecular orbitals, a bonding molecular orbital and an anti-bonding molecular orbital. In the case of bonding orbitals, the composing atomic orbitals are in phase, resulting in an electron density distribution with a high density in between the neighboring atoms. Consequently, coulomb forces will draw the atoms together,

[4] The set of coefficients can be quantitatively evaluated using the Hartree-Fock method, which attempts to minimize the system's total energy, but in most cases a qualitative prediction about the molecule's structure fullfils the needs.

[5] I would like to offer an example of how symmetries affect the bonding orbitals: Take a water molecule with z as the principal axis, x connecting the hydrogen atoms and y perpendicular to the molecular plane. An oxygen's p_x changes sign upon mirroring at the yz-plane or rotating around z. The hydrogens' s-orbits, oppositely phased, swap places accordingly. Therefore, they can overlap in all cases; a resulting molecule orbital would be possible. In contrast, a p_y orbital equally overlaps with in-phase and out-of-phase areas, effectively resulting in no overlap, hence no joint molecule orbital. In terms of symmetry, this means one symmetry operation acts differently on the hydrogen's s-orbitals and the oxygen's p_y. It is the mirroring at the xz-plane, that changes the sign for the p_y but not the s-orbitals.

hence the name. The potential energy is also lower than that of the anti-bonding state, which has low electron density in between the composing atoms.

Further, the electrons will occupy the orbitals in a well-known manner:

- Aufbau-principle: Electronic states are filled up from the lowest energy state towards the higher.
- Pauli principle: At maximum, two electrons may occupy the same orbital; they will then have different spins.
- Hund's rule: Orbitals of equal energy are half filled, with spins parallel, before any is filled with a second electron.

With this presupposition, one can proceed to examine the symmetry properties of the NV's geometric structure. With the NV-axis through vacancy and nitrogen the adjacent carbons form a three-fold rotational symmetry around that axis. The symmetry operation causing identity by azimuthal rotation C_n (in Schoenflies notation) is, accordingly, one by $\frac{360^\circ}{n} = 120^\circ$, which makes it a C_3 operation. Additionally, one can mirror the configuration at the vertical mirror planes σ_v through the axis and the neighbouring carbon atoms, which completes the symmetry's designation, C_{3v}.

Mathematically, this is a group formed by 6 elements from 3 conjugacy classes: E, $2C_3$, $3\sigma_v$, with E being the identity (from German: Einheit). This group is one of the 32 point groups known to crystallography. Each has its representations, which are mappings from its group members to individual matrices. A basis representing the geometric features has to be chosen for the representation, e.g., the atoms can be numbered, forming a vector with each atom as an individual entry.[6] This delivers one quadratic matrix with the basis' dimension for every element constituting the group. Of course one can perform similarity transformations ($D_A = S^{-1}AS$) and may attempt to diagonalize the matrix, but generally one will just be able to obtain block form[7]. These blocks satisfy all requirements for a matrix representation of that group (closed, complete sub-groups) on their own, but especially regarding the associated vector components they act on; they cannot cause a mixing with other components. Creation of smaller blocks will conclude by achieving so-called irreducible representations or 'irreps'. It is noteworthy that these irreducible representations retain their trace/character χ under similarity transformations. One might find irreps that show different matrices for the respective group members, but their traces reveal that they are similar; they create the same behaviour upon the objects they act on. Irreps with a unique set of characters are entered into a character table and designated so-called Mullikan symbols. They are associated, as

[6] An example for the geometry dependency: The matrix representing a 180° turn around z is different for a sphere compared to a vector. It is a 3D identity matrix for the sphere, while it is a matrix including a 2D-euler-matrix in the xy-box and the unit in the zz-component for the vector.

[7] A block matrix consists of quadratic blocks of complex numbers along the diagonal surrounded with zeros.

with the vector components, with translation axes, rotations, orbitals or vibronic states sharing that behaviour. Sometimes not as many irreps are found as there are conjugacy classes. Then the basis would not fully describe the point-group structure. For example translational axes as a basis are not sufficient; rotations have to be taken into account too.

A common form of notation for irreducible representations are Mullikan indices. The main letters are:

- A: one-dimensional and symmetric for rotation around the main axis
- B: one-dimensional and asymmetric for rotation around the main axis
- E: two-dimensional
- T: three-dimensional

Sub- and superscripts:

- g / u: symmetric / asymmetric with respect to center inversion
- 1 / 2: symmetric / asymmetric with respect to rotation around off-principal axes
- ' / ": symmetric / asymmetric with respect to horizontal mirroring

A character table consists of a Schoenflies symbol in the upper left corner, denoting the point group of the structure. The conjugacy classes, more specifically the symmetry transformations, form the column's heads, while the rows are labeled with the irreducible representations. The body is filled with the characters of each irreducible representation for each symmetry operation. Two additional columns are common, one showing the principal axes and rotations, one showing the products of axes. Rotations are mostly denoted with an 'R' before the indicating axis and for degenerate (higher dimensional blocks) irreducible tuples of entities are commonly written within parentheses.
Character table for C_{3v}:

C_{3v}	E	$2C_3$	$3\sigma_v$	linear, rotations	quadratic
A_1	1	1	1	z	x^2+y^2,z^2
A_2	1	1	-1	R_z	
E	2	-1	0	(x,y),(R_x, R_y)	(x^2-y^2, xy),(xz, yz)

The energy level diagram for the NV features an ${}^3A_2$ ground state, an ${}^3E$ excited state as well as an ${}^1E$ intermediate state and an ${}^1A_1$ metastable state. The letters before the Mullikan symbols are used to indicate, whether it is a triplet state or a singlet state.

The ${}^1A_1$ does not change under all symmetry operations, so its phase is symmetric along the z-axis. ${}^3A_2$ is also 3-fold symmetric but always with a phase change at each mirror plane.

8.4 Torque of magnetic moment in a magnetic field

The relation $\vec{\tau} = \vec{\mu} \times \vec{B}$ is usually justified by the similarity to the situation with an electric dipole in an electric field. Taking a closer look at its derivation reveals that the situation is much more complicated in the former case due to the additional cross product introduced by the Lorentz force. This derivation is basically adopted from Jackson's classical electrodynamics [Jac98] and has been rewritten to focus explicitly on the torque acting on a magnetic dipole.

Symbols used

t time
$\vec{r}$ position vector
$\vec{v}$ velocity
m mass
$\vec{p}$ impulse
$\vec{j}$ electrical current density
$\vec{I}$ angular moment
$\vec{\mu}$ magnetic moment
$\vec{\tau}$ torque
$\vec{F}$ force
$\vec{B}$ magnetic induction or flux density

Basics on the mechanics of rotations

A rotation can be described by its angular velocity $\vec{\omega}$. The axis and orientation is represented by the direction of that vector, the amount of rotation (the change of angle over time $\frac{d\phi}{dt}$) by its size. The speed $\vec{v}$ of any point following that rotation is proportional to that angular velocity, increasing with the distance from the axis, being a tangential movement, ergo perpendicular to the axis and the position vector $\vec{r}$ at once. As the positioning vector can have an arbitrarily selected origin, all rotational physical quantities are dependent on that origin. Should no origin be stated, the center of the object is assumed to be the origin.

$$\vec{v} = \vec{\omega} \times \vec{r} \tag{8.35}$$

$$\vec{\omega} = \vec{e}_r \times \frac{\vec{v}}{r} \tag{8.36}$$

From that one can see that the dimension of ω is $\frac{(rad)}{s}$, as all spacial dimensions cance leach other out.

The rotations equivalent for the momentum $\vec{p} = m\vec{v}$ (with m as mass) for a point-like object is the angular momentum $\vec{L}$. It again reflects the axis of rotation and the amount or rotation but also includes the mass:

$$\vec{L} = \vec{r} \times \vec{p}. \tag{8.37}$$

If the mass is spatially distributed, which is probable for an expanded rigid body, the mass is reflected by the moment of inertia Θ, represented through a 3×3 matrix. Its components are defined as $\Theta_{ij} = \int_V \rho(\vec{r})(r_l^2 \delta_{ij} - r_i r_j)\ d^3r$. Θ is symmetrical and can be diagonalized to hold only the moments along the principal axes in the representing matrix. $\vec{L} = \vec{r} \times \vec{p} = \vec{r} \times \Theta\vec{v} = \Theta\ \vec{r} \times \vec{v}$, which is allowed, since Θ is symmetrical and the operator $\times$ fully anti-symmetrical and thus they commute.

$$\vec{L} = \Theta\vec{\omega} \tag{8.38}$$

The torque τ, also called moment of force, is the equivalent of the force F:

$$\vec{F} = \frac{d\vec{p}}{dt} = m\frac{d\vec{v}}{dt}, \tag{8.39}$$

$$\vec{\tau} = \frac{d\vec{L}}{dt} = \Theta\frac{d\vec{\omega}}{dt}. \tag{8.40}$$

We can further expand this: $\frac{d\vec{L}}{dt} = \vec{r} \times \frac{d\vec{p}}{dt} + \frac{d\vec{r}}{dt} \times \vec{p} = r \times m\frac{d\vec{v}}{dt} + \vec{v} \times m\vec{v}$, with the second term always being 0; thus,

$$\vec{\tau} = \vec{r} \times \vec{F}. \tag{8.41}$$

Precession is the name of the phenomenon of a rotating object constantly changing its angular velocity's direction. There can be two reasons for that. The object's symmetry axis, more precisely the three principal axes of the momentum of inertia, are misaligned to the axis of rotation. Another possibility is an external force applied elsewhere than at the center of mass. This results in a torque changing the angular momentum perpendicular to the force's direction: $\dot{\vec{L}} \perp \vec{F}$.

Nutation occurs when the axis of rotation $\vec{\omega}$ is itself rotating around the axis of angular momentum $\vec{L}$. If an impulse or torque tilts the angular momentum off the principal axes of the moment of inertia $\Theta_i\vec{e}_i$, with $i = x, y, z$, the rotation axis will generally not follow, but start rotating around the axis of angular momentum instead. The angular momentum is fixed in space if no external torque is applied, as it is a conserved quantity. Thus, the principal axis of the object rotates around the angular momentum as well. Nutation is not possible for electrons in either classical or quantum-mechanical representation, as there is no distinguished principal axis for a spherical symmetrical object.

Derivation of the torque proposition

The well-known definition of the angular momentum is $\vec{I} = \vec{r} \times \vec{p}$, with $\vec{p} = m\vec{v}$ being the impulse. Later we will use an analogous expression for electrodynamics involving a spatially distributed current, the magnetic moment:

$$\mu = \frac{1}{2} \int \vec{r} \times \vec{j}(\vec{r}) \, d^3r. \tag{8.42}$$

A torque is commonly defined as:

$$\vec{\tau} = \frac{d\vec{\mu}}{dt} = \underbrace{\frac{d\vec{r}}{dt} \times \vec{p}}_{=0} + \vec{r} \times \frac{d\vec{p}}{dt} = \vec{r} \times \vec{F}. \tag{8.43}$$

Using a distributed current density the torque can be defied as:

$$\vec{\tau} = \int \vec{r}' \times d\vec{F}(\vec{r}'). \tag{8.44}$$

The force applied obeys Ampere's law or a Lorentz force:

$$\vec{F} = \vec{j}(\vec{r}) \times \vec{B}(\vec{r}). \tag{8.45}$$

Using this and the Grassmann identity results in:

$$\begin{aligned} \vec{\tau} &= \int \vec{r}' \times \left[\vec{j}(\vec{r}') \times \vec{B}(\vec{r}') \right] \, d^3r' && (8.46) \\ &= \int \left[\vec{r}' \cdot \vec{B}(\vec{r}') \right] \vec{j}(\vec{r}') \, d^3r' - \int \left[\vec{r}' \cdot \vec{j}(\vec{r}') \right] \vec{B}(\vec{r}') \, d^3r'. && (8.47) \end{aligned}$$

Now, using the following trick, taking into account that $div\vec{j} = 0$ (as $\frac{\partial \rho}{\partial t} = 0$ in magnetostatics):

$$\vec{\nabla}(r^2\vec{j}) = (\vec{\nabla}r^2)\vec{j} + r^2\vec{\nabla}\vec{j} = 2\,\vec{r} \cdot \vec{j}. \tag{8.48}$$

Further, recall the Taylor series for the magnetic field around the origin:

$$\vec{B}(\vec{r}) = \vec{B}(\vec{0}) + (\vec{r} \cdot \vec{\nabla})\vec{B}(\vec{0}) + ... \tag{8.49}$$

Using that trick, the first order of the Taylor approximation only and the divergence theorem (Gauss' law) on the second addend, results in:

$$\begin{aligned} -\int \left[\vec{r}' \cdot \vec{j}(\vec{r}') \right] \vec{B}(\vec{r}') \, d^3r' &= -\frac{1}{2} \int \vec{\nabla} \left[r^2 \cdot \vec{j}(\vec{r}') \right] \vec{B}(\vec{r}') \, d^3r' && (8.50) \\ &= -\frac{1}{2} \vec{B}(\vec{0}) \int \vec{\nabla} \left[r^2 \cdot \vec{j}(\vec{r}') \right] \, d^3r' && (8.51) \\ &= -\frac{1}{2} \vec{B}(\vec{0}) \oint r^2 \cdot \vec{j}(\vec{r}') d\vec{f}' && (8.52) \\ &= 0. && (8.53) \end{aligned}$$

The final term is zero, as one can always find a closed surface around a localized current distribution such that no current enters or leaves the volume. Therefore, only the first addend remains. The next steps will provide a helpful identity:

Let $f(\vec{r})$ and $g(\vec{r})$ be arbitrary scalar functions and $\vec{j}(\vec{r})$ a localized current distribution ($div\vec{j} = 0$); then the following is proposed:

$$\int \left(f(\vec{r}')\vec{j}(\vec{r}')\vec{\nabla}'\vec{g}(\vec{r}') + g(\vec{r}')\vec{j}(\vec{r}')\vec{\nabla}'f(\vec{r}') \right) \, d^3r' = 0. \tag{8.54}$$

Proof: We start with the following term, which is zero, as we can use the divergence theorem (Gauss' law) on it and have localized a current distribution given (argument $\vec{r}'$ and infinite element d^3r' implicit):

$$\int \vec{\nabla}'(f\vec{j}g) = \oint f\vec{j}g = 0. \tag{8.55}$$

Nevertheless, we can calculate the derivation using the product rule:

$$\int \vec{\nabla}'(f\vec{j}g) = \int (\vec{\nabla}'(f\vec{j}))g + \int f\vec{j}\vec{\nabla}'g = \int (\vec{\nabla}'f)\vec{j}g + \int f \underbrace{(\vec{\nabla}'\vec{j})}_{=0} g + \int f\vec{j}\vec{\nabla}'g. \tag{8.56}$$

Thus we find:

$$\int (\vec{\nabla}'f)\vec{j}g = -\int f\vec{j}\vec{\nabla}'g. \tag{8.57}$$

Q.E.D.

Now, $f = x_i'$ and $g = x_l'$ would be the arbitrary components of the position vector:

$$\int (x_i' \underbrace{\vec{j}x_l}_{j_l} + x_l \underbrace{\vec{j}x_i}_{j_i}) \, d^3r'. \tag{8.58}$$

Therefore,

$$\int x_l'j_i' \, d^3r' = \frac{1}{2} \left(\int x_l'j_i' \, d^3r' - \int x_i'j_l' \, d^3r' \right). \tag{8.59}$$

Multiplying this with the l-th component of an arbitrary vector $\vec{B}$ and summing over that index delivers:

$$\sum_l B_l \int x_l'j_i' \, d^3r' = \sum_l \frac{1}{2} B_l \left(\int x_l'j_i' \, d^3r' - \int x_i'j_l' \, d^3r' \right) \tag{8.60}$$

$$= -\frac{1}{2} \left[\vec{B} \times \int \vec{r} \times \vec{j}(\vec{r}') \, d^3r' \right]_i. \tag{8.61}$$

The above equation can easily be verified by calculating explicitly each side for each component; it is basically a Grassmann identity. Now one can exchange r' for r and retrieve:

$$\int \vec{B}\vec{r}j_x \; d^3r' = \frac{1}{2}\int [\vec{B} \times (\vec{r} \times \vec{j})]_x \; d^3r'. \tag{8.62}$$

Resuming calculations with the first addend:

$$\vec{\tau} = \int \left[\vec{r}' \cdot \vec{B}(\vec{r}')\right] \vec{j}(\vec{r}') \; d^3r' = -\vec{B}(\vec{0}) \times \frac{1}{2}\int \vec{r}' \times \vec{j}(\vec{r}') \; d^3r'. \tag{8.63}$$

Using the above definition of the magnetic moment delivers the desired results.

$$\tau = \vec{\mu} \times \vec{B}(\vec{0}) \tag{8.64}$$

8.5 Spin-spin coupling in molecules and defects

Normally, spins use an external field as quantization direction. Nevertheless, it was stated that the dark and bright states of the NV have different energy levels by 2.88 GHz, which are called zero field splitting. This implies that there is an internally manifested axis of quantization for each NV, which themselves can take 4 directions with each 2 orientations. It is quite intentional that the spins will choose the NV-axis as their quantization direction. Any external magnetic field needs to overpower the internal field distortion from spherical geometry, determining the quantization direction, in order to become quantization direction.

The subsequent derivation of the quantization direction for low magnetic fields and the zero field splitting is provided in the form of an excerpt from the textbook "Molekülphysik und Quantenchemie" by Haken and Wolf [HW02]. The Hamiltonian of this system describes the energy of two interacting spins[8]:

[8] For absolute Basics one starts with Maxwell's equations, more precisely Ampere's law: $\nabla \times \vec{B} = \mu_0 \vec{J} + \epsilon_0 \mu_0 \frac{\partial E}{\partial t}$. One may use the vector potential of the electromagnetic field $\vec{B} = \nabla \times \vec{A}$ and, as we are looking at the time-independent solution, may neglect all time derivatives. The resulting term $\nabla \times (\nabla \times \vec{A}) = \mu_0 \vec{J}$ can be reduced using common vector identities delivering a Poisson equation $\nabla^2 \vec{A} = -\mu_0 \vec{J}$, whose solution is well known: $\vec{A}(\vec{r}) = \frac{\mu_0}{4\pi} \int d^3r' \frac{\vec{J}(\vec{r}')}{|\vec{r}-\vec{r}'|}$. For relatively small $\vec{r}'$, one may use the Cartesian multi-pole expansion $\frac{1}{|\vec{r}-\vec{r}'|} = \sum \frac{1}{|r|} + \frac{r_i r_i'}{|r|^3} + ...$ to expand the scalar term (the denominator): $\vec{A}_i(\vec{r}) = \frac{\mu_0}{4\pi}\left(\frac{1}{|r|}\int \vec{J}_i(\vec{r}')d^3r' + \frac{r_j'}{c|r|^3}\int \vec{J}_i(\vec{r}')r_j' d^3r' + ...\right)$. As the current density has no sources, the first integral will be 0. The momentum is defined as $\vec{\mu} = \frac{1}{2}\int \vec{r} \times \vec{J}$. The cross product can be moved to the other side of the equation by a long, purely algebraic process, resulting in $\int J_j r_k = -\epsilon_{jkl}\mu_l$. Using this in the remaining (second) term one obtains: $\vec{A}_i(\vec{r}) = \frac{\mu_0}{4\pi}\frac{\vec{\mu}\times\vec{r}}{|\vec{r}|^3}$. Finally, one may use the definition of the vector potential again for calculating the magnetic flux density of a magnetic dipole: $\vec{B} = \frac{\mu_0}{4\pi}\frac{3\vec{r}(\vec{r}\vec{\mu})-\vec{r}^2\vec{\mu}}{|\vec{r}|^5}$. From that one can write down the dipole-dipole interaction Hamiltonian: $H = -\frac{\mu_0}{4\pi}\left(\frac{3(\vec{\mu}_1\vec{r}_{12})(\vec{\mu}_2\vec{r}_{12})}{r_{12}^5} - \frac{\vec{\mu}_1\vec{\mu}_2}{r_{12}^3}\right)$.

$$H = \frac{\mu_0}{4\pi}\frac{g_e^2\mu_B^2}{\hbar^2}\left(\frac{\hat{\vec{S}}_1\hat{\vec{S}}_2 - 3(\hat{\vec{S}}_1\vec{r}_{12})(\hat{\vec{S}}_2\vec{r}_{12})}{\vec{r}_{12}^5}\right). \tag{8.65}$$

As one can see this is a dipole-dipole interaction Hamiltonian with the magnetic moments replaced by spin operators multiplied with $g_e\mu_B/\hbar$. It describes the energy and the spacial motion of the spin. As the effect of the spin on the spatial motion is negligible, the wave functions of local motion and spin can be separated. Now it is possible to calculate a spatial quantum-mechanical mean. A quantum-mechanical mean looks as follows:

$$\overline{H^S} = \int {}^3\Phi^*(r_1, r_2)H^S\,{}^3\Phi(r_1, r_2)dV_1dV_2. \tag{8.66}$$

Now the interaction Hamiltonian is inserted. To have a clearer look at it, we separate the integral, as the Hamiltonian consists of a sum inside the brackets. The first addend is:

$$\frac{\mu_0}{4\pi}\frac{g_e^2\mu_B^2}{\hbar^2}\int {}^3\Phi^*(r_1, r_2)\frac{\hat{\vec{S}}_1\hat{\vec{S}}_2}{\vec{r}_{12}^3}\,{}^3\Phi(r_1, r_2)dV_1dV_2. \tag{8.67}$$

As the spin operators are not spacial dependent and the integral is a scalar, they can be moved outside the integral, for a further purpose $\hat{\vec{S}}_1$ to the left and $\hat{\vec{S}}_2$ to the right:

$$\hat{\vec{S}}_1\int ...\ \hat{\vec{S}}_2. \tag{8.68}$$

For the second addend is:

$$-3\frac{\mu_0}{4\pi}\frac{g_e^2\mu_B^2}{\hbar^2}\int {}^3\Phi^*(r_1, r_2)\frac{(\hat{\vec{S}}_1\vec{r}_{12})(\hat{\vec{S}}_2\vec{r}_{12})}{r_{12}^5}{}^3\Phi(r_1, r_2)dV_1dV_2. \tag{8.69}$$

Now we swap the $\hat{\vec{r}}_{12}$ and $\hat{\vec{S}}_2$ to again move the spin operators outside the integral. By doing so $\vec{r}_{12}$ is transposed so the integral now contains a second order tensor:

$$\hat{R} = \vec{r}_{12}\cdot\vec{r}_{12}^T = \begin{pmatrix} x_{12}x_{12} & x_{12}y_{12} & x_{12}z_{12} \\ y_{12}x_{12} & y_{12}y_{12} & y_{12}z_{12} \\ z_{12}x_{12} & z_{12}y_{12} & z_{12}z_{12} \end{pmatrix}. \tag{8.70}$$

Now we insert the matrix abbreviation into the spatial-averaged Hamiltonian:

$$\overline{H^S} = \hat{\vec{S}}_1\left[\frac{\mu_0}{4\pi}\frac{g_e^2\mu_B^2}{\hbar^2}\int {}^3\Phi^*(r_1, r_2)\left(\frac{1}{r_{12}^3} - \frac{3\hat{R}}{r_{12}^5}\right){}^3\Phi(r_1, r_2)dV_1dV_2\right]\hat{\vec{S}}_2. \tag{8.71}$$

The term inside rectangular brackets will now be renamed $2F$. For purposes of analysis, we will switch to index notation. Indices will be $i, j = x, y, z$, so we can rewrite this as

$\hat{R}_{ij} = \vec{r}_{12,i} \cdot \vec{r}^{T}_{12,j}$ and we may use abbreviations such as $\vec{r}_{12,1} = x_{12}, \vec{r}_{12,2} = y_{12}, \vec{r}_{12,3} = z_{12}$. That term, written in index notation, is:

$$F_{ij} = \frac{\mu_0}{4\pi} \frac{g_e^2 \mu_B^2}{2\hbar^2} \int {}^3\Phi^*(r_1, r_2) \left(\frac{\delta_{ij}}{r_{12}^3} - \frac{3\hat{R}_{ij}}{r_{12}^5} \right) {}^3\Phi(r_1, r_2) dV_1 dV_2. \tag{8.72}$$

As all matrices inside are symmetrical; this term remains symmetrical as well. As symmetrical matrices can be diagonalized, all off-diagonal terms disappear, which will be assumed for all further thoughts.

$$F_{i \neq j} = 0 \tag{8.73}$$

$$F_{xx} = \frac{\mu_0}{4\pi} \frac{g_e^2 \mu_B^2}{2\hbar^2} \int {}^3\Phi^*(r_1, r_2) \left(\frac{r_{12}^2 - 3x_{12}^2}{r_{12}^5} \right) {}^3\Phi(r_1, r_2) dV_1 dV_2 \tag{8.74}$$

$$F_{yy} = \frac{\mu_0}{4\pi} \frac{g_e^2 \mu_B^2}{2\hbar^2} \int {}^3\Phi^*(r_1, r_2) \left(\frac{r_{12}^2 - 3y_{12}^2}{r_{12}^5} \right) {}^3\Phi(r_1, r_2) dV_1 dV_2 \tag{8.75}$$

$$F_{zz} = \frac{\mu_0}{4\pi} \frac{g_e^2 \mu_B^2}{2\hbar^2} \int {}^3\Phi^*(r_1, r_2) \left(\frac{r_{12}^2 - 3z_{12}^2}{r_{12}^5} \right) {}^3\Phi(r_1, r_2) dV_1 dV_2 \tag{8.76}$$

It can be easily shown that the trace over F is 0 by summing up the above three expressions. So we have finally rewritten the space-averaged Hamiltonian to be further explicitly expressed as:

$$\overline{H^S} = 2\hat{\vec{S}}_1 F \hat{\vec{S}}_2 = 2F_{xx} \hat{\vec{S}}_{1x} \hat{\vec{S}}_{2x} + 2F_{yy} \hat{\vec{S}}_{1y} \hat{\vec{S}}_{2y} + 2F_{zz} \hat{\vec{S}}_{1z} \hat{\vec{S}}_{2z}. \tag{8.77}$$

Now I would like to show that the above relation can be expressed with the total spin:

$$\hat{\vec{S}} = \hat{\vec{S}}_1 + \hat{\vec{S}}_2. \tag{8.78}$$

$$\overline{H^S} = \hat{\vec{S}} F \hat{\vec{S}} = \hat{\vec{S}}_1 F \hat{\vec{S}}_1 + \hat{\vec{S}}_2 F \hat{\vec{S}}_2 + \hat{\vec{S}}_1 F \hat{\vec{S}}_2 + \hat{\vec{S}}_2 F \hat{\vec{S}}_1 \tag{8.79}$$

Looking at the first addends we see that they become zero (as we see a trace over F here again):

$$\hat{\vec{S}}_1 F \hat{\vec{S}}_1 = F_{xx} \hat{S}_{1x}^2 + F_{yy} \hat{S}_{1y}^2 + F_{zz} \hat{S}_{1z}^2 = F_{xx} \tfrac{\hbar^2}{4} + F_{yy} \tfrac{\hbar^2}{4} + F_{zz} \tfrac{\hbar^2}{4} = 0. \tag{8.80}$$

The latter addends are the same as F is symmetrical. Thus it has been shown that

$$\overline{H^S} = 2\hat{\vec{S}}_1 F \hat{\vec{S}}_2 = \hat{\vec{S}} F \hat{\vec{S}}. \tag{8.81}$$

As we have seen, the trace over F is 0; so we may split it into two constants D and E. These, from now on called fine-structure-constants, may look as if they have been chosen arbitrarily:

$$D = \hbar^2 \left(F_{zz} - \frac{1}{2}(F_{xx} + F_{yy}) \right), \tag{8.82}$$

$$E = \hbar^2 \frac{1}{2}(F_{xx} - F_{yy}). \tag{8.83}$$

Writing these explicitly using the above definition of the diagonal elements of F yields:

$$D = \frac{3}{4}\frac{\mu_0}{4\pi} g_e^2 \mu_B^2 \int {}^3\Phi^*(r_1, r_2) \left(\frac{r_{12}^2 - 3z_{12}^2}{r_{12}^5} \right) {}^3\Phi(r_1, r_2) dV_1 dV_2, \tag{8.84}$$

$$E = \frac{3}{4}\frac{\mu_0}{4\pi} g_e^2 \mu_B^2 \int {}^3\Phi^*(r_1, r_2) \left(\frac{y_{12}^2 - x_{12}^2}{r_{12}^5} \right) {}^3\Phi(r_1, r_2) dV_1 dV_2. \tag{8.85}$$

From the definition of D and E we see that the magnitude of the fine-structure interaction scales with the energy of dipole interaction between the two electrons, or in other words, with the interaction of two Bohr magnetons in a distance specific to the molecule. The D parameter reflects the deviation of the molecule from the spherical geometry along the connecting axis, while the E parameter shows the difference between the off-axial components. D has already me mentioned as zero field splitting and amounts to 2.88 GHz. Two times E is observable as a small energy difference between the $m_s = 1$ and $m_s = -1$ states. It is very small and different for every NV, because the deviation from equal off-axial components is highly dependent on the local crystalline strain.

8.6 Annealing niobium wires

In the process of creating a bond, the wire has to be bent; if the material is too hard, it may eventually break off the bond's first connection spot. Niobium, needed for its super-conductive properties in a cryogenic experiment, is such a hard material, but we expected the drawn wire to become more flexible if it was annealed. In that paper the niobium filament was heated nearly to its melting point by applying current. As such temperatures would cause the wire to burn, this process can only be performed under oxygen-free environment. A suitable option was a small testing vacuum chamber, which could be brought down to 10^{-7} mbar via a membrane- and a turbo-pump within a few hours. A hot-cathode ionization gauge had already been installed for measuring pressures. First a port for electrical connections was fixed at the bottom of the chamber. From there, two teflon covered copper rods were emerging. These were formed to resemble two horns, between which the wire was intended to be mounted. The wire itself was tied [9] to small washers on its ends to ease mounting. One washer was mounted in the middle, so that it would sag instead of tangle. Finally the chamber was sealed with a porthole to observe the filament. To sustain the low pressure needed all parts of the

[9] a tricky task, as one hardly sees the filament, grab it or even make it move trough its own loops, as it is that stiff

vacuum chamber were joined by CF flanges with copper gasket and steel knife edges that cut into the gasket upon tightening the flange to seal the connection properly.

I first measured the current at which the wire would burn through. This was done by manually adjusting the voltage. When rapidly increasing the voltage, current will rise proportionally, with its resistance slowly increasing as the wire gets hotter. The wire is going to burn through at 127 mA. In contrast, when approaching the critical current slowly, one will notice a different behaviour above 120 mA. The current will start dropping even when the voltage is held constant. That increasing electrical resistance originates from plastic deformation, it thins and elongates. This is of course unwanted as a wire thinner than the given 25 µm would rest just loosely in the bonder's needle, and the bonder's ultrasonic vibrations could not be applied properly. After all it proved expedient to stay at 120 mA for 5 minutes and take it immediately from power afterwards to prevent recrystallization by slowly cooling off.

These wires were not used for my NV experiment (I subsequently used aluminium bonds), but dealing with them was a helpful exercise when it came to inserting such a wire into the bonding machine.

Figure 8.1: This image into the vacuum chamber with the almost white glowing niobium wire was taken at about 100mA current.

Bibliography

[Abr61] A. Abragam. *The Principles of Nuclear Magnetism.* Oxford University Press, 1961.

[AJBB11] V. M. Acosta, A. Jarmola, E. Bauch, and D. Budker. Optical properties of the nitrogen-vacancy singlet levels in diamond. http://arxiv.org/pdf/1009.0032v1.pdf, May 2011. Putz: [2].

[AL97] Daniel S. Abrams and Seth Lloyd. Simulation of many-body fermi systems on a universal quantum computer. *arXiv:quant-ph/9703054*, March 1997. Phys.Rev.Lett. 79 (1997) 2586-2589.

[Ame94] Optical Society Of America. *Handbook of Optics, Vol. 2: Devices, Measurements, and Properties, Second Edition.* McGraw-Hill Professional, 2 edition, September 1994.

[AP01] Gennaro Auletta and Giorgio Parisi. *Foundations and Interpretation of Quantum Mechanics: In the Light of a Critical-Historical Analysis of the Problems and of a Synthesis of the Results.* World Scientific, June 2001.

[Ava02] Technologies Avago. AppCAD. http://www.hp.woodshot.com/, 2002.

[azo13] azom. Titanium - corrosion by acids. http://www.azom.com/article.aspx?ArticleID=1240#_Red_Fuming_Nitric, 2013.

[BB84] Charles H. Bennett and Gilles Brassard. Quantum cryptography: public key distribution and coin tossing. *Proceedings of IEEE International Conference on Computers Systems and Signal Processing*, Bangalore India, December 1984:175–179, 1984.

[BBC+95] Adriano Barenco, Charles H. Bennett, Richard Cleve, David P. DiVincenzo, Norman Margolus, Peter Shor, Tycho Sleator, John A. Smolin, and Harald Weinfurter. Elementary gates for quantum computation. *Physical Review A*, 52(5):3457–3467, November 1995.

[BCK+08] Gopalakrishnan Balasubramanian, I. Y. Chan, Roman Kolesov, Mohannad Al-Hmoud, Julia Tisler, Chang Shin, Changdong Kim, Aleksander Wojcik, Philip R. Hemmer, Anke Krueger, Tobias Hanke, Alfred Leitenstorfer, Rudolf Bratschitsch, Fedor Jelezko, and Jörg Wrachtrup. Nanoscale imaging magnetometry with diamond spins under ambient conditions. *Nature*, 455(7213):648–651, October 2008.

[BDCZ98] H.-J. Briegel, W. Dür, J. I. Cirac, and P. Zoller. Quantum repeaters: The role of imperfect local operations in quantum communication. *Physical Review Letters*, 81(26):5932–5935, December 1998.

[Ben80] Paul Benioff. The computer as a physical system: A microscopic quantum mechanical hamiltonian model of computers as represented by turing machines. *Journal of Statistical Physics*, 22(5):563–591, 1980.

[Ben09] O. Benson. Single quantum emitters. HU berlin, lecture: Elements of nanophotonics, 2009. http://www.physik.hu-berlin.de/nano/lehre/Gastvorlesung%20Wien/Single%20Emitters, 2009.

[BKK+09] Volker Buschmann, Benedikt Krämer, Felix Koberling, Rainer Macdonald, and Steffen Rüttinger. Quantitative fcs: Determination of the confocal volume. http://www.picoquant.com/technotes/appnote_quant_fcs.pdf, 2009.

[Car07] Kjell Carlsson. Compendium light microscopy, physics of biomedical microscopy - applied physics department, KTH, stockholm. http://www.biox.kth.se/kjellinternet/Compendium.Light.Microscopy.PDF, 2007.

[CGDT+06] L. Childress, M. V. Gurudev Dutt, J. M. Taylor, A. S. Zibrov, F. Jelezko, J. Wrachtrup, P. R. Hemmer, and M. D. Lukin. Coherent dynamics of coupled electron and nuclear spin qubits in diamond. *Science*, 314(5797):281–285, October 2006.

[CGMB90] W. M. Chen, M. Godlewski, B. Monemar, and J. P. Bergman. Steady-state level-anticrossing spectra for bound-exciton triplets associated with complex defects in semiconductors. *Physical Review B*, 41(9):5746, 1990.

[Chi07] L. Childress. Coherent manipulation of single quantum systems in the solid state, March 2007.

[CN71] C D Clark and C A Norris. Photoluminescence associated with the 1.673, 1.944 and 2.498 eV centres in diamond. *Journal of Physics C: Solid State Physics*, 4(14):2223–2229, October 1971.

[CN98] Warren C. W. Chan and Shuming Nie. Quantum dot bioconjugates for ultrasensitive nonisotopic detection. *Science*, 281(5385):2016–2018, September 1998.

[CTDL92] Claude Cohen-Tannoudji, Bernard Diu, and Frank Laloe. *Quantum Mechanics*. Wiley-Interscience, 2 volume set edition, November 1992.

[CZ95] J. I. Cirac and P. Zoller. Quantum computations with cold trapped ions. *Physical Review Letters*, 74(20):4091–4094, May 1995.

[Dav76] G Davies. The a nitrogen aggregate in diamond-its symmetry and possible structure. *Journal of Physics C: Solid State Physics*, 9(19):L537–L542, October 1976.

[Deg08] C. L. Degen. Scanning magnetic field microscope with a diamond single-spin sensor. *Applied Physics Letters*, 92(24):243111–243111–3, June 2008.

[Dem08] Wolfgang Demtröder. *Experimentalphysik 2: Elektrizität und Optik (Springer-Lehrbuch)*. Springer, 5., überarb. u. erw. aufl. edition, December 2008.

[Deu85] D. Deutsch. Quantum theory, the church-turing principle and the universal quantum computer. *Proceedings of the Royal Society of London. A. Mathematical and Physical Sciences*, 400(1818):97–117, August 1985.

[DFD+11] F. Dolde, H. Fedder, M. W. Doherty, T. Nöbauer, F. Rempp, G. Balasubramanian, T. Wolf, F. Reinhard, L. C. L. Hollenberg, F. Jelezko, and J. Wrachtrup. Electric-field sensing using single diamond spins. *Nature Physics*, 7(6):459–463, April 2011.

[DFT+99] A. Dräbenstedt, L. Fleury, C. Tietz, F. Jelezko, S. Kilin, A. Nizovtzev, and J. Wrachtrup. Low-temperature microscopy and spectroscopy on single defect centers in diamond. *Physical Review B*, 60(16):11503–11508, October 1999.

[DH76] G. Davies and M. F. Hamer. Optical studies of the 1.945 eV vibronic band in diamond. *Proceedings of the Royal Society A: Mathematical, Physical and Engineering Sciences*, 348(1653):285–298, February 1976.

[DJ92] David Deutsch and Richard Jozsa. Rapid solution of problems by quantum computation. *Proceedings of the Royal Society of London. Series A: Mathematical and Physical Sciences*, 439(1907):553–558, August 1992.

[DLC+92] Gordon Davies, Simon C. Lawson, Alan T. Collins, Alison Mainwood, and Sarah J. Sharp. Vacancy-related centers in diamond. *Physical Review B*, 46(20):13157–13170, November 1992.

[DLR+11] A. Dréau, M. Lesik, L. Rondin, P. Spinicelli, O. Arcizet, J.-F. Roch, and V. Jacques. Avoiding power broadening in optically detected magnetic resonance of single NV defects for enhanced dc magnetic field sensitivity. *Physical Review B*, 84(19), November 2011.

[DP65] H. B. Dyer and L. du Preez. Irradiation damage in type i diamond. *The Journal of Chemical Physics*, 42(6):1898–1906, March 1965.

[EFMP11] M. D. Eisaman, J. Fan, A. Migdall, and S. V. Polyakov. Invited review article: Single-photon sources and detectors. *Review of Scientific Instruments*, 82(7):071101–071101–25, July 2011.

[Fey82] Richard Feynman. Simulating physics with computers. *International Journal of Theoretical Physics*, 21(6):467–488, 1982.

[FLC+07] Chi-Cheng Fu, Hsu-Yang Lee, Kowa Chen, Tsong-Shin Lim, Hsiao-Yun Wu, Po-Keng Lin, Pei-Kuen Wei, Pei-Hsi Tsao, Huan-Cheng Chang, and Wunshain Fann. Characterization and application of single fluorescent nanodiamonds as cellular biomarkers. *Proceedings of the National Academy of Sciences*, 104(3):727–732, January 2007.

[Fox06] Mark Fox. *Quantum Optics: An Introduction*. Oxford University Press, USA, June 2006.

[FTGY08] Robert E. Fischer, Biljana Tadic-Galeb, and Paul R. Yoder. *Optical System Design*. SPIE Society of Photo-Optical Instrumentation Engi, 2Rev ed edition, January 2008.

[GDT+97] A. Gruber, A. Dräbenstedt, C. Tietz, L. Fleury, J. Wrachtrup, and C. Borczyskowski. Scanning confocal optical microscopy and magnetic resonance on single defect centers. *Science*, 276(5321):2012–2014, June 1997.

[GHD+12] Bernhard Grotz, Moritz V. Hauf, Markus Dankerl, Boris Naydenov, Sébastien Pezzagna, Jan Meijer, Fedor Jelezko, Jörg Wrachtrup, Martin Stutzmann, Friedemann Reinhard, and Jose A. Garrido. Charge state manipulation of qubits in diamond. *Nature Communications*, 3:729, March 2012.

[Gro97] Lov K. Grover. Quantum mechanics helps in searching for a needle in a haystack. *Physical Review Letters*, 79(2):325–328, July 1997.

[HDF+08] R Hanson, V V Dobrovitski, A E Feiguin, O Gywat, and D D Awschalom. Coherent dynamics of a single spin interacting with an adjustable spin bath. *Science (New York, N.Y.)*, 320(5874):352–355, April 2008. PMID: 18339902.

[HHM84] R T Harley, M J Henderson, and R M Macfarlane. Persistent spectral hole burning of colour centres in diamond. *Journal of Physics C: Solid State Physics*, 17(8):L233–L236, March 1984.

[Hol73] A. S. Holevo. Bounds for the quantity of information transmitted by a quantum communication channel. *Problems of information transmission*, 9(3):177–183, 1973.

[HW02] Hermann Haken and Hans C. Wolf. *Molekülphysik und Quantenchemie: Einführung in die experimentellen und theoretischen Grundlagen (Springer-Lehrbuch)*. Springer, 4., völlig neu bearb. u. erw. aufl. edition, November 2002.

[IBW+00] K. Iakoubovskii, M.V. Baidakova, B.H. Wouters, A. Stesmans, G.J. Adriaenssens, A.Ya. Vul', and P.J. Grobet. Structure and defects of detonation synthesis nanodiamond. *Diamond and Related Materials*, 9(3–6):861–865, April 2000.

[ILTT05] Jan Isberg, Adam Lindblom, Antonella Tajani, and Daniel Twitchen. Temperature dependence of hole drift mobility in high-purity single-crystal CVD diamond. *physica status solidi (a)*, 202(11):2194–2198, 2005.

[Jac98] John David Jackson. *Classical Electrodynamics*. John Wiley & Sons, 3. auflage edition, December 1998.

[JCW+06] Tao Jiang, Xiangrong Cheng, Yining Wang, Hua Tong, and Jiming Hu. [effects of three different etching methods on surface morphology and element of pure titanium]. *Sheng wu yi xue gong cheng xue za zhi = Journal of biomedical engineering = Shengwu yixue gongchengxue zazhi*, 23(4):814–817, August 2006. PMID: 17002114.

[JGP+04a] F. Jelezko, T. Gaebel, I. Popa, M. Domhan, A. Gruber, and J. Wrachtrup. Observation of coherent oscillation of a single nuclear spin and realization of a two-qubit conditional quantum gate. *Physical Review Letters*, 93(13):130501, September 2004.

[JGP+04b] F. Jelezko, T. Gaebel, I. Popa, A. Gruber, and J. Wrachtrup. Observation of coherent oscillations in a single electron spin. *Physical Review Letters*, 92(7):076401, February 2004.

[JM98] J. A. Jones and M. Mosca. Implementation of a quantum algorithm on a nuclear magnetic resonance quantum computer. *The Journal of Chemical Physics*, 109(5):1648–1653, August 1998.

[JPG+02] F. Jelezko, I. Popa, A. Gruber, C. Tietz, J. Wrachtrup, A. Nizovtsev, and S. Kilin. Single spin states in a defect center resolved by optical spectroscopy. *Applied Physics Letters*, 81(12):2160–2162, September 2002.

[JW06] F. Jelezko and J. Wrachtrup. Single defect centres in diamond: A review - jelezko - 2006 - physica status solidi (a) - wiley online library. http://onlinelibrary.wiley.com/doi/10.1002/pssa.200671403/pdf, 2006.

[Kan98] B. E. Kane. A silicon-based nuclear spin quantum computer. *Nature*, 393(6681):133–138, 1998.

[KB59] W. Kaiser and W. L. Bond. Nitrogen, a major impurity in common type i diamond. *Physical Review*, 115(4):857–863, August 1959.

[KLM+01] E. Knill, R. Laflamme, G. J. Milburn, et al. A scheme for efficient quantum computation with linear optics. *Nature*, 409(6816):46–52, 2001.

[KMZW00] C. Kurtsiefer, S. Mayer, P. Zarda, and H. Weinfurter. Stable solid-state source of single photons. *Physical Review Letters*, 85(2):290–293, 2000.

[Lev08] Malcolm H. Levitt. *Spin Dynamics: Basics of Nuclear Magnetic Resonance*. Wiley, 2 edition, April 2008.

[LW78] J. H. N. Loubser and J. A. Wyk. Electron spin resonance in the study of diamond. *Reports on Progress in Physics*, 41:1201, 1978.

[LWR+10] G. de Lange, Z. H. Wang, D. Ristè, V. V. Dobrovitski, and R. Hanson. Universal dynamical decoupling of a single solid-state spin from a spin bath. *Science*, 330(6000):60–63, January 2010.

[Mai94] A. Mainwood. Nitrogen and nitrogen-vacancy complexes and their formation in diamond. *Physical Review B*, 49(12):7934, 1994.

[Mat11] Diamond Materials. Diamond materials CVD diamond booklet. http://www.diamond-materials.com/downloads/cvd_diamond_booklet.pdf, 2011.

[ME10] Peter W. Milonni and Joseph H. Eberly. *Laser Physics*. Wiley, April 2010.

[MHS06] N. Manson, J. Harrison, and M. Sellars. Nitrogen-vacancy center in diamond: Model of the electronic structure and associated dynamics. *Physical Review B*, 74(10), September 2006.

[mi72] Imperial metal industries. SURFACE TREATMENT OF TITANIUM, March 1972.

[Mil62] W. A. Miller. On the photographic transparency of various bodies, and on the photographic effects of metallic and other spectra obtained by means of the electric spark. *Philosophical Transactions of the Royal Society of London*, 152:861–887, 1862.

[MMK+95] C. Monroe, D. M. Meekhof, B. E. King, W. M. Itano, and D. J. Wineland. Demonstration of a fundamental quantum logic gate. *Physical Review Letters*, 75(25):4714–4717, December 1995.

[MSH+08] J. R. Maze, P. L. Stanwix, J. S. Hodges, S. Hong, J. M. Taylor, P. Cappellaro, L. Jiang, M. V. Gurudev Dutt, E. Togan, A. S. Zibrov, A. Yacoby, R. L. Walsworth, and M. D. Lukin. Nanoscale magnetic sensing with an individual electronic spin in diamond. *Nature*, 455(7213):644–647, October 2008.

[MW70] R. P. Messmer and G. D. Watkins. Linear combination of atomic orbital-molecular orbital treatment of the deep defect level in a semiconductor: Nitrogen in diamond. *Physical Review Letters*, 25(10):656–659, 1970.

[NC11] Michael A. Nielsen and Isaac L. Chuang. *Quantum Computation and Quantum Information: 10th Anniversary Edition.* Cambridge University Press, 10 anv edition, January 2011.

[NKJ+03] A. Nizovtsev, S. Kilin, F. Jelezko, I. Popa, A. Gruber, C. Tietz, and J. Wrachtrup. Spin-selective low temperature spectroscopy on single molecules with a triplet-triplet optical transition: Application to the NV defect center in diamond. *Optics and Spectroscopy*, 94(6):848–858, 2003.

[NKJ+09] P. Neumann, R. Kolesov, V. Jacques, J. Beck, J. Tisler, A. Batalov, L. Rogers, N. Manson, G. Balasubramanian, F. Jelezko, et al. ANU-Digital collections: Excited-state spectroscopy of single NV defects in diamond using optically detected magnetic resonance. *Made available in DSpace on 2010-12-20T06: 02: 42Z (GMT). No. of bitstreams: 1 Neumann_Excited2009. pdf: 1060304 bytes, checksum: ebed6110e8d06df6a2d07771a1842c5d (MD5) Previous issue date: 2009-10-26T00: 06: 18Z*, 2009.

[OLS+05] Hooisweng Ow, Daniel R. Larson, Mamta Srivastava, Barbara A. Baird, Watt W. Webb, and Ulrich Wiesner. Bright and stable core-shell fluorescent silica nanoparticles. *Nano Letters*, 5(1):113–117, January 2005.

[Per12] PerkinElmer. SPCM-AQRH-1X. http://www.perkinelmer.com/CMSResources/Images/44-12462DTS_SPCM%20AQRH.pdf, 2012.

[Pie95] Hugh O. Pierson. *Handbook of Carbon, Graphite, Diamonds and Fullerenes: Processing, Properties and Applications.* William Andrew, 1 edition, January 1995.

[PP12] Leiterplatten Piu-Printex. Rogers RO4450B: PIU-PRINTEX leiterplatten. http://support.piu-printex.at/ptx/index.php?id=84, November 2012.

[Put11] Stefan Putz. Coherent manipulation of nitrogen-vacancy center electron spins, March 2011.

[RBM+10] Kelley Rivoire, Sonia Buckley, Arka Majumdar, Hyochul Kim, Pierre Petroff, and Jelena Vuckovic. Fast quantum dot single photon source triggered at telecommunications wavelength. *arXiv:1012.0300*, December 2010.

[RFM34] Robert Robertson, J. J. Fox, and A. E. Martin. Two types of diamond. *Philosophical Transactions of the Royal Society of London. Series A*, 232:463–535, 1934.

[RFR99] Hermann Römpp, Jürgen Falbe, and Manfred Regitz. *Römpp Basislexikon Chemie. Kompaktausgabe: 4 Bände.* Thieme, Stuttgart, November 1999.

[RMK87] N.R.S. Reddy, N.B. Manson, and E.R. Krausz. Two-laser spectral hole burning in a colour centre in diamond. *Journal of Luminescence*, 38(1–6):46–47, December 1987.

[ROT94] J.G. Rarity, P.C.M. Owens, and P.R. Tapster. Quantum random-number generation and key sharing. *Journal of Modern Optics*, 41(12):2435–2444, 1994.

[SB08] Sabine Szunerits and Rabah Boukherroub. Different strategies for functionalization of diamond surfaces. *Journal of Solid State Electrochemistry*, 12(10):1205–1218, 2008.

[SDV+04] Alyona Sukhanova, Jérôme Devy, Lydie Venteo, Hervé Kaplan, Mikhail Artemyev, Vladimir Oleinikov, Dmitry Klinov, Michel Pluot, Jacques H.M Cohen, and Igor Nabiev. Biocompatible fluorescent nanocrystals for immunolabeling of membrane proteins and cells. *Analytical Biochemistry*, 324(1):60–67, January 2004.

[Sho94] P.W. Shor. Algorithms for quantum computation: discrete logarithms and factoring. In *, 35th Annual Symposium on Foundations of Computer Science, 1994 Proceedings*, pages 124 –134, November 1994.

[Sho95] Peter W. Shor. Scheme for reducing decoherence in quantum computer memory. *Physical Review A*, 52(4):R2493–R2496, October 1995.

[Ska99] B. S. Skagerstam. Topics in modern quantum optics. *Arxiv preprint quant-ph/9909086*, 1999.

[Sli90] Charles P. Slichter. *Principles of Magnetic Resonance*. Springer, 1990.

[SNB+10] M. Steiner, P. Neumann, J. Beck, F. Jelezko, and J. Wrachtrup. Universal enhancement of the optical readout fidelity of single electron spins at nitrogen-vacancy centers in diamond. *Physical Review B*, 81(3), January 2010.

[SSGL59] W. V. Smith, P. P. Sorokin, I. L. Gelles, and G. J. Lasher. Electron-spin resonance of nitrogen donors in diamond. *Physical Review*, 115(6):1546–1552, September 1959.

[SWB+12] T. van der Sar, Z. H. Wang, M. S. Blok, H. Bernien, T. H. Taminiau, D. M. Toyli, D. A. Lidar, D. D. Awschalom, R. Hanson, and V. V. Dobrovitski. Decoherence-protected quantum gates for a hybrid solid-state spin register. *Nature*, 484(7392):82–86, April 2012.

[TCC+08] J. M. Taylor, P. Cappellaro, L. Childress, L. Jiang, D. Budker, P. R. Hemmer, A. Yacoby, R. Walsworth, and M. D. Lukin. High-sensitivity diamond magnetometer with nanoscale resolution. *Nature Physics*, 4(10):810–816, 2008.

[Tes09] Gerald Teschl. *Mathematical Methods in Quantum Mechanics: With Applications to Schrödinger Operators*. American Mathematical Soc., May 2009.

[ue11] uni erlangen. Photonenstatistik. http://www.fp.fkp.uni-erlangen.de/praktikumsversuche-master/BSc-Versuchsanleitungen/B45.pdf, September 2011.

[uni12] univie. resolution. http://www.univie.ac.at/mikroskopie/1_grundlagen/optik/opt_instrument 2012.

[var08] various. Etching titanium without hydrofluoric acid. http://www.finishing.com/134/32.shtml, 2008.

[VLK99] Lorenza Viola, Seth Lloyd, and Emanuel Knill. Universal control of decoupled quantum systems. *Physical Review Letters*, 83(23):4888–4891, December 1999.

[Vog05] Thomas Vogel. Dotierung von diamant durch MeV-Ionenimplantation. http://www-brs.ub.ruhr-uni-bochum.de/netahtml/HSS/Diss/VogelThomas/diss.pdf, 2005.

[Web96] R. H. Webb. Confocal optical microscopy. *Reports on Progress in Physics*, 59:427, 1996.

[Wie83] Stephen Wiesner. Conjugate coding. *ACM SIGACT News*, 15(1):78–88, 1983.

[Wie96] Stephen Wiesner. Simulations of many-body quantum systems by a quantum computer. *arXiv:quant-ph/9603028*, March 1996.

[WKN01] J. Wrachtrup, S. Y. Kilin, and A. P. Nizovtsev. Quantum computation using the 13 c nuclear spins near the single NV defect center in diamond. *Optics and Spectroscopy*, 91(3):429–437, 2001.

[Wol09] D. E. Wolf. What is the confocal volume. http://www.fcsxpert.com/classroom/theory/pdfs/fcs_confocal.pdf, 2009.

[YKC+05] Shu-Jung Yu, Ming-Wei Kang, Huan-Cheng Chang, Kuan-Ming Chen, and Yueh-Chung Yu. Bright fluorescent nanodiamonds-no photobleaching and low cytotoxicity. *Journal of the American Chemical Society*, 127(50):17604–17605, December 2005.

[Zai01] A. M. Zaitsev. *Optical Properties of Diamond: A Data Handbook*. Springer, 1 edition, August 2001.

[Zal98] Christof Zalka. Efficient simulation of quantum systems by quantum computers. *Fortschritte der Physik*, 46(6-8):877–879, 1998.

Lebenslauf – Adrian Kowar

2011 – 2013	Technische Universität Wien – Atominstitut, ZMNS Schwerpunkte: Quantenphysik, Mikroelektronik Diplomarbeit: *Microwave microstructures for enhanced coherent control of nitrogen-vacancy center spin qubits in diamond*
2004 – 2010	Universität Wien, Studium der Physik
2000 – 2004	BRG Roseggergasse, 2380 Perchtoldsdorf
1996 – 2000	BRG Bachgasse (Biolog. Zweig), 2340 Mödling